VISUALIZING PLASTICITY OF CIRCUITS:

DEVELOPMENT OF TWO-TIMEFRAME RABIES VIRUS TRACING

Danielle Kathryn Paynter

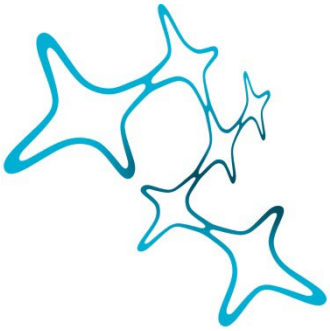

Graduate School of
Systemic Neurosciences

LMU Munich

Dissertation at the
Graduate School of Systemic Neurosciences
Ludwig-Maximilians-Universität München
October, 2024

Supervisor:
Prof. Dr. Mark Hübener
Max Planck Institute for Biological Intelligence

First Reviewer: Prof. Dr. Mark Hübener
Second Reviewer: Prof. Dr. Simon Jacob
External Reviewer: Prof. Dr. Frank Sengpiel

Date of Submission: 25 October 2024
Date of Defense: 13 March 2025

Abstract

An animal's ability to adapt to changing environments is critical to its survival. This ability is, in a large part, enabled by neuroplasticity — the capacity of the brain to store information by changing in response to environmental stimuli. Changes in neuronal connectivity, known as synaptic plasticity, are crucial to the brain's capacity for information storage and retrieval. Synaptic plasticity has two facets: updates in strength of existing synapses, and addition or removal of synapses. Current methods used to study neuroplasticity in the brain generally investigate either anatomical or functional correlates of plasticity. Methods that do so, such as repeated recordings from neurons, and optogenetic activation or inactivation, are powerful and can provide insight into principles of how the brain adapts, but they are limited in scope. For instance, the regions for which function is studied are often already hypothesized to be involved in the plasticity paradigm in question. Alternatively, anatomical tracers allow whole-brain access to circuits, but they do not provide a within-subject comparison of how circuits adapt in response to environmental changes.

Here, I introduce a novel approach that captures circuit changes over time, across the whole mouse brain: two-timeframe monosynaptic rabies virus tracing (TTT). This method allows for the visualization of alterations to a circuit that occur during episodes of learning or plasticity. The foundation of this approach is a modified version of monosynaptic rabies virus tracing performed in transgenic reporter mice. First, as in conventional monosynaptic rabies virus tracing, a group of "starter cells" in a brain region of interest is infected with a helper construct by means of an adeno-associated virus (AAV). Unlike conventional monosynaptic rabies virus tracing, TTT identifies two distinct sets of inputs, based on the "timeframe" in which the neuron becomes infected with rabies virus. The baseline set of "Timeframe 1" neurons projecting to the starter cells is first transsynaptically traced by the rabies virus, which infects presynaptic input neurons throughout the brain. A "snapshot" of this initial connectivity pattern is then made, via conditional expression of the mouse's reporter gene in infected neurons, thereby labeling Timeframe 1 inputs with an additional fluorophore. After taking this "snapshot" of baseline inputs, the mouse undergoes experience-dependent plasticity or training. The rabies virus continuously infects neurons, including putatively novel inputs, as it is still active in the starter cells. These neurons, which become infected during "Timeframe 2", do not express the second fluorophore. Timeframe 2 neurons indicate which parts of the brain contribute to plasticity by strengthening the region's input to the starter cell region.

In order to establish this approach, I first performed a set of *in vitro* experiments in organotypic slice cultures, demonstrating that the helper construct, rabies virus, and conditional gene expression in Timeframe 1 neurons are all functional. I then characterized these three components *in vivo*, showing that: 1) the vast majority of neurons infected with rabies virus during Timeframe 1 is also successfully labeled via conditional expression of the reporter gene, 2) neurons infected with the rabies virus

strain used survive for at least one month after injection in my experimental conditions, and 3) the fraction of Timeframe 2 neurons observed under control conditions is more than twice as high as the "false positive rate," (i.e., the fraction of neurons appearing to have been infected during Timeframe 2, despite being infected during Timeframe 1) showing that rabies virus tracing from starter cells is still occurring during Timeframe 2. From these experiments, I concluded that TTT is functional at a technical level.

Next, I implemented TTT in a standard model for experience-dependent plasticity in the neocortex, monocular deprivation (MD). To assess changes in connectivity associated with the experimental manipulation (MD), I traced inputs to starter cells in mouse binocular visual cortex, such that Timeframe 2 inputs consist of neurons that were newly infected with rabies virus while the visual cortex was undergoing ocular dominance (OD) plasticity, as confirmed by functional imaging. I found that the fraction of Timeframe 2 neurons is significantly higher in mice that underwent MD, in particular in brain regions like the dorsal lateral geniculate nucleus of the thalamus and visual cortical areas. These brain regions provide the strongest input to the starter cell region, and additionally have been implicated in OD plasticity in previous work. As such, this finding suggests that TTT is robust and sensitive enough to identify changes that occur in projections to primary visual cortex during adult OD plasticity in the mouse. Furthermore, taking into consideration the results of the validation experiments, TTT has the potential to provide insight into connectivity changes that underlie other forms of experience-dependent plasticity and learning.

Contents

1. Introduction

1.1. Neuroplasticity

"Memory is the glue that holds our mental life together. Without its unifying power…Our life would be empty and meaningless."

- "The Molecular and Systems Biology of Memory," Kandel et al., 2014

1.1.1. Plasticity enables memory

The formation and storage of memories is enabled by a process called neuroplasticity, which is the brain's ability to selectively update its circuitry and excitability. From recalling warm memories and friends' birthdays, to remembering a stomachache caused by a specific food ingredient, we rely on our memories constantly and in all realms and phases of life. And, as Kandel and colleagues prudently point out, memory gives our lives meaning. What the brain learns and remembers consists not only of these kinds of "declarative" memories of events and facts, but also of "nondeclarative" memories, like learned skills and conditioning or adaptation to our environments. The ways in which plasticity contributes to the formation and storage of memory in the brain is therefore a central topic in neuroscience.

The initial idea that memories are stored at the connections between neurons is attributed to Santiago Ramón y Cajal (Jones, 1994), William James (James, 1890), and Henry Maudsley (Maudsley, 1876). These sites of neuronal connections are called synapses. Donald Hebb was later the first to describe a potential biological mechanism for what was later termed synaptic plasticity. He posited that coincident firing of neurons leads to "some growth process or metabolic change," such that the strength of the connection is altered, thereby storing a memory of the triggering experience (Hebb, 1949).

More than seventy years later, synaptic plasticity's precise roles are still being elucidated. But it is clear that, as Hebb suggested, these growth processes and metabolic changes of neuronal connections enable the formation and storage of memory (Abraham et al., 2019; Poo et al., 2016). Neurons update their connectivity to support learning and memory through alterations in the strength of existing synapses and through formation and loss of synapses (Bailey et al., 2015).

Individual synapses can become stronger or weaker. Experimental evidence for this so-called "Hebbian" synaptic plasticity came in the 1970s, when Bliss and Lømo found that repeated stimulation of presynaptic neurons could induce long-term potentiation (LTP) of the postsynaptic response (Bliss and Lømo, 1973). LTP is a long-lasting strengthening of a synapse, which allows more effective and reliable signal transmission between the pre- and postsynaptic neuron. In short, the connection between two neurons is strengthened by LTP. In contrast, long-term depression (LTD) of a synapse is a lasting weakened connection (Dudek and Bear, 1992). An example where both of these processes have

been shown to have causal links to memory comes from work using cued fear conditioning as an associative memory paradigm (Nabavi et al., 2014; Whitlock et al., 2006). Nabavi and colleagues showed that rats learned to associate a tone with a foot shock, and also learned to associate optogenetic activation of sensory-specific inputs to the amygdala with a foot shock. Furthermore, this artificial stimulation induced optogenetically was shown to induce LTP of these relevant inputs to the amygdala. Finally, they showed that experimentally induced LTD of these inputs caused inactivation of the fear memory. These experiments provide a direct link between behavioral expression of associative memory, and the increase or decrease in efficacy of synaptic transmission (Nabavi et al., 2014).

Synapses are formed and eliminated in the juvenile as well as the adult brain, both under baseline conditions and in response to experience (Attardo et al., 2015; Bhatt et al., 2009; Holtmaat and Svoboda, 2009; Pfeiffer et al., 2018; Trachtenberg et al., 2002; Zhou et al., 2020; Zuo et al., 2005). Synapse loss and formation, collectively called synaptic "turnover," is often studied by using dendritic spines as a proxy for synapses. Spines are small protrusions from dendrites and are the postsynaptic sites of most excitatory synapses. A large body of work demonstrates that formation of new, stable spines is associated with learning and memory (Bailey and Kandel, 1993; Keck et al., 2008; Leuner et al., 2003; Ma and Zuo, 2022; Sengpiel et al., 1999; Xu et al., 2009; Yang et al., 2009). However, these numerous studies of postsynaptic plasticity of spines are often missing the complementary piece of the puzzle: which presynaptic neurons provide input to these novel spines?

While a nascent, immature spine may not be receiving input from a presynaptic neuron, stable spines (those lasting more than 15 to 18h) are reported to always be the site of at least one synapse, as determined by electron microscopy (Knott et al., 2006; Nägerl et al., 2007). This means that lasting spines that form in response to some episode of plasticity are connected to presynaptic neurons. Note that there are two categories of these presynaptic partners: the presynaptic neuron providing input to a new spine may be already connecting to the postsynaptic neuron via other synapses, or, alternatively, it may be providing entirely novel input to the postsynaptic neuron. Increasing the number of synapses by which a pair of neurons is connected likely increases the overall efficacy of signal transmission between them (Fauth et al., 2015; Greenough and Bailey, 1988; Markram et al., 1997). Plasticity also involves the addition and removal of neurons from a network (Albieri et al., 2015; Barnes et al., 2015). This form of rewiring has important implications for the overall storage capacity of the brain and for the organism's ability to learn and adapt (Chklovskii et al., 2004). A network that is not static, but can fully lose connections and form entirely new ones, is more flexible and efficient (Li et al., 2017). It is not in question, whether gain and loss of neurons from a circuit is possible (Falkner et al., 2016; Kaplan and Hinds, 1977; Schwob et al., 1999). What is still uncertain is the degree to which this process contributes to plasticity underlying learning and memory. That is, do most plasticity-related spines receive input from neurons that already connect to the postsynaptic cell? Or does a substantial fraction of new spines receive input from

previously unconnected neurons? This ratio is yet undetermined, but could be investigated experimentally.

1.1.2. Paradigms for studying plasticity in the brain

Synaptic plasticity supports the storage of information in the brain. As implied in the previous section, a diverse set of experimental paradigms has been developed to study the relationship between these alterations in neuronal connectivity, and alterations in an animal's behavior. These paradigms can be broadly categorized into two groups: learning paradigms, and experience-dependent plasticity (EDP) paradigms. The difference is largely in semantics, in that EDP is sometimes considered under the larger umbrella of "learning." For this thesis, I distinguish between learning as a process by which an animal acquires knowledge or a skill through remembering some features of an experience, and EDP as a passive adaptation to a change in sensory input. However, it is important to note that the underlying processes enabling both EDP and more semantic forms of memory likely exist on a spectrum and, in all possibility, involve many of the same cellular mechanisms (Hübener and Bonhoeffer, 2010).

Established learning paradigms include associative learning, such as fear conditioning or conditioned taste aversion, spatial navigation, categorization of stimuli, among many others (Garcia et al., 1955; Kim and Fanselow, 1992; Reinert et al., 2021; Rosenberg et al., 2021). In most cases, experiments that study learning do so in a trial-based structure, where animals are repeatedly trained on a task. This task structure may involve being rewarded for correct performance and/or punished for failure.

EDP encompasses the structural and functional reorganization of the brain in response to altered sensory input and changes in the environment. Several paradigms have been established to experimentally induce EDP in mammals, enabling us to study the relationship between experience, changes in synaptic connectivity, and changes in the function of brain regions and circuits. Examples include enriched environments; temporary or permanent sensory deprivation via amputation of a digit, lesion of part of the retina, or removal of whiskers; and restriction of visual input to a particular orientation (Jung and Herms, 2014; Kaas et al., 1990; Keck et al., 2008; Kreile et al., 2011; Merzenich et al., 1984; Sztainberg and Chen, 2010; Tagawa et al., 2005; Tanaka et al., 2006; Trachtenberg et al., 2002). Unlike learning paradigms, EDP is generally not induced via trial-based tasks, but rather through persistent alteration of sensory input. One of the most widely-implemented EDP paradigms is monocular deprivation (MD), or temporary closure of one eye (Espinosa and Stryker, 2012; Wiesel and Hubel, 1963). As the key experimental manipulation employed in this thesis, MD will be expanded upon in detail in a later section.

1.2. Visual system as a model for studying plasticity

1.2.1. The mouse visual system

1.2.1.1. Circuitry of the mouse visual system

The mouse visual cortex is an excellent system in which to study experience-dependent plasticity, for several reasons. Visual circuitry in the brain is well-organized, and there is detailed understanding in the field of this organization. And sensory input to the visual system is fairly simple to manipulate, which is useful in experimental settings. The statistics of visual stimuli, such as luminance, spatial frequency, and orientations that are represented, can be parameterized with relative ease. This is not the case, for example, in chemoreception. Here, I lay out the main pathway from the eyes to the visual cortex, and then further elaborate on how the mouse visual cortex is organized.

In mice, visual information is conveyed from cones and rods, the light-sensitive cells in the retina at the back of the eye, via retinal ganglion cells (RGCs), whose axons are bundled in the optic nerve. Two major targets of these fibers are the dorsal lateral geniculate nucleus (dLGN) of the thalamus and the superior colliculus (SC), with the majority of RGC fibers terminating in the latter of these two (Ellis et al., 2016). The vast majority of these fibers cross the midline at the optic chiasm and terminate in the opposite hemisphere from where they originated. As the mouse's eyes are located laterally on the head, mice have a relatively small binocular field of view, spanning approximately 40 degrees (Heesy, 2004). A fraction of the RGC fibers responding to the most medial part of the field of view project to ipsilateral regions (Coleman et al., 2009; Dräger and Olsen, 1980; Heesy, 2004).

Unlike primate and cat dLGN, the mouse dLGN does not contain layers, but is rather separated into "core" and "shell" regions. These differ in that ipsilateral RGC input is only present in a subsection of the core, and input from SC is only present in the shell (Bickford et al., 2015; Kerschensteiner and Guido, 2017). Both subregions receive input from contralateral RGCs. RGC input to the dLGN is arranged retinotopically, along a dorsolateral-ventromedial gradient for elevation, and a medial-lateral gradient for azimuth (Piscopo et al., 2013).

The dLGN provides feed-forward input, conveying visual signal to the cortex. Like most cortical areas, mouse visual cortex has six layers, following the canonical circuit that is shared among mammals (Douglas et al., 1989; Douglas and Martin, 1991). The dLGN projects primarily to layer 4 (L4) of the primary visual cortex (V1). L4 projects to L2/3, which sends signals down to L5. L5 projects to L6, as well as to the opposite hemisphere's visual cortex and several subcortical targets, including SC and the dorsomedial striatum (Kasper et al., 1994; Khibnik et al., 2014; Lur et al., 2016). L6 provides feedback projections to dLGN and other subcortical areas (Olsen et al., 2012).

1.2.1.2. Organization of visual cortex and its inputs

Within primary visual cortex, neurons are arranged retinotopically. Neurons located close together in the cortex respond to stimuli in regions of visual space that are also neighboring (Dräger, 1975; Schuett et al., 2002). This organization results in two-thirds of V1 being driven by monocular input from the contralateral eye. The lateral one-third of V1, termed the binocular region or bV1, responds to input from both eyes (Dräger, 1975).

The mouse visual cortex consists not only of V1, but of several higher visual areas (HVAs), as well. Most HVAs share borders with V1 and also display retinotopy (Wang and Burkhalter, 2007). These regions are directly innervated by V1, and also provide feedback projections to V1 (Morimoto et al., 2021; Wang and Burkhalter, 2007).

In addition to the recurrent connectivity between V1 layers, the feedforward projection from dLGN, and feedback projections from HVAs, V1 receives input from a wide range of subcortical and cortical regions. Large portions of these additional inputs to V1 come from the retrosplenial cortex (RSP), auditory cortex (AUD), and the lateral posterior (LP) nucleus of the thalamus (Morimoto et al., 2021; Siegle et al., 2021; Yao et al., 2023). Analyses of origin layers, response latency, and receptive field size of inputs to V1 suggests that HVAs and LP are higher up in the hierarchical processing stream and are therefore providing feedback projections (Morimoto et al., 2021; Siegle et al., 2021).

1.2.1.3. Selectivity of neurons in V1

Neurons in mouse V1 exhibit tuning to several features of visual stimuli. A neuron might respond preferentially to stimuli of a certain orientation, moving in a certain direction, or moving at a certain speed (Dräger, 1975; Métin et al., 1988). Additionally, neurons in bV1 may respond preferentially to input from either the ipsilateral or contralateral eye, a property known as ocular dominance (OD). While mammals such as primates and carnivorans show clustering of neurons with similar response properties (Bonhoeffer et al., 1995; Bonhoeffer and Grinvald, 1991; Hubel and Wiesel, 1968, 1962; LeVay et al., 1975; Ohki et al., 2006, 2005; Payne et al., 1981; Tootell et al., 1981; Weliky et al., 1996; Wiesel et al., 1974) such organization is putatively lacking in mice (Bonin et al., 2011; Mrsic-Flogel et al., 2007; Ohki et al., 2005; but see Goltstein et al., 2023).

These response properties of neurons in V1 are, in all likelihood, shaped by the presynaptic neurons in brain regions described previously that provide feedforward and feedback visual information, along with other contextual information such as physical movement (Keller et al., 2020; Vangeneugden et al., 2019; Wang et al., 2024).

1.2.2. Ocular dominance plasticity in the visual system

To state explicitly what has already been implied: the mouse visual system is plastic, exhibiting changes at multiple scales in response to altered sensory input. Restriction of visual input to just one eye via MD has been used since the 1960s as one such modification to sensory input (Wiesel and Hubel, 1963). Under normal conditions, the binocular region of V1 responds to input from both eyes, albeit to different degrees, with stronger responses for stimuli presented to the contralateral eye. The difference in

response strength is often described by a normalized difference index called the ocular dominance index, or ODI. ODI values fall between -1 and 1, and are usually positive, reflecting stronger responses to the contralateral eye. The ODI in the visual cortex can be measured using several techniques, for example intrinsic optical signal imaging (IOS) while presenting visual stimuli to one eye at a time (Bonhoeffer and Hübener, 2016; Grinvald et al., 1986). During MD, the ratio of responses evoked by stimulation of each eye shifts towards the open, unaffected eye (Wiesel and Hubel, 1963). The ODI therefore decreases. This shift is indicative of ocular dominance plasticity. OD plasticity was first studied in cats, but has also been studied in primates, rats, and mice (Dräger, 1978; Fagiolini et al., 1994; Gordon and Stryker, 1996; LeVay et al., 1975; Wiesel and Hubel, 1963). OD plasticity occurs more readily in juvenile animals, compared to adults; indeed, adult animals in some species do not seem to show OD plasticity at all (Guire et al., 1999; Lickey et al., 2004; Sawtell et al., 2003; for review, see Hübener and Bonhoeffer, 2014). OD plasticity is strongest during "critical periods" in development, in which the brain is especially plastic and susceptible to influence from sensory input. In mice, monocular experience still influences circuits and neuronal response properties after the closure of the critical period, but the effects are more transient and less drastic (Sawtell et al., 2003).

The ODI shift induced by MD has two components: weakening of the response to stimulation of the previously-closed eye, and strengthening of the response to the open, unaffected eye. Critical period plasticity in mice is characterized by an initial drop in cortical responsiveness to the deprived eye, followed by a delayed increase in open-eye responsiveness due to homeostatic plasticity (Frenkel and Bear, 2004). In other words, the ODI shift in juvenile mice is primarily mediated by depression of deprived-eye responses. Deprived-eye depression is dependent on retinal input from the closed eye, as shown by experiments where tetrodotoxin (TTX, a sodium channel blocker) was injected into the vitreous chamber of the eye to silence these inputs (Frenkel and Bear, 2004). During MD but in the absence of TTX, RGCs can still provide some input to the dLGN, because the retina can still respond to gross changes in luminance while the eye is closed. Since the effect does not occur without this uncorrelated input from the retina, it's likely that this deprived-eye depression is mediated by LTD (Heynen et al., 2003; Sawtell et al., 2003).

In contrast to deprived-eye depression seen during the critical period, adult OD plasticity is rather defined by open-eye strengthening of responses as the primary mediator of the ODI shift (Hofer et al., 2006; Sato and Stryker, 2008; Sawtell et al., 2003). At a synaptic level, this means that LTP, rather than LTD, is the likely mechanism of these strengthened responses (Ranson et al., 2012). It is important to note, though, that adult OD plasticity is quite variable, and the pattern of how the responses change depends on external factors such as social hierarchy within the cage, access to voluntary exercise, and other forms of enrichment being available (Balog et al., 2019; Greifzu et al., 2016; Kalogeraki et al., 2014).

What mechanisms lead to these broad effects of MD on cortical responsiveness? Theories about the mechanisms of OD plasticity account for the fact that MD has measurable effects on response properties of individual neurons in the visual system and on connectivity of these neurons. The characteristics of OD plasticity at each of these levels are different in adult mice, as compared to juveniles; these differences are noted in the following sections. Here, OD plasticity at each of these levels is addressed in turn, with a focus on the effects of MD in adult mice.

1.2.2.1. MD alters response properties of single cells

Underlying the shift in ODI measured by population methods like IOS imaging are shifts in the ODIs of individual neurons. After a period of MD, the distribution of ODIs is skewed more towards the open, unaffected eye. During the critical period in mice, a significant change in the distribution of single-unit ODIs is observable after four days of MD (Gordon and Stryker, 1996). In adult mice, however, the effects of MD on the distribution of ODIs are only observable after approximately one week of MD (Hofer et al., 2006; Sato and Stryker, 2008).

In addition to studies that look at the overall distribution of ODIs prior to and following MD, there has also been at least one study that analyzes the shift in ODI for individual neurons, by repeatedly imaging the same cells before and after MD (Rose et al., 2016). The authors found that individual neurons in mouse bV1 become more responsive to the unaffected, ipsilateral eye and less responsive to the previously closed eye. After binocular vision is restored, neurons largely recover their original tuning preference. Additionally, many neurons do not exhibit an ODI shift, suggesting that the effect of OD plasticity observed at the level of the whole cortex is mediated by a subset of the neurons in the region (Rose et al., 2016).

A majority of research on OD plasticity has focused on visual cortex, rather than on subcortical visual structures, possibly because it is more accessible for recording and imaging. As such, the roles of other regions that could be involved in OD plasticity are less established. Work in more recent years has identified effects of OD plasticity in the thalamus, as well. Axonal boutons of neurons in the mouse dLGN that project to binocular V1, despite being primarily (86%) monocular prior to MD, become less responsive to the deprived eye and gain responsiveness to the open eye during MD (Jaepel et al., 2017). Furthermore, the shift observed in dLGN neurons is not dependent on the feedback projections from V1, arguing that the sensory deprivation itself is responsible for dLGN OD plasticity, rather than it being inherited from V1 (Qin et al., 2023).

Neurons in some HVAs also show an effect of MD, in that the distribution of cellular ODIs shifts towards the open eye (Craddock et al., 2023). Interestingly, this study showed that the ODI shift in a particular HVA, the lateromedial area (LM), was stronger than that in bV1. The effects of OD plasticity, then, are not uniform throughout the visual cortex.

Individual cells in the adult mouse bV1 exhibit a shift in their ODI during MD, such that they become relatively more responsive to the open eye (Rose et al., 2016). While it has not yet been shown for neurons followed over time in HVAs and the dLGN, the distribution of unit-wise responses in these regions also respond more strongly to the open eye after MD (Craddock et al., 2023; Jaepel et al., 2017). These findings, taken together, are not entirely surprising, as these regions are strongly connected to each other. The dLGN provides the strongest feed-forward input to bV1, and HVAs are bidirectionally connected to bV1 (Yao et al., 2023).

1.2.2.2. MD alters connectivity between neurons

One goal of this thesis is to understand more about how local and long-range projections to visual cortex contribute to OD plasticity in the adult mouse. The functional shift in responses towards the open, ipsilateral eye during MD is accompanied by synaptic plasticity. In juvenile mice, this includes pruning of spines (and, most likely, their corresponding synapses) on L2/3 and L5 visual cortex neurons (Mataga et al., 2004; Zhou et al., 2017). Additionally, the axons of dLGN neurons in the visual cortex show a reduction in outgrowth during MD (Antonini et al., 1999).

The synaptic plasticity induced by MD is different in adult mice. Instead of spine loss, MD induces significant spine gain on L5 neurons in bV1 (Hofer et al., 2009). Hofer and colleagues also showed that many of these new spines remain stable after re-opening of the temporarily closed eye, despite functional recovery of response strength of each eye. Interestingly, a second eye suture did not induce the same increase in spine turnover and spine density as the first, but rather caused an increase in the size of spines formed following the first MD, likely corresponding to an increase in the strength of these connections (Hofer et al., 2009). However, there is also a significant loss of inhibitory synapses at the initiation of adult MD and, interestingly, during recovery after eye re-opening as well (van Versendaal et al., 2012). That loss of inhibition occurs both with perturbation of visual input, as well as with restoration of normal input, suggests that recovery of previous response properties is not a mere reversion to a previous state of synaptic organization. These findings regarding synapse loss and gain in adult mice are focused on postsynaptic changes, at least for excitatory neurons, but that implies changes in presynaptic structures, as well. For that reason, it is important to consider the main presynaptic inputs to bV1, and how changes in these projections may be contributing to OD plasticity observed in bV1.

One possibility is that the projection from the dLGN to bV1 is undergoing structural plasticity during MD, and thereby providing input to the aforementioned new, stable spines. While direct evidence for plasticity of geniculocortical afferents in monocularly-deprived adult mice is rather lacking, it has been shown by Antonini and colleagues that long MD (20 days) induces growth of these axonal arbors in young adult mice aged P40-P60. This structural plasticity was accompanied by shift in the eye preferences of neurons in visual cortex consistent with weak OD plasticity (Antonini et al., 1999). It is therefore

quite possible that dLGN-bV1 connectivity is altered by MD in a way that contributes to the functional shift in responses in favor of the open eye.

Another possibility is that connectivity with the opposite hemisphere's visual cortex is changing during OD plasticity. Work by Restani and colleagues showed that during the critical period in rats, the shift in ocular dominance is dependent in part on neurons that project via the corpus callosum from the visual cortex ipsilateral to the closed eye. As expected for critical period rats, the ODI distribution shifted strongly towards the open eye during MD. When the callosal projection was pharmacologically silenced after reopening the eye, neurons reverted to responding preferentially to contralateral stimulation (Restani et al., 2009). This suggests that, at least in juvenile rats, the shift in ODI observed in bV1 neurons is partially dependent on input from the opposite visual cortex, which is heavily dominated by the open eye. The role of the callosal projection in OD plasticity has not been specifically investigated in the adult mouse, but based on prior work, this projection is likely involved.

A third way in which connectivity may change during OD plasticity is via local inhibition. As mentioned, adult MD involves the loss of inhibitory synapses. The presynaptic partners of these lost synapses are most likely local inhibitory interneurons (Harauzov et al., 2010).

There are other regions that provide input to bV1 that may also play a role in OD plasticity. For example, projections from motor cortex appear to be important for OD plasticity in adult mice, as a lesion in the secondary motor cortex prevents ODI shifts and improvements in the acuity of the open eye in the same hemisphere during MD (Pielecka-Fortuna et al., 2015). Long-range projections from the medial prefrontal cortex (mPFC) are also hypothesized to influence OD plasticity, as male mice higher up in social hierarchies had both higher prefrontal dopamine concentration and a shift in ODI after only 4 days of MD (Balog et al., 2019). It is clear that connectivity between bV1 and a diverse set of brain regions is implicated in adult OD plasticity. While the roles of the dLGN projection and the callosal V1 projection in OD plasticity have been investigated to some extent, the contribution of synaptic plasticity of inputs from many other regions remains unexplored.

1.3. Rabies virus tracing as a circuit-mapping tool

1.3.1. *Rhabdoviridae* in nature

Rabies virus, the type species of the genus *Lyssavirus*, is a negative strand, bullet-shaped RNA virus. One virion is approximately 180 x 75nm in size. In nature its genome encodes five genes for the following proteins: a nucleoprotein (N), phosphoprotein (P), matrix protein (M), glycoprotein (G), and polymerase (L) (Tordo and Kouknetzoff, 1993). The genetic material is stored in a helical core, surrounded by an envelope protein. Glycoprotein is expressed on the surface of the virion and mediates entry into cells. It is a neurotropic virus that infects neurons and crosses synapses in the retrograde direction, allowing the virus to infect the brain via distal, peripheral motor neurons. Infection leads

to flu-like symptoms, followed by aggression, fear of water and/or fresh air, hallucinations, and cardio-respiratory arrest. Rabies virus is fatal once symptoms have appeared in an infected person or animal ("Rabies," 2024).

Rabies virus infects neurons via chemical synapses, but not electrical gap junctions, and not at cell-cell contacts that are not synapses (Graf et al., 2002; Tang et al., 1999; Ugolini, 1995; for review, see Ugolini, 2010). The mechanism by which rabies virus enters a cell is not entirely understood. Attempts to delineate the mechanism have yielded several candidate receptors for initial attachment of the virion, including the nicotinic acetylcholine receptor (nAChR), the neural cell adhesion molecule (NCAM), the low-affinity nerve growth factor receptor (p75NTR), and the metabotropic glutamate receptor 2 (mGluR2) (Bracci et al., 1988; Cremer et al., 1994; Guo et al., 2019; Lafon, 2005; Tuffereau et al., 2007; Wang et al., 2018). However, neurons expressing none of these target receptors are also susceptible to rabies virus infection, arguing that not all mechanisms of entry have been identified yet (Piccinotti et al., 2013). After attachment, the virion is endocytosed in an actin-dependent manner (Guo et al., 2019; Piccinotti and Whelan, 2016), but precise entry routes seem to vary by rabies virus substrain. For example, work by Gabriella Ugolini, who is responsible for much of what is known about rabies virus as a transneuronal tracer, showed that CVS-11 strain rabies virus injected into the peripheral nervous system infected only motor neurons, and not the sensory or autonomic neurons in the injection region (Ugolini, 1995, further experiments confirming result reviewed in Ugolini, 2011). Rabies virus strains carried by bats, though, are able to infect humans via superficial bites to the skin, indicating that sensory neurons can, in principle, also allow for rabies virus entry (Hemachudha et al., 2005). The details of these findings paint only a partial picture, regarding the neurotropic characteristics of rabies virus.

Following endocytosis, rabies virus transfers to the cell's soma. Here, too, there is uncertainty with regard to how this occurs. It is possible that an intact virion inside of a vesicle is transported via dynein and microtubules through the axon, towards the soma (Klingen et al., 2008). Alternatively, it is possible that uncoating of the virus and translation of its proteins occurs already near the site of entry, and individual proteins are transported to the soma (Bauer et al., 2014).

Despite these gaps in understanding at the molecular level how rabies virus interacts with the mammalian nervous system, we know how the virus acts at a cellular and systemic level: rabies virus is neuron-specific, synapse-specific, and moves retrogradely in the nervous system.

1.3.2 Development of rabies virus tracing as a tool in neuroscience

Viral tracers have been used as tools in neuroscience for several decades. They were adopted because of advantages over conventional tracers that, above all else, were not self-replicating and thereby rendered tracing heavily dependent on the amount of tracer injected. Several neurotropic viruses have been used in tracing connectivity between neurons, including herpes simplex virus type 1, pseudorabies virus, and vesicular

stomatitis virus (Liu et al., 2022). But rabies virus is the most widely-used, possibly for the following reasons: In contrast to herpes viruses, it is exclusively transported retrogradely, has a very low affinity for glial cells, and shows little to no spurious labeling of neurons not connected to an infected cell via a chemical synapse (Liu et al., 2022).

Rabies virus tracing studies were originally performed by injecting the virus to a terminal (usually motor) nucleus of interest and then euthanizing animals after various time intervals. Immunohistochemistry on sliced brains was then used to identify neurons infected with rabies virus. Comparing the extent of tracing across the time course allowed for estimates of when a given nucleus or brain region was infected by the virus and, by extent, an estimate of how many synapses from the origin the region was located (Tang et al., 1999; Ugolini, 1995). This method yielded important findings about connectivity and circuitry, but it was missing precision in that it left uncertainty in whether a rabies virus-infected neuron was a first-order, second-order, or even more distal connection of the injected region. The uncertainty in these studies is compounded by controversy over whether rabies virus tracing is independent of synapse strength and activity. As such, a strong second-order projection to the injection region may be labeled sooner than a weak first-order connection, making it seem as though the weak projection is disynaptically connected to the origin site (Ugolini, 1995). This limitation was addressed by development of monosynaptic rabies virus tracing.

Restriction of rabies virus infection to only the initial set of infected neurons was made possible by deleting the glycoprotein gene from the virus, but growing the virus in cells expressing glycoprotein. The virus incorporated the glycoprotein into its membrane and budded off from the host cells, despite not carrying the gene for glycoprotein (Mebatsion et al., 1996). Rabies virus pseudotyped with glycoprotein, though not expressing glycoprotein, can enter neurons at axon terminals and replicate in the soma, but it cannot transsynaptically infect presynaptic neurons. Wickersham and colleagues made use of this property and, instead of merely deleting the glycoprotein gene, replaced it with the gene for a fluorescent protein (Wickersham et al., 2007a). This virus fluorescently labels neurons throughout the brain that have axon terminals in the injection region. This single-step tracing method is useful for identifying whether neurons project to a given region, but this method cannot identify which neuron(s) in the injection region are synaptically connected to the infected neurons.

Monosynaptic rabies virus tracing, a further development in transneuronal tracing techniques, drastically improved the explanatory power of rabies virus tracing experiments (Wickersham et al., 2007b). This technique differs from the previously-described restricted retrograde tracing technique in that the rabies virus a) can only initially enter an experimentally determined set of neurons, rather than having broad neurotropism, and b) can transsynaptically trace first-order projections to the initially infected cells. Instead of pseudotyping G-deleted rabies virus with glycoprotein, it is pseudotyped with envelope A (EnvA) protein, a ligand for the tumor virus A (TVA) receptor. TVA receptors are expressed naturally in avian species, but not in mammals.

The monosynaptic rabies virus tracing system relies on a so-called “helper” construct, which carries genes for the TVA receptor and glycoprotein. The helper construct can be introduced into neurons in several ways, but the most commonly used are virus injection of an adeno-associated virus (AAV) (see, e.g., Lavin et al., 2020; Watabe-Uchida et al., 2012) and single-cell electroporation of plasmid DNA (see, e.g., Marshel et al., 2010; Wertz et al., 2015). Rabies virus entry is thereby restricted to helper construct-expressing neurons, termed “starter cells”. Once inside a starter cell, rabies virus replicates and expresses the proteins in its genome. Then, via *in trans* complementation with the glycoprotein expressed by the helper construct, rabies virus can cross synapses to neurons with direct input to the initially infected cells. The viral payload is expressed in these first-order input cells, but the virus cannot cross to second-order inputs because of the lack of glycoprotein in these cells (Callaway and Luo, 2015; Wickersham et al., 2007b). Through these modifications, rabies virus tracing was made into a safer and more accessible method that could be applied to more targeted research questions.

1.3.3 Advancements in monosynaptic rabies virus tracing

Since its initial description, rabies virus tracing has been applied to a wide range of circuits and research questions. Advancements in the field have built upon monosynaptic rabies virus tracing, making the technique continually more appealing and powerful. The primary advances have been in further genetic modifications, which have increased the range of possible genes that could be introduced by rabies virus, and in reducing the cytotoxicity of rabies virus.

Rabies viruses that carry genes for optogenetic constructs, calcium indicators, inducible Cre recombinase, and virtually any other protein have been developed (Osakada et al., 2011). These combine the ability to interrogate function and neuronal activity with the benefits of using rabies virus, like the ability to survey the whole brain.

A major disadvantage of first-generation rabies virus tracing is the cytotoxicity of the rabies virus. The rabies virus used in initial monosynaptic tracing studies was of the SAD-B19 strain, which is more cytotoxic and less efficient at labeling input neurons compared to the CVS-N2c strain. Using CVS-N2c strain rabies virus in tracing experiments made it possible for experiments to last for over one month, rather than only one week, without extensive cell death (Reardon et al., 2016).

In addition to introduction of the CVS-N2c strain as a way to reduce cytotoxicity, this challenge was also addressed by so-called “self-inactivating” rabies virus, which relies on a proteasome inhibitor to stop replication after infection (Ciabatti et al., 2017). While initially met with criticism (Jin et al., 2023a), this generation of rabies virus was then shown to be valid (Ciabatti et al., 2023). Two additional advances, introduced as second- and third-generation rabies viruses for monosynaptic tracing, greatly improved the expected survival times of rabies virus-infected neurons, to up to one year (Chatterjee et al., 2018; Jin et al., 2023b; see 4.1.2.2).

There are still several disadvantages of using rabies virus tracing. These include cytotoxicity, incompleteness of labeling of the full set of inputs to a starter cell, and remaining uncertainty about which receptors and features of connectivity influence rabies virus tracing (Svoboda, 2019). Considerable resources have been invested into development and improvement of rabies virus tracing, such that the strengths of the method outweigh its disadvantages by a larger and larger margin.

1.3.4 Toward integrating rabies virus tracing with studies of plasticity

Many monosynaptic rabies virus tracing experiments investigate anatomy and circuits of the brain. While valuable and informative, the advances in rabies virus tracing and in neuroscience have made it possible to move the technique beyond anatomy and connectivity. Introduction of rabies viruses that can express constructs such as genetically encoded calcium indicators (GECIs; e.g., GCaMP) and optogenetic actuators like channelrhodopsins, for example, allow for experiments that investigate neuronal function in addition to connectivity. Rabies virus tracing has also been applied to studies of plasticity, to investigate how experience, learning, and memory influence brain-wide connectivity (Beier et al., 2017; Lavi et al., 2023).

Here, I present a new methodological approach to advance the use of rabies virus tracing in studying plasticity, termed two-timeframe monosynaptic rabies virus tracing (TTT). This approach is designed to identify brain regions that alter their connectivity with the starter cell region during a specific episode of plasticity. The major improvement of the approach presented here is that it incorporates a temporal component to tracing experiments. Through three modifications to classic monosynaptic tracing that will be described in detail in the following section, TTT utilizes the strengths of rabies virus tracing and conditional gene expression to identify a baseline set of inputs to starter cells, and distinguish the baseline inputs from inputs that are infected during a plasticity paradigm. In doing so, TTT has the ability to survey whole-brain inputs to a given brain region, while also going beyond input mapping to be able to gauge not only whether a region projects to a region of interest, but also whether this projection might contribute to functional plasticity.

1.4. Two-timeframe monosynaptic rabies virus tracing

TTT aims to bridge the gap between studies of whole-brain connectivity, and studies of plasticity. To do so, TTT labels two sets of inputs to starter cells: an initial, baseline set of rabies virus-infected neurons, termed “Timeframe 1” inputs, and an additional, plasticity-related set, termed “Timeframe 2” inputs. By doing so, TTT identifies changes in brain regions known to connect to the starter cell region, but may have an unclear role in a given plasticity paradigm. The following is a description of the key principles of TTT, rather than a detailed explanation of specific procedures used in my experiments. The latter will follow in section 2, Materials and Methods.

1.4.1. How does two-timeframe tracing differ from monosynaptic rabies virus tracing?

TTT involves an additional, temporally-controlled labeling, or "snapshot," of rabies virus-infected neurons, which allows us to classify infected neurons as belonging to either Timeframe 1 or Timeframe 2. The value of this approach lies in aligning TTT with a plasticity paradigm of interest, such that Timeframe 1 encompasses a baseline set of inputs, and Timeframe 2 encompasses inputs putatively related to plasticity.

To achieve this differential labeling of Timeframe 1 and Timeframe 2 inputs, we modified the procedure of monosynaptic rabies virus tracing, to include a "snapshot" of the set of neurons infected with rabies virus during the first ten to twelve days following rabies virus injection (Fig. 1.1D). The snapshot uses conditional gene expression of a fluorophore in neurons that have been infected by rabies virus at that time. Neurons that are included in the snapshot express both the rabies virus payload, which usually includes a fluorophore (in the experiments in this thesis, eGFP), *and* a reporter gene of the transgenic reporter mouse line (in the following, tdTomato). Hence, Timeframe 1 neurons are double-labeled with eGFP (carried by the rabies virus), and tdTomato, which is expressed via recombination of the reporter mouse's transgene.

The effect of the snapshot is transient, though. Neurons infected with rabies virus after the effect of the snapshot has worn off will not express the reporter mouse's transgene, but will only express the rabies virus payload (Fig. 1.1E). Having been infected after the snapshot, we consider this set of single-labeled neurons to be part of Timeframe 2. This distinction, between double-labeled Timeframe 1 neurons and single-labeled Timeframe 2 inputs, allows us to visualize relative amounts of rabies virus tracing throughout the brain that may be influenced by an episode of learning or plasticity.

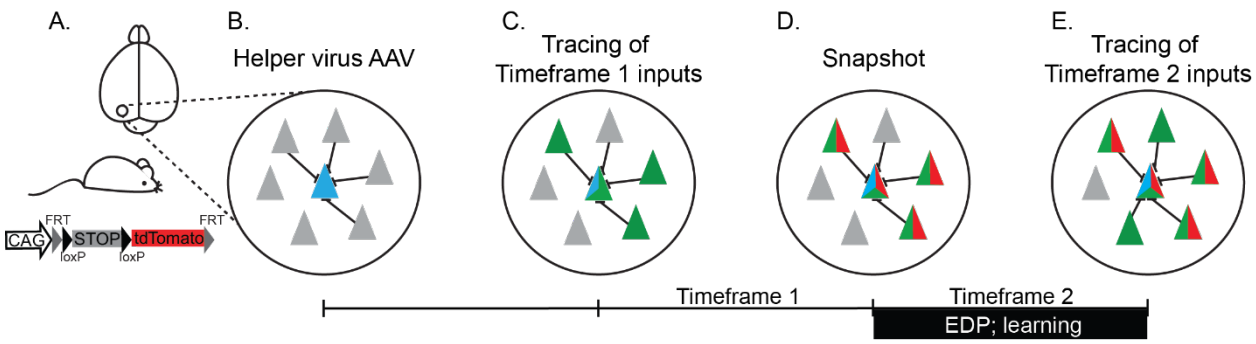

Figure 1.1 | Two-timeframe monosynaptic rabies virus tracing procedure interleaved with an episode of experience-dependent plasticity or learning. A. A reporter mouse line is employed for TTT experiments; here, a tdTomato reporter mouse. **B.** A helper construct, consisting of genes for the TVA receptor, glycoprotein, and a fluorophore (mTurquoise2, in this case) is expressed via injection of an AAV into a brain region of interest. "Starter cells" express mTurquoise2. **C.** Rabies virus, carrying genes for eGFP and inducible Cre recombinase, is injected at the same location. Starter cells and presynaptic inputs to starter cells express eGFP. Note that not all inputs to starter cells are infected. **D.** 4-hydroxy-tamoxifen (4OHT) is injected systemically, inducing expression of tdTomato in rabies virus-traced inputs. Presynaptic neurons labeled during Timeframe 1 express eGFP and tdTomato. **E.** After 4OHT is metabolized, newly-infected Timeframe 2 neurons express only eGFP. Newly-infected neurons are either novel connections, or previously-connected neurons that only become infected during Timeframe 2.

1.4.1. Three modifications to monosynaptic rabies virus tracing

The snapshot that is the defining feature of TTT is made possible by the following modifications to monosynaptic rabies virus tracing: first, TTT experiments are done in transgenic reporter mice. Second, the rabies virus used has a payload that consists not only of a fluorophore, but also of inducible Cre recombinase. Third, Cre recombinase is induced at a strategic time point, enabling recombination and transgene expression in neurons infected with rabies virus at the time of Cre induction.

The first modification made in TTT is the use of transgenic reporter mice. Transgenic reporter mice are, as the name suggests, used to "report" the presence of some other factor, usually Cre recombinase and/or Flp recombinase (see Box 1), in a given cell. Several mouse lines of this sort have been generated by inserting a Cre- or Flp-dependent construct at the *Rosa26* locus (Li et al., 2018; Soriano, 1999). The reporter mouse used in these experiments is the Ai9 "tdTomato" mouse. This line expresses the tdTomato fluorophore in neurons where Cre-mediated recombination has taken place (Madisen et al., 2010). Other transgenic reporter mice could also be used in TTT experiments, though, if a different line were to be more suitable or more easily available. For example, there are Cre reporter mouse lines that were developed alongside the Ai9 line and express EYFP or ZsGreen, instead of tdTomato. These mouse lines could be used in the case that a red fluorophore is used in a different part of the experiment (Madisen et al., 2010).

The second modification is the use of a rabies virus that carries a gene coding for inducible Cre recombinase, in addition to a fluorophore. Inducible Cre allows for temporal control over Cre-mediated recombination, because the protein can only enter the nucleus of a cell after being activated pharmacologically (see Box 1). To maximize the specificity and efficacy of temporal control of the "snapshot" transgene expression, it is important that inducible Cre is highly sensitive to the exogenous estrogen receptor ligand (here, 4OHT), but is also highly resistant to spurious activity of Cre in the absence of treatment with the ligand. To achieve both of these points in TTT experiments, I use a rabies virus that expresses $^{ERT2}Cre^{ERT2}$, a fusion protein with two ER^{T2} sites. This way, spurious Cre activity is reduced to virtually none (Casanova et al., 2002).

Box 1. Development of inducible Cre recombinase.

Cre recombinase is a site-specific recombinase (SSR) protein that has the ability to manipulate the genome at positions where *loxP* sites are located. For example, a gene flanked by loxP sites ("floxed") can be excised from the DNA by Cre recombinase. Inducible Cre recombinase is designed to allow temporal precision in when the genome manipulation (e.g., excision of a STOP codon, or inversion of a gene so that it may be transcribed) takes place. This was accomplished via a fusion protein of Cre recombinase and a modified estrogen receptor binding domain (ER^T site), which we refer to as inducible Cre (Schwenk et al., 1998). The ER^T site was modified to not bind endogenous hormones like β-estradiol, but to only respond to synthetic, exogenous estrogen receptor ligands like 4OHT. When unbound to 4OHT, the ER^T site of the inducible Cre fusion protein represses nuclear translocation of Cre and, by extension, represses Cre-mediated

recombination of DNA in that cell. When 4OHT binds to the ER^T site, Cre recombinase is no longer repressed. ER^{T2}, which is used in TTT experiments, is similar to ER^T, but is approximately ten times more sensitive to exogenous ligands than its predecessor (Indra et al., 1999).

The third modification is the induction of Cre recombinase, which links the previous two modifications together. To do so, 4-hydroxy-tamoxifen (4OHT) is injected systemically. 4OHT binds to the ER^{T2} sites of the inducible Cre protein carried by the rabies virus, allowing Cre to enter the nucleus. Cre induces recombination of the transgene, so that the floxed STOP codon is removed, and tdTomato (or another reporter gene) is expressed in a cell-specific manner. The timing of the 4OHT injection is aligned to occur just prior to the experimental induction of plasticity.

Taken together, these modifications give spatial (rabies virus-infected neurons) and temporal (end of Timeframe 1, when 4OHT is injected) control over expression of a transgene.

1.4.2. General procedure for two-timeframe tracing

To implement two-timeframe tracing with the goal of labeling peri-plasticity inputs to a set of starter cells, the following general steps are followed: 1) a helper construct is expressed in a brain region of interest (Fig. 1.1B); 2) a rabies virus is injected into the starter cell region, to infect starter cells and monosynaptic inputs to starter cells (Fig. 1.1C); 3) 4OHT is injected systemically, to induce the tdTomato snapshot in the set of Timeframe 1 inputs (Fig. 1.1D); and 4) the plasticity paradigm is implemented as Timeframe 2 labeling begins. In principle, these four steps can also be implemented in an *in vitro* system, such as organotypic cultures (see section 3.1). While such a system may not exhibit “experience dependent” plasticity, there are several advantages to using it as a test bed for these procedures.

The helper construct carries genes for the necessary proteins for monosynaptic rabies virus tracing. Incorporating it into an AAV vector which can be injected into the brain is the most straightforward way to express the helper construct, but single-cell electroporation has also been used to initiate rabies virus tracing from single neurons (Marshel et al., 2010; Wertz et al., 2015). There are a few factors to consider, in determining the specifics of helper construct expression, such as the desired location in the brain, which subtypes of neurons (excitatory, neuromodulatory, etc.) one wants to trace from, and approximate number of the starter cells. All of these influence the set of neurons that will be traced by the rabies virus.

Once the helper construct has expressed, the EnvA-pseudotyped rabies virus, which carries genes for a fluorophore and inducible Cre recombinase, is injected into the starter cell region. It infects starter cells and transsynaptically spreads to neurons throughout the brain that provide input to the starter cells. In these neurons, eGFP and inducible Cre are expressed. Importantly, Cre cannot yet enter the nucleus to induce recombination of the tdTomato transgene. At this stage, rabies virus-infected neurons do not express the

tdTomato fluorophore. The initial period of rabies virus tracing, Timeframe 1, lasts seven days in the TTT experiments described here (see timeline below 1.1C-D). This timespan may be modified, for example, with the aim of increasing the proportion of inputs to starter cells that are infected in Timeframe 1. But care must be taken not to extend the timeline of the experiment so far that starter cells begin to die before the end of Timeframe 2.

The third step, application of 4OHT to induce the tdTomato snapshot of Timeframe 1 neurons, is accomplished by systemic (i.p.) injection of 4OHT. As described previously, 4OHT activates the inducible Cre recombinase carried by the rabies virus, which induces recombination and removal of the floxed STOP codon, enabling expression of the tdTomato transgene in neurons that are infected with rabies virus at that time (Fig. 1.1D). I refer to this experimental step as a "snapshot" because it leaves a lasting marker of what the inputs to starter cells consisted of at the time of 4OHT injection.

Only the baseline set of inputs, infected during Timeframe 1, is labeled by the tdTomato snapshot. During Timeframe 2, newly-infected neurons express only eGFP (Fig. 1.1E). These Timeframe 2, eGFP-only inputs correspond to an episode of learning or experience-dependent plasticity that begins at the onset of Timeframe 2. In this way, the readout of TTT contains two sets of brain-wide inputs to starter cells: double-labeled baseline inputs (Fig. 1.1E, green-red triangles), and eGFP-only inputs that were infected while the brain was undergoing some form of plasticity (Fig. 1.1E, green-only triangles). The eGFP-only inputs may have already been connected to starter cells, and simply not infected during Timeframe 1, but they may also be providing novel input to the circuit as a mechanism of plasticity. By comparing the readout in these mice, to a group of control mice who have not experienced the plasticity-inducing paradigm, inferences about which brain regions may be more or less involved in said plasticity paradigm can be drawn.

2. Materials and Methods

2.1. Materials

2.1.1. DNA Constructs

Plasmid Name	Supplier
pAAV.hSyn.TVAmTurquoise2.2A.oG.WPRE	Custom-made
pAAV.hSyn.TVA.T2A.HA.mTurquoise2.F2A.oG.WPRE	Custom-made

2.1.2. Viruses

Virus	Titer	Supplier	Reference
AAV1.CaMKIIa.FLPo.WPRE	16.30 x 10^{11} GC/mL	VectorBuilder (Chicago, Illinois, USA)	Custom-made
AAV1.hSyn.FFLEX.TVAmTurquoise2.2A.oG.WPRE	1.03 x 10^{13} GC/mL	VectorBuilder (Chicago, Illinois, USA)	Custom-made
AAV1.hSyn.HI.eGFP.Cre.WPRE.SV40	1.1 x 10^{13} GC/mL	AddGene (Watertown, MA, USA)	Chan et al., 2017
AAV1.hSyn.TVA.mTurquoise2.F2A.oG.WPRE.SV40	9.028 x 10^{12} GC/mL	University of Pennsylvania Vector Core Services (Philadelphia, Pennsylvania, USA)	Custom-made
AAV2.hSyn.FFLEX.TVA.T2A.HA.mTurquoise2.F2A.oG.WPRE	1.01 x 10^{13} GC/mL	VectorBuilder (Chicago, Illinois, USA)	Custom-made
RABV.N2c.ΔG.eGFP.T2A.^{ERT2}Cre^{ERT2}(EnvA)	6.5 x 10^{8} ffu/mL	Gene Center Munich, LMU (Munich, Germany)	Karl-Klaus Conzelmann
RABV.N2c.ΔG.eGFP.T2A.^{ERT2}Cre^{ERT2} (N2cG)	6.5 x 10^{8} ffu/mL	Gene Center Munich, LMU (Munich, Germany)	Karl-Klaus Conzelmann

2.1.3. Pharmaceuticals

Pharmacological agent	Supplier

APV	Sigma-Aldrich Chemie GmbH (Taufkirchen, Germany)
Atipamezole	Veyx-Pharma GmbH (Schwarzenborn, Germany)
DNQX	Tocris (Bristol, UK)
Fentanyl	HEXAL AG (Holzkirchen, Germany)
Flumazenil	HEXAL AG (Holzkirchen, Germany)
Isopto-Max eye cream	Novartis Pharma GmbH (Melsungen, Germany)
Kolliphor® EL	BASF SE (Ludwigshafen, Germany)
Midazolam	Ratiopharm (Ulm, Germany)
Naloxone	Ratiopharm (Ulm, Germany)
NBQX	Biotrend (Cologne, Germany)
Oculotect® eye drops	Alcon Pharma GmbH (Freiburg, Germany)
Rimadyl® carprofen	Zoetis (Florham Park, New Jersey, USA)
Sedin® Medetomidine	Vetpharma (Barcelona, Spain)
Sterofundin® VG-5 1-1 E, G-5%, Infusionslösung	B. Braun Melsungen AG (Melsungen, Germany)
Tetrodotoxin	Sigma-Aldrich Chemie GmbH (Taufkirchen, Germany)
Xylocain® Pumpspray Lidocaine	AstraZeneca GmbH (Wedel, Germany)
4-Hydroxy-tamoxifen	Sigma-Aldrich Chemie GmbH (Taufkirchen, Germany)

2.1.4. Solutions and media: prepared in-house

Solution	Ingredients	Concentration/amount
Cortex buffer (pH adjusted to 7.4 with 1N NaOH)	NaCl KCl $C_6H_{12}O_6 \cdot H_2O$ $C_8H_{18}N_2O_4S$ $CaCl_2 \cdot 2\ H_2O$ $MgSO_4 \cdot 7\ H_2O$	125mM 5mM 10mM 10mM 2mM 2mM
Grey's balanced salt solution (GBSS)	$CaCl_2 \cdot 2\ H_2O$ KCl KH_2PO_4 $MgSO_4 \cdot 7\ H_2O$ $MgCl_2 \cdot 6\ H_2O$ $NaHCO_3$ NaCl Na_2HPO_4 D-(+) Glucose $\cdot H_2O$	1.5mM 5.0mM 0.2mM 0.3mL 1.0mM 2.7mM 136.9mM 0.9mM 5.6mM

K-Gluconate intracellular solution	K-Gluconate KCl HEPES Na_2-Phosphocreatine NaGTP MgATP	142.5mM 7.5mM 10mM 10mM 0.3mM 4mM
Phosphate buffered saline (PBS)	NaCl KCl Na_2HPO_4 KH_2PO_4	137mM 2.7mM 5.4mM 1.5mM
Slice culture preparation medium (pH adjusted to 7.2 with HCl)	GBSS Kynurenic acid Glucose (50% in H_2O)	98mL 1mL 1mL
Slice culture medium with Penicillin/Streptomycin (pH adjusted to 7.25 with 1N NaOH)	Horse Serum HBSS HEPES (1M) Glucose (50% in H_2O) Penicilin/Streptomycin MEM	50mL 50mL 2.5mL 2mL 1mL 94.5mL

2.1.5. Solutions and media: commercially available

Product	Supplier
X-Clarity™ hydrogel solution	Logos Biosystems (Gyeonggi-do, South Korea)
X-Clarity™ electrophoretic tissue clearing (ETC) solution	Logos Biosystems (Gyeonggi-do, South Korea)
X-Clarity™ mounting solution	Logos Biosystems (Gyeonggi-do, South Korea)
FluorSave™ mounting medium	Merck Chemicals GmbH/Merck Millipore (Darmstadt, Germany)

2.1.6. Glues, gels, and cements

Product	Supplier
Histoacryl®	B. Braun Surgical, S.A. (Rubí, Spain)
Paladur® dental cement	Heraeus Kulzer GmbH (Hanau, Germany)
Pattex® Power Easy Gel	Henkel AG & Co. KGaA (Düsseldorf, Germany)
Pattex® Ultra Gel	Henkel AG & Co. KGaA (Düsseldorf, Germany)

2.1.7. Materials and instruments

Product	Supplier
In vitro experiments	
Axoporator 800A	Molecular Devices, Inc. (San Jose, CA, USA)
Borosilicate glass capillaries 0 (1.5 mm O.D. x 0.86 mm I.D.)	Harvard Instruments (Holliston, MA, USA)
CCD Camera, KP-M2RP	Hitachi Kokusai Electric Inc. (Tokyo, Japan)
Heracell™ 150 CO2 Incubator	Thermo Fischer Scientific (Waltham, MA, USA)
LN SM1 micromanipulator	Luigs & Neumann (Ratingen, Germany)
McIlwain tissue chopper	Mickle Lab Engineering Co. Ltd./Cavey Laboratory Engineering Co. Ltd. (Surrey, UK)
Millicell® Cell Culture Inserts, 0.4 µm, 30 mm diameter	Merck Chemicals GmbH/Merck Millipore (Darmstadt, Germany)
P-97 Flaming/Brown Micropipette Puller	Sutter Instrument Co. (Novato, CA, USA)
Pneumatic PicoPump PV 820	World Precision Instruments (Sarasota, FL, USA)
Thermomixer compact	Eppendorf (Hamburg, Germany)
Vertical puller Model PC-10	Narishige Group (Tokyo, Japan)
In vivo experiments	
Bone wax	Ethicon Inc. (Rariton, NJ, USA)
Borosilicate glass capillaries (OD: 0.8 mm, wall thickness: 0.28 mm)	Hilgenberg GmbH (Malsfeld, Germany)
Cover glasses, round, 4 mm diameter	Glaswarenfabrik Karl Hecht GmbH & Co. KG (Sondheim, Germany)
DC temperature controller and heat pad	FHC (Bowdoin, ME, USA)
Dental drill MF-Perfecta 9975E	W&H (Bürmoos, Austria)
Drill bits HM 1-005	Hager & Meisinger GmbH (Neuss, Germany)
K802H PERMA-HAND Suture 6-0, 7-0	Ethicon Inc. (Rariton, NJ, USA)
MO-10 One-axis oil hydraulic micromanipulator	Narishige Group (Tokyo, Japan)
MP-285 micromanipulator	Sutter Instrument Co. (Novato, CA, USA)
Peristaltic pump Minipuls 3	Gilson Inc. (Middleton, WI, USA)
Stereotax and ear bars	Stoelting (Wood Dale, IL, USA)
Sugi® absorbent sponge points	Kettenbach Medical (Eschenburg, Germany)
Toohey Spritzer Pressure System	Toohey Company (Fairfield, NJ, USA)
Vibratome, 5100mz	Campden Instruments (Leics., UK)

X-Clarity™ polymerization system	Logos Biosystems (Gyeonggi-do, South Korea)
X-Clarity™ tissue clearing system	Logos Biosystems (Gyeonggi-do, South Korea)
Microscopes & related components	
BScope: rotating, translating multiphoton imaging microscope	Thorlabs (Dachau, Germany)
CFI75 LWD 16x, 0.8 NA, water-immersion objective	Nikon Corporation (Tokyo, Japan)
Fiber coupled LED, 530 nm	Thorlabs (Dachau, Germany)
Fiber coupled LED, 735 nm	Thorlabs (Dachau, Germany)
GaAsP photon multiplier tubes	Hamamatsu (Toyooka, Japan)
Leica SP8	Leica Microsystems (Wetzlar, Germany)
Leica Stellaris	Leica Microsystems (Wetzlar, Germany)
MaiTai® HP DeepSee™ Laser	Spectra Physics/Newport (Santa Clara, CA, USA)
Olympus BX51WI	Olympus (Shinjuku, Japan)
Olympus XLFluor 4x/340, 0.28 NA	Olympus (Shinjuku, Japan)
Pockels cell 350-80LA-BK Electro-Optic Modulator	Conoptics (Danbury, CT, USA)
Pockels cell controller 302RM	Conoptics (Danbury, CT, USA)
SteREO Lumar.V12	Carl Zeiss AG (Oberkochen, Germany)
X-Cite® Series 120	Olympus (Shinjuku, Japan)

2.1.8. Software

Software	Company/Source	Version
Arivis Cloud	Carl Zeiss AG (Oberkochen, Germany)	arivis Cloud 2023
ImageJ	Wayne Rasband, National Institutes of Health (Bethesda, MD, USA)	1.52p - 1.54j
LAS-X	Leica Microsystems (Wetzlar, Germany)	1.4.6
MATLAB	The MathWorks (Natick, MA, USA)	R2012b
NUTIL	EBRAINS (Brussels, Belgium)	0.8.0
Python	Python software foundation (Wilmington, DE, USA)	3.7 - 3.9
QuickNII	EBRAINS (Brussels, Belgium)	2.2
ScanImage	Vidrio Technologies, LLC (Janelia Farm, VA, USA)	4.2
VisuAlign	EBRAINS (Brussels, Belgium)	0.9

2.2. *In vitro* Methods

2.2.1. Organotypic slice culture preparation

Organotypic cultures were prepared from the hippocampus of tdTomato reporter mice (B6.Cg-Gt(ROSA)26Sor$^{tm9(cAG-tdTomato)Hze}$/J; Ai9; The Jackson Laboratory), aged P6-P9, according to the protocol by Stoppini et al. (1991). All procedures took place within a laminar flow hood sterilized with UV light. Tools were disinfected with 80% ethanol and a Bunsen burner. Mice were decapitated with scissors and the whole brain was dissected out into freshly-prepared, ice cold slice culture preparation medium, with pH adjusted to 7.2 using HCl. Hippocampi were dissected under a dissection microscope and removed from the rest of the brain. The hippocampi were arranged on a Teflon disk, and a McIllwain tissue chopper fitted with a razor blade cleaned with ether and ethanol was used to slice the hippocampus into 400µm transverse sections. Slices were immediately rinsed into ice cold slice culture preparation medium and stored at 4°C for 30 to 45 minutes. Slices were then plated on small membrane patches on Millipore inserts in 6-well plates. Each well contained 1mL of pre-warmed slice culture medium containing penicillin and streptomycin ("pen/strep"). For single-culture experiments, four cultures were plated in each well. For co-cultures of two hippocampus slices, two co-cultures on larger membrane patches were placed in each well. Cultures were kept at 35°C and 5% CO_2. Twice each week, 0.5mL of the medium was replaced with fresh, warmed pen/strep slice culture medium. Cultures generally survived for at least four weeks.

2.2.2. Virus injections in slice cultures

Virus solutions were injected, undiluted, into CA1 of organotypic hippocampal cultures (aged at least three days *in vitro*) to perform *in vitro* monosynaptic rabies virus tracing experiments. Glass capillaries (borosilicate, 1.5mmOD, 0.86mmID) were pulled into pipettes for microinjection using a horizontal puller (Sutter Instrument Co.; settings: heat: ramp + 20, pull: 30, velocity: 50, time: 250) and then clipping the tip until the diameter was approximately 12µm (for AAVs) or 16µm (for rabies virus). Injection pipettes were back filled with 1 to 2µL of virus solution, inserted into the pipette holder of a Pneumatic PicoPump PV 820, and visually inspected to ensure there were no air bubbles or debris. Warmed slice culture medium (800µL) was pipetted into a disinfected slice chamber at an Olympus BX51WI microscope fitted with a 4x objective. Millipore inserts holding cultures were brought from the incubator using a small petri dish (35mm) with 1mL of warmed slice culture medium, and transferred to the slice chamber with sterile forceps. An LN SM1 micromanipulator was used to position the pipette over CA1 of the culture to be injected. The pipette was inserted into CA1, and then withdrawn slightly along the axis of the pipette, to create an indentation that virus could flow into. One timed pulse was applied (settings: pressure: 20 psi, pulse duration: 250ms). The pipette was then retracted and cultures were returned to the incubator. Pipettes were reused for all injections of a given virus on a given day.

2.2.3. Single cell electroporation

Sparse expression of constructs in organotypic cultures was achieved using single-cell electroporation. Glass capillaries (borosilicate, 1.5mmOD, 0.86mmID) were pulled on a vertical puller (for which the heating values were measured in arbitrary units) into pipettes with a resistance of 10-15MΩ. Pipettes were backfilled with sterile-filtered K-gluconate intracellular solution containing plasmid DNA at concentrations ranging from 50nM to 250nM. Cultures were brought from the incubator to the setup in warmed, sterilized cortex buffer, and moved to the slice chamber containing cortex buffer. Neurons in CA1 were targeted with a 40x immersion objective, bright field illumination, an infrared filter, and a CCD camera. The pipette, under positive pressure, was brought into contact with a neuron until a dimple in the cell body was observed. Positive pressure was released and, if the acoustically monitored resistance increased above 20MΩ, a 1s pulse train was triggered (-12V, 0.5ms pulse duration, 50Hz) using an Axoporator 800. The process was repeated for three cells per culture. A pipette was reused for subsequent cultures only if the resistance measured in cortex buffer was still within 10-15MΩ, indicating it was not clogged with debris.

Single cell electroporation was particularly advantageous for *in vitro* experiments, where I needed only one to three cells to express the constructs. Single cell electroporation does not have a high throughput, and therefore was not well-suited to the *in vivo* experiments described in this work.

2.2.4. Epifluorescence imaging

Expression of fluorescent constructs in live cultures was assessed using an X-Cite Series 120 mercury lamp and a ZEISS SteREO Lumar.V12 microscope fitted with filters for cyan (excitation filter: 470/40nm, emission filter: 525/50nm), green (excitation: 470/40nm, emission: 525/50nm), and red (excitation: 560/40nm, emission: 630/75nm) fluorophores. Cultures were imaged within the 6-well plate, brought directly from the incubator. Exposure time was adjusted automatically for each culture to account for differences in expression strength, as quantitative fluorescence measurements were not necessary for these qualitative checks for expression.

2.2.5. Drug Application

The drug 4-hydroxy-tamoxifen (4OHT) was used to induce “snapshot” labeling of Timeframe 1 inputs to starter cells in rabies virus tracing experiments. For *in vitro* application of 1µM 4OHT, a stock solution was first prepared with a concentration of 3.3mM, or 1.29mg per mL of 100% EtOH, using a heated mixer set to 35°C and a 2mL Eppendorf tube. 3µL of the stock solution was then added to 10mL of pen/strep slice culture medium in a Falcon tube. Culture medium was vortexed immediately before use.

To apply 4OHT to cultures, 1mL of pen/strep + 4OHT slice culture medium was pipetted into each well of a 6 well plate. Inserts containing cultures were moved with sterile forceps from the wells containing normal pen/strep slice culture medium to the 4OHT-containing plate, and returned to the incubator for 24 hours. To end 4OHT treatment

after 24 hours, cultures were moved to fresh Millipore inserts on pen/strep slice culture medium using sterile forceps to lift the membrane patch of each culture.

In a subset of experiments, various pharmacological agents were used to influence neuronal activity of the cultures, by blocking a given receptor or combination of receptors. Each given drug was mixed into pen/strep slice culture medium at the desired concentration and applied to slice cultures in a 6-well plate as described above. During drug treatment periods, 0.5mL medium was exchanged in each well every two days. Rinsing from drug-containing medium was performed as described above.

2.2.6. Fixing and imaging slice cultures

Cultures attached to membrane patches were moved to wells of a 24-well plate containing room temperature 4% paraformaldehyde (PFA) for 20 minutes for fixation. Cultures were then rinsed 2x 10 minutes in PBS. Nuclei were stained with a 1:1000 dilution of DAPI in PBS for 15 minutes, and rinsed once more in PBS for 10 minutes. Cultures on membrane patches were mounted on slides with 200µm spacers and FluorSave mounting medium. Cultures were imaged with a Leica TCS SP8 confocal microscope and a 20x immersion objective, using glycerol as immersion medium. Samples were imaged sequentially with laser stimulation at 405nm (DAPI), 488nm (eGFP), and 561nm (tdTomato). Pixel size ranged from 0.7µm x 0.7µm to 1µm x 1µm. The z step between planes was set to three to seven micrometers, depending on the density of labeling in the culture.

2.3. *In vivo* methods

2.3.1. Animal experiments

All experiments were performed with approval from the Regierung von Oberbayern, under animal license ROB-55.2-2532.Vet_02-20-92, and in accordance with the Max Planck Society's institutional guidelines.

2.3.2. Animals

In all *in vivo* experiments, adult male and/or female tdTomato reporter mice (B6.Cg-Gt(ROSA)26Sor$^{tm9(cAG-tdTomato)Hze}$/J; Ai9; The Jackson Laboratory) from an in-house breeding colony were used. Mice were housed in a reverse 12 hour light-dark cycle, with *ad libitum* access to food and water. Mice were cohoused whenever possible, in large, plastic, individually ventilated cages (IVC, Tecniplast GR900; 1500cm^2) containing bedding material and enrichment including a running wheel.

2.3.3. Surgical interventions

In all surgical interventions, mice were anesthetized with an intraperitoneal (i.p.) injection of FMM (Fentanyl (0.05µg/g), Medetomidine (0.5µg/g), Midazolam (5.0µg/g), in saline) and treated prophylactically with a subcutaneous (s.c.) injection of carprofen (5µg/g in saline) for analgesia. The mouse's eyes were protected with a layer of Isopto-Max eye cream. Body temperature was maintained at 37°C with a DC temperature controller and heat pad, and anesthesia was maintained by regularly checking the response to a toe

pinch and injecting additional FMM when needed. After surgery, anesthesia was counteracted by s.c. injection of a mixture of Atipamezole (2.5 µg/g), Flumazenil (0.5 µg/g), and Naloxone (1.2 µg/g), in saline. Carprofen was administered via s.c. injection on each of the two days following a surgical intervention.

2.3.3.1. Cranial window and headbar implantation

Mice aged P48 and older were anesthetized as described, and fixed stereotactically via ear bars. The skin on top of the skull was cleaned first with iodine, and then with 80% ethanol. Lidocaine was applied to the area for local analgesia. A rounded patch of skin was removed from the top of the skull using scissors. The exposed skull was treated with lidocaine and cleaned of hairs and tissue with forceps and a scalpel. The surface of the skull was scratched with the scalpel in order to improve adhesion of the cement. Edges of the skin were, when necessary, fixed to the skull with Histoacryl. The mouse was then removed from the stereotax. A rectangular metal headbar with a hole in the center (weighing 1 gram, produced in-house) was loosely attached with a small amount of glue to the left posterior part of the skull. Dental cement was applied using a syringe to fix the headbar in place. Cement was left to set for at least 20 minutes before proceeding.

A round craniotomy, 4mm in diameter, was made using a dental drill. Depending on the experiment, virus was injected as described below, immediately after the craniotomy. The dura was kept moist using cortex buffer. The craniotomy was covered with a 4mm diameter cover glass, secured with glue.

2.3.3.2. Helper virus injection

If performed in a separate surgery from cranial window implantation, the cover glass above the craniotomy was removed using a dental drill and any tissue, which occasionally grows over the cortex after a craniotomy, was removed. Pipettes for virus injection were pulled on a horizontal puller (settings: heat: ramp + 20, pull: 150, velocity: 120, time: 100) from glass capillaries (length: 100 mm, OD: 0.8 mm, wall thickness: 0.28 mm), trimmed with microscissors, and beveled at a 45 degree angle, to a final outer diameter between 20 and 24 µm. Pipettes were front loaded with virus mixture using negative pressure. The pipette was positioned over the exposed visual cortex using a micromanipulator, lowered onto the surface of the brain, and inserted into the cortex using a one-axis oil hydraulic micromanipulator. Virus was ejected using a Toohey Spritzer and N_2 gas (approximately 50nL, measured by previous calibration of the volume per unit length of the pipette; 300µm depth; one injection site).

For pilot experiments investigating the long-term survival and ramp-up of rabies virus-traced neurons, a mixture of two viruses was used, in order to achieve sparsened expression. A FlpO-dependent “helper virus” expressing a TVA receptor fused to an mTurquoise2 fluorophore and optimized rabies virus glycoprotein under the synapsin promoter (AAV1.hSyn.FFLEX.TVAmTurquoise2.2A.oG.WPRE) and a virus expressing FlpO under the CaMKIIa promoter, to target excitatory neurons (AAV1.CaMKIIa.FLPo.WPRE), were diluted with sterile cortex buffer. 1µL of CaMKIIa:FlpO virus was diluted in 99µL of cortex buffer and vortexed. 1µL of this mixture was added to a 3µL aliquot of helper virus,

for a final FlpO virus dilution of 1:400 (final titer FlpO virus: 4.1 x 10^6 GC/mL; final titer helper virus: 7.5 x 10^{12} GC/mL).

For two-timeframe tracing experiments, the same dilution procedure was used, but changes were made to the design of helper virus. Here, a tricistronic virus (AAV2.hSyn.FFLEX.TVA.T2A.HA.mTurquoise2.F2A.oG.WPRE) was used. By expressing the fluorophore as a protein separate from the membrane-bound TVA receptor, I improved the ability to image neurons expressing the helper virus. In these experiments, the virus injection site was determined by intrinsic optical signal (IOS) imaging of retinotopy to locate the binocular region of the primary visual cortex (see below for details).

2.3.3.3. Transsynaptic rabies virus injection

Two weeks after helper virus injection, mice were again anesthetized and the cover glass was removed. Pipettes for virus injection were prepared as described above, to a final diameter of 24 to 32µm, to account for the higher viscosity of the rabies virus solution. Epifluorescence imaging of mTurquoise2 was used to target the rabies virus injection to the site of helper virus expression. Less than 50nL of undiluted virus was injected.

The rabies virus used expresses an eGFP fluorophore and an inducible Cre protein, and is pseudotyped with envelope A (EnvA) protein, which restricts the virus's entry to cells expressing the TVA receptor (RABV.N2c$^{\Delta G}$.eGFP.T2A.^{ERT2}Cre^{ERT2}(EnvA), "EnvA-pseudotyped rabies virus").

2.3.3.4. Non-transsynaptic rabies virus injection

In a pilot experiment to investigate the efficacy of the 4OHT snapshot, a single surgical intervention was used to inject a non-transsynaptic rabies virus without implanting a headbar or cranial window. Mice were fixed in a stereotax with ear bars. Skin on the top of the skull was prepared as described above, and then a single diagonal incision was made over the left posterior part of the skull using a scalpel. Skin was spread slightly to expose a small region of the skull. A dental drill was used to make a small craniotomy (1-2mm). In this site, 50nL of a rabies virus that does not rely on helper virus to enter cells, but is rather taken up by axon terminals, was injected at each of three depths below the surface of the brain: 600µm, 450µm, and 300µm, for a total of 150nL of virus (RABV.N2c.ΔG.eGFP.T2A.^{ERT2}Cre^{ERT2} (N2cG), "non-transsynaptic rabies virus"). The craniotomy was sealed with bone wax and the incision closed with two to three mattress sutures.

2.3.3.5. Monocular deprivation

Monocular deprivation (MD) was induced under the surgical conditions described in section 2.3.3.; i.e., under anesthesia and after treatment with carprofen analgesia. The right eyelid edges were trimmed using microscissors in order to create a wound that would heal shut after suturing, to ensure the MD would last for the eight day duration. Size 6-0 or 7-0 sutures were used. A mattress suture was used to close the eye in the center. Two additional mattress sutures were then added, one on either side of the center suture, with all three knots over the top lid.

Sutures were checked at least once daily. In the case of eye opening before day 5 of MD, the mouse was anesthetized again and the eye was resutured. If an eye opened after day 5, the mouse was anesthetized and imaged to measure the ocular dominance index, and the experiment was then terminated. The cutoff at day five was selected based on previous work showing that spine gain induced by MD peaked after four days of MD (Hofer et al., 2009).

At the end of the deprivation period, mice were anesthetized and the eye was opened with microscissors. Swelling was reduced with Oculotect® eye drops. IOS imaging (see below) took place immediately after the opened eye was cleared to measure effect of MD on ocular dominance.

2.3.4. 4-hydroxy-tamoxifen injection

To prepare 4OHT for *in vivo* application, the drug in powdered form was dissolved in 100% ethanol at a dilution of either 10mg/mL, or 20mg/mL, depending on the desired dose, in an Eppendorf tube. Dissolution was aided by a heated shaker set to 39°C. A volume of Kolliphor® EL equal to the volume of EtOH used was then added to the Eppendorf tube. The tube was returned to the heated shaker with the lid open. The shaker was loosely covered with aluminum foil for light shielding. The tube was heated and vortexed for up to three hours, until all ethanol evaporated, and the 4OHT remained suspended in Kolliphor. This solution was diluted four times by volume with PBS. 4OHT was freshly prepared no more than 48 hours in advance of treatment. Mice were given an i.p. injection of 0.01mL per gram body weight of warmed 4OHT-Kolliphor-PBS solution. The dose was therefore either 100mg/kg, or 50mg/kg, depending on the initial concentration of 4OHT in ethanol. In a pilot experiment, various doses and treatment protocols were tested: a total dose of either 100mg/kg, or 200mg/kg, and treatment on either one day, or split over two subsequent days. For two-timeframe tracing experiments, 100mg/kg was injected on each of two subsequent days.

2.3.5. Intrinsic optical signal imaging

Intrinsic optical signal (IOS) imaging was performed through cranial windows on anesthetized mice placed on a heat pad and fixed in a headbar holder. Data were acquired using a sCMOS camera (Andor Zyla 4; 12-bit depth) and a 4x Olympus air objective (NA 0.28). A green (530 nm) LED was used to image the blood vessel pattern and find the focal plane (approximately 400µm below the surface of the brain). A red (735 nm) LED and a red filter in front of the camera were used for functional imaging. Frames were acquired at 10Hz during functional imaging, and then downsampled by a factor of 5. Images were acquired at 2048 x 2048 pixels (4.4 x 4.4 µm pixel size) and downsampled to 512 x 512 pixels (17.6 x 17.6 µm pixel size).

Visual stimuli were presented using custom MATLAB scripts and the Psychophysics Toolbox on a monitor controlled by a Tenma power supply. IOS imaging to retinotopically map the visual cortex was performed with the monitor placed primarily in the mouse's right field of view, as cranial windows were placed over left visual cortex. Visual stimuli consisted of drifting gratings of eight orientation and motion direction combinations,

shown in one of 12 positions in a 4 x 3 grid on the monitor. Each stimulus spanned 34 x 32 degrees of visual angle, and presentation was corrected for screen curvature and eccentricity. For each stimulus presentation, imaging took place for 9.5s: a 2s baseline period with no stimulus on the monitor, a 6s period of stimulus presentation, and a 1.5s period after stimulus offset. There was a 0.5s intertrial interval. Four blocks of stimulus presentations were recorded in one retinotopy imaging session.

To measure ocular dominance in binocular visual cortex, the monitor was placed directly in front of the mouse, 13cm away from the nose. Motorized eye shutters (custom 3D printed) controlled by custom MATLAB script were used to block visual input to one eye at a time, thus allowing measurement of response strength for each eye individually. Again, eight orientations and directions of drifting gratings were used, but stimuli were always shown in the center of the monitor, spanning 50 x 70 degrees of visual angle in the center of the visual field so as to primarily activate the binocular region of visual cortex. For each stimulus presentation, imaging took place for 15s: a 5s baseline period with no stimulus on the monitor, a 5s period of stimulus presentation, and a 5s period after stimulus offset. There was a 5s intertrial interval. One block consisted of eight stimulus presentations to one eye, followed by eight stimulus presentations to the other eye. The order in which orientation was shown, and which eye was shuttered first, was (pseudo)randomized over an 8-block imaging session.

2.3.6. Two-photon imaging

In a pilot experiment aiming to quantify the long-term survival and ramp-up of rabies virus-traced neurons, repeated structural two-photon imaging was employed. Mice were lightly anesthetized with FMM as described above, body temperature was maintained at 37°C using a heat pad, and the eyes were protected from drying using Isopto-Max eye cream. Mice were fixed in place by the implanted headbar.

The imaging setup used a tunable Ti:Sapphire laser (pulse width: 100fs; pulse frequency: 80MHz) with a pre-chirp unit, set to 920nm wavelength. Laser power was controlled using a Pockels cell and adjusted based on the depth of the imaging plane and strength of fluorescence expression. The microscope was fitted with a 16x water immersion objective (0.8 NA, Nikon) a dichroic filter to allow simultaneous imaging of green (eGFP) and red (tdTomato) emission, and two GaAsP photon multiplier tubes (PMTs), each fitted with a bandpass filter (525/50-25nm or 607/70-25 nm). Diluted ultrasound gel (three parts gel, one part water) was applied to the cranial window of the anesthetized mouse as immersion medium. Structural stacks were obtained for one to four fields of view (FOVs) in the visual cortex of each mouse, depending on the spread of rabies virus expression and the quality and clarity of the cranial window. Each FOV was 512 x 512 pixels, and approximately 500 x 500µm in size, with a 3-4µm step between imaging planes. FOVs were imaged every three to six days for four weeks following rabies virus injection.

2.3.7. Perfusion

Mice were deeply anesthetized with an overdose of FMM (1.5-2.5x normal dose). After foot pinch reflex yielded no response, mice were fixed in place and the chest cavity was

opened to allow a needle to be inserted into the right ventricle. Animals were first perfused with 15-20mL of ice-cold saline containing lidocaine (0.1%) and heparin (1 U/mL), and then 20-25mL of ice-cold 4% PFA. Brains were immediately dissected and post-fixed in PFA for 24 hours.

2.4. Whole brain processing and imaging

2.4.1. Brain clearing

Perfused whole brains were cleared to allow for imaging of thick (1mm) slices that preserved a great degree of axonal and dendritic branching in a single slice. Tissue clearing was performed with the X-Clarity™ aqueous clearing system as follows: Brains were post-fixed in 4% PFA for 24 hours after perfusion to ensure crosslinkage of proteins, rinsed in PBS for 24 hours at 4°C, and then infused with activated X-Clarity™ hydrogel solution for 24 hours at 4°C. After infusion, brains submerged in hydrogel solution were polymerized at 37°C, -80kPa vacuum, for 3 hours, to induce formation of the tissue-gel hybrid. Brains were immediately rinsed with PBS to remove viscous hydrogel and prevent it from sticking to the tissue. Brains were then moved to clean Falcon tubes with 50mL of PBS, protected from light with aluminum foil, and placed on a rocker at room temperature for at least 5 hours to ensure proper rinsing of the hydrogel solution.

After rinsing, lipids were removed from the brain via electrophoretic tissue clearing. Each polymerized brain was placed in a tissue holder and lowered into the electrophoresis chamber of the X-Clarity™ tissue clearing machine. The chamber contained sodium dodecyl sulfate (SDS)-based electrophoretic tissue clearing (ETC) solution, which was warmed and circulated through the chamber via a control tower. The machine was run for 8 to 10 hours, with a -0.8 ampere current provided by the electrodes within the chamber. ETC solution was warmed to 37°C and circulated at 50 RPMs.

After the tissue was cleared, it was rinsed using PBS and stored at 4°C in PBS until slicing. Brains were sliced coronally to 1mm thickness while submerged in PBS on a vibratome. Slices were incubated in a 1:1000 dilution of DAPI in PBS for 48 hours at room temperature, and then rinsed and stored in PBS in 12-well plates at 4°C. Slices stored in PBS became translucent.

2.4.2. Confocal imaging

Cleared slices were mounted on glass slides fitted with 900µm spacers in X-Clarity™ mounting medium, a refractive index matching solution, and covered with a cover glass. Slices were mounted at least 8 hours before imaging so that the tissue would be clear, rather than translucent, at the start of imaging.

Cleared slices were imaged at Leica confocal microscopes (TCS SP8, Stellaris 5 DMi8, Stellaris 5 DM6), using 10x air objectives (SP8 objective NA: 0.3; Stellaris objective NA: 0.4). Four channels were imaged: DAPI (405nm excitation), mTurquoise2 (458nm excitation), eGFP (488nm excitation), and tdTomato (561nm excitation), with a pixel size of 1µm x 1µm. A 20µm z-step was used, as it was sufficient to image neuronal cell bodies in at least one plane. Scanning rate was set to 600Hz (bidirectionally). Tiles were imaged

with a 10% overlap to enable online stitching. Images were stored using the Leica imaging format (".lif") and later exported to TIF format.

Slices may have been imaged more than once, indicated by "_redo" in Table 1. Reasons for reimaging a slice include corrupted data files, errors resulting in missing channels or missing planes, or issues with swelling of the slice that resulted in being unable to stitch the imaging tiles properly.

2.5. Image processing and analysis

2.5.1. *In vitro* cell counting

Confocal images of either the whole culture or of two regions of interest, one from CA1 and one from CA3, were opened in LAS-X software. The cell annotation tool was used to manually annotate neurons based on which fluorophore(s) they expressed. Cell counts for each expression pattern (eGFP-only, tdTomato-only, or double-labeled) were recorded.

2.5.2. Whole-brain image processing

To quantify how many rabies virus-infected neurons were present in each brain region, and which fluorophore(s) they expressed, the following processing steps were implemented. Images obtained with confocal microscopy were exported to necessary formats (section 2.5.2.1). Then, neurons were segmented from background (2.5.2.2), and classified based on fluorescence in the eGFP and tdTomato channels (2.5.2.3). In parallel, images were registered to the Allen Brain Atlas, such that each neuron could be assigned to a brain region (2.5.2.4). Finally, data from segmentation, classification, and registration steps were merged (2.5.2.5) and analyzed.

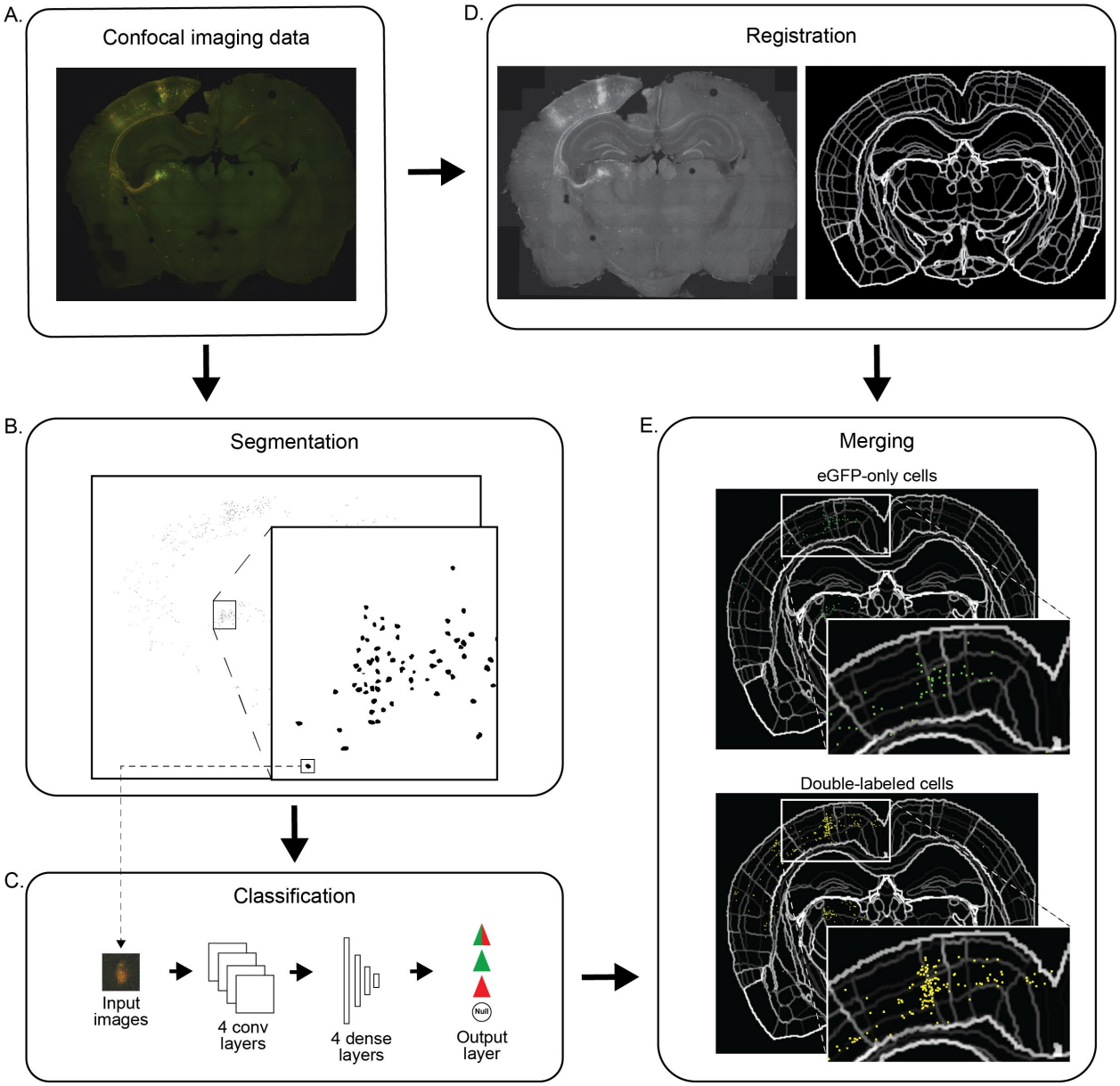

Figure 2.1 | Whole-brain image processing steps. A. Images acquired with confocal microscopy are converted to TIFs. **B.** Example of output image from Arivis Cloud segmentation. Somas (black) are segmented from background (white). **C.** Classification of segmented somas using a custom convolutional neural network (CNN). Output layer reports whether the input is a neuron expressing eGFP, tdTomato, or both, or that the input is not a neuron. **D.** *Left:* Example of three-channel (eGFP, tdTomato, DAPI) image used for registration. *Right:* Example output from Visualign software, after adjusting the affine transform in QuickNII and the non-affine transform in Visualign. **E.** Example inputs to NUTIL software. *Top:* A green square (10 x 10 pixels) is centered on the X-Y coordinate for each neuron classified as eGFP-only in (C). *Bottom:* As at the top, for neurons that are classified as double-labeled.

2.5.2.1. Data preparation

Confocal images were exported from Leica image format (.lif) to single-plane, single-channel 8-bit TIF files, using LAS-X and custom Python scripts. For various further processing stages, merged images were created: tdTomato + eGFP TIFs (Fig. 2.1A) for segmentation and classification of neurons, and downsampled (to 2000 pixel width as recommended for QUINT software suite) tdTomato + eGFP + DAPI JPEGs (Fig. 2.1D) for registration. For the registration step only, pixel dimensions therefore varied between images. Helper virus data in the mTurquoise2 channel was analyzed separately.

2.5.2.2. Segmentation of fluorescently-labeled neurons

Neuron somas were segmented from background, in grayscale images of the tdTomato + eGFP channels, using segmentation models trained in the Arivis Cloud platform (Carl Zeiss Microscopy GmbH, 2023). In order to optimize model performance for variations in quality across brain slice imaging data, three instance segmentation models were trained and implemented. Models were trained on annotated whole-slice images from both control and monocularly deprived mice. The images were annotated using the Arivis Cloud platform, and annotations consisted of examples of pixels belonging to the "cell" and "background" classes. Training of the model is performed automatically in Arivis Cloud, and the details of the model and the training process are not made available to users.

Trained models were used to segment somas from background in two-dimensional (in contrast to volumetric segmentation) grayscale images, one per imaging plane, of the merged eGFP and tdTomato channels. Each slice was segmented with one model, and then the output was visually inspected for quality. In cases where the result of the segmentation did not consist primarily of segmented somas (i.e., blood vessels and neurites were additionally considered foreground), the slice was then segmented with another model, and the most accurate segmentation was selected for further processing. The output consisted of one binary image for each plane, denoting somas versus background (Fig. 2.1B), and a CSV file containing data for each segment, including centroid, area, and eccentricity.

Model 1 was trained on four images: two from one mouse (MD group), and one each from two mice (one control, one MD). Model 1 was used to segment neurons in the images with the best imaging quality and perfusion quality (note that perfusion quality influences the degree of autofluorescence of structures like blood vessels) (126 slices). Model 2 was trained on one image from each of three mice (two MD, one control) and was used to segment neurons in images with lower quality, primarily due to low-quality perfusions (73 slices). By using two different models in this processing step, I was able to process qualitatively different imaging data, such that the data could be analyzed together at later steps. A third model was trained on ten images from six mice (three control, three MD) and was applied to images with poor imaging quality (e.g., artifacts due to swelling of tissue or incorrect settings in the microscope software). However, no iteration of this model was able to accurately segment neurons in the poor-quality images, so these slices were excluded from analysis (ten slices). The model used for each slice, as well as which slices are excluded, are described in Table 1.

2.5.2.3. Classification of fluorescently-labeled neurons

I determined the pattern of fluorescent protein expression for each segmented neuron with a custom convolutional neural network (CNN), developed with Pieter Goltstein. The inputs to the CNN were 34 x 34 pixel images of segments (putatively neurons) identified by the Arivis Cloud segmentation model and taken from the merged eGFP + tdTomato TIFs (Fig. 2.1C, left). The network had four convolutional layers: two 3×3 layers, with 4

and 8 channels, respectively, and two 5 x 5 layers, with 16 and 32 channels, respectively. Max pooling (2 x 2) was applied after each of these convolutional layers. Four fully-connected layers followed, with 64, 32, 16, and 8 channels, respectively. The last fully-connected layer was connected to a four-channel output layer, with each channel corresponding to a neuron class: eGFP-only, double-labeled, tdTomato-only, or "null," which indicated that the segmented image did not contain a soma.

The network was trained using the RMSprop optimizer on repeated batches of 32 samples, drawn equally from the training data. The network was trained with a dataset containing 37,418 images that had been manually assigned to one of the four classes by a trained observer. These data were taken from six slices, sampled from five mice (1 MD, 4 controls). The dataset was split, such that 80% of the images were used for training, and 20% for validation.

The segment classification network performed at 96% correct, with precision and recall varying slightly across the four classes (precision: eGFP-only: 0.96, double-labeled: 0.97, tdTomato-only: 1.0, null: 0.97; recall: eGFP-only: 0.98, double-labeled: 0.94, tdTomato-only: 0.90, null: 0.99).

Furthermore, the performance of the model was verified for each slice, by inspecting a subset of the segments classified into each of the four groups.

2.5.2.4. Registration

Brains were registered to the Allen Brain Atlas common reference coordinate framework (Wang et al., 2020) using the QUINT suite of software (Yates et al., 2019). The down-sampled JPEGs of the eGFP, tdTomato, and DAPI channels were used in registration steps. For each optical section (plane) of each slice, the parameters of the affine transform between the imaging data and the atlas template were manually adjusted using QuickNII (QUINT suite), and then non-affine transforms were manually adjusted with Visualign (Fig. 2.1D; Puchades et al., 2019).

2.5.2.5. Merging segmentation and registration

Segmented and classified neurons were assigned to their corresponding brain regions with NUTIL, a software tool from the QUINT suite (Groeneboom et al., 2020). The inputs to NUTIL are FLAT files containing registration data from Visualign for each slice, and binary PNGs, where each neuron of one class are represented by a 10 x 10 pixel square centered on the X-Y coordinate provided by the Arivis Cloud segmentation. To preserve information about the neuron's class, NUTIL was run separately for eGFP-only neurons, and for double-labeled neurons (Fig. 2.1E).

Data were compiled into a data frame such that each row contained the following features for a given neuron: brain region, class (determined by fluorophores expressed), area of the segmented neuron, eccentricity of the segmented neuron, and whether the neuron was located in the left or right hemisphere.

The brain regions reported by NUTIL provided the highest level of detail (e.g., cortical (sub)layers). To reduce the number of areas to report, brain regions assigned by NUTIL were grouped together into 21 broader brain regions, as described in Table 2.

2.5.3. IOS ocular dominance imaging analysis

Image sequences acquired with IOS imaging were processed and analyzed using custom Python scripts. For each trial (one stimulus presentation to one eye), a baseline reflectance value was calculated by averaging the first three frames (1.5s) and then subtracted from each frame in the trial. These values were then each divided by the baseline value, resulting in a measure of change in reflectance as a fraction of baseline reflectance (ΔR/R). A trial average for each pixel was calculated by averaging the ΔR/R in frames from 1s after stimulus onset to 1s after stimulus offset. A grand average was calculated from all trials in all blocks (one block = one stimulus presentation for each of eight grating orientations, for one eye) of responses to stimulation of the ipsilateral eye in order to identify the binocular region of visual cortex. A threshold value of the most responsive pixels (those with negative ΔR/R, indicating less reflectance of red light) was manually implemented. This region of maximal activation in the grand average was used as a mask for all trials for both eyes. Only the pixels inside the mask were included in further processing. A blockwise average was calculated for each eye. These were used to calculate the ocular dominance index (ODI):

$$ODI = \frac{contra - ipsi}{contra + ipsi}$$

ODI was calculated for each block of trials, and averaged over eight blocks to calculate the session ODI. Activation plots of mean amplitude over time were visually inspected for each trial to verify quality of acquisition.

2.5.4. IOS retinotopy analysis

Retinotopic imaging analysis was performed with custom MATLAB scripts as described previously (Goltstein et al., 2021). Briefly, data were processed separately for each of the 12 retinotopic stimulus locations. A baseline value was calculated by averaging responses over 5s, lasting from 6s to 1s preceding stimulus onset. Responses to the stimulus were calculated for the period 1s to 6s following stimulus onset, relative to the baseline value. Response maps were then averaged over trials and smoothed, then normalized to a value between 0 and 1, to allow comparing response strength across all 12 retinotopic stimuli. To compile a map of retinotopic preference in the imaged cortex, each pixel was assigned a color corresponding to the retinotopic region that evoked the strongest response.

2.5.5. Statistics

Data are reported as mean ± standard error of the mean, unless otherwise noted. We assume that the distribution of counts of fluorescently labeled neurons approximates a normal distribution. This is because the underlying process leading to this observation is likely stemming from a Poisson distribution, and λ (number of labeled cells) is large. Therefore, parametric tests are used in comparing brain regions with a mean higher than

100 neurons per mouse, and observations in 10 or more mice per group. For comparisons involving multiple brain regions, two-way analysis of covariance, (referred to as "ANCOVA" for the remainder) and Tukey's honestly significant difference (HSD) post-hoc tests are used. For comparisons of whole brain measurements, two-sample independent t-tests (referred to as "t-test" for the remainder) are used. Functional imaging data are tested for normality and compared using paired t-tests.

For experiments with low sample size (see section 3.2.1, . Quantification of Timeframe 1 snapshot efficacy), Kruskal-Wallis tests are used to compare data that is not normally distributed.

One-way analysis of variance (ANOVA) tests with Tukey's HSD post-hoc tests were used to assess results from *in vitro* experiments (see section 3.1) because, unlike in the cases where ANCOVA is used, there was no hypothesized covariate.

Table 1. Slices in TTT *in vivo* experiments segmented with each model.

0717A_slice10	Model 1
0717A_slice11	Model 1
0717A_slice4	Model 1
0717A_slice5	Model 1
0717A_slice6_redo	Model 2
0717A_slice7	Model 1
0717A_slice8	Model 1
0717A_slice8_redo	Model 1
0717C_slice10	Model 2
0717C_slice11	Model 2
0717C_slice3	Model 2
0717C_slice4_left	Model 1
0717C_slice4_right	Model 2
0717C_slice5	Model 2
0717C_slice6	Model 2
0717C_slice7	Model 2
0717C_slice8	Model 2
0717C_slice9	Model 2
0717D_slice10	Model 1
0717D_slice3	Model 1
0717D_slice4	Model 1
0717D_slice5	Model 1
0717D_slice6	Model 1
0717D_slice7	Model 1
0717D_slice8	Model 1

0717D_slice9	Model 1
0718A_slice1	Model 1
0718A_slice2_redo	Model 1
0718A_slice3_redo	Model 1
0718A_slice5	Model 1
0718A_slice7	Model 1
0718A_slice8_hemi	Model 2
0718A_slice8_mid	Model 1
0718B_slice0	Model 1
0718B_slice1_redo	Model 1
0718B_slice2_DAPItest	Model 1
0718B_slice3_redo	Model 1
0718B_slice4_hemi	Model 1
0718B_slice4_mid	Model 1
0718F_slice2	Model 2
0718F_slice3	Model 1
0718F_slice4_redo	Model 2
0718F_slice5_redo	Model 2
0718F_slice6_left	Model 2
0718F_slice6_right	Model 2
0718F_slice7	Model 1
0729A_slice2	Model 2
0729A_slice3	Model 1
0729A_slice4_redo	Model 1
0729A_slice5_redo	Model 1

0729A_slice6	Model 1
0729A_slice7	Model 1
0729B_slice2_redo	Model 1
0729B_slice3_redo	Model 1
0729B_slice4_redo	Model 1
0729B_slice7_redo	Model 1
0729C_slice4	Model 1
0729C_slice5	Model 1
0729C_slice6	Model 1
0729C_slice7_redo	Model 1
0730D_slice2	Model 1
0730D_slice5	Model 1
0730D_slice6	Model 2
0730D_slice7	Model 1
0730D_slice8	Model 1
0730E_slice1_hemi	Model 1
0730E_slice1_mid	Model 1
0730E_slice2	Model 1
0730E_slice3	Model 1
0730E_slice4_redo	Model 1
0730E_slice5	Model 1
0730E_slice6	Model 1
0730E_slice7	Model 1
0730F_slice2	Model 1
0730F_slice3_redo	Model 1
0730F_slice4_redo	Model 1
0730F_slice5	Model 2
0730F_slice6	Model 1
0730H_slice1	Model 2
0730H_slice2	Model 2
0730H_slice3	Model 2
0730H_slice4_redo	Model 2
0730H_slice5	Model 2
0802A_slice5	Model 2
0802A_slice6	Model 2
0802A_slice7	Model 2
0802A_slice8	Model 2
0802A_slice9	Model 2
0802B_slice2A	Model 1
0802B_slice2B	Model 2
0802B_slice6	Model 2
0802B_slice7	Model 2
0802B_slice8	Model 2
0802B_slice9	Model 2
0802C_slice4	Model 1
0802C_slice5	Model 1
0802C_slice6	Model 1
0802C_slice7	Model 1
0802C_slice8	Model 1
0802D_slice2	Model 1
0802D_slice3	Model 2
0802D_slice4	Model 2
0802D_slice5	Model 2
0802D_slice6	Model 2
0802D_slice8	Model 2
0802F_slice10	Model 2
0802F_slice11	Model 2
0802F_slice12	Model 1
0802F_slice5	Model 2
0802F_slice6	Model 1
0802F_slice7	Model 2
0802F_slice8	Model 2
0802F_slice9	Model 1
0802F_slice9_redo	Model 1
0802G_slice4_left	Model 1
0802G_slice4_right	Model 1
0802G_slice5	Model 2
0802G_slice6	Model 1
0802G_slice7	Model 2
0802G_slice8	Model 2
0802H_slice5	Model 1
0802H_slice6	Model 1
0802I_slice3	Model 1
0802I_slice4	Model 1
0802I_slice5	Model 1
0802I_slice6	Model 2
0807C_slice2_redo	Model 1
0807C_slice3_redo	exclude
0807C_slice4_redo	Model 2
0807C_slice5	Model 1
0807C_slice6	Model 1
0807D_slice2	Model 2

0807D_slice3	Model 1
0807D_slice4	Model 1
0807D_slice5_redo	Model 1
0807D_slice6	Model 1
0807D_slice7	Model 1
0807G_slice2_hemi	Model 1
0807G_slice2_mid	Model 1
0807G_slice3_redo	Model 1
0807G_slice4	Model 1
0807G_slice5_redo	Model 1
0807G_slice6	exclude
0807G_slice7	exclude
0807G_slice8	Model 2
0807H_slice1	Model 1
0807H_slice2_redo	exclude
0807H_slice3_cropped	Model 1
0807H_slice4	Model 1
0807H_slice5	Model 1
0807H_slice6	Model 1
0807H_slice7	Model 1
0807I_slice2_redo	exclude
0807I_slice3	Model 1
0807I_slice4_redo	exclude
0807I_slice5_lefthemi	Model 1
0807I_slice5_redo_righthemi	Model 1
0807I_slice6	exclude
0807I_slice7	exclude
0807I_slice8	Model 1
0815A_slice10	Model 2
0815A_slice11	Model 2
0815A_slice12	Model 2
0815A_slice5_left	Model 2
0815A_slice5_right	Model 2
0815A_slice6	Model 2
0815A_slice7	Model 2
0815A_slice8	Model 2
0815A_slice9	exclude
0919A_slice10	Model 2
0919A_slice7	Model 2
0919A_slice9	Model 2
0919B_slice10	Model 2
0919B_slice6_left	Model 1
0919B_slice6_right	Model 2
0919B_slice7	Model 2
0919B_slice8	Model 2
0919B_slice9	Model 1
0919D_slice10	Model 2
0919D_slice11	Model 2
0919D_slice12	Model 2
0919D_slice9_left	Model 2
0919D_slice9_right	Model 2
0920F_slice2_left	Model 1
0920F_slice2_right	Model 1
0920F_slice3	Model 1
0920F_slice4	exclude
0920F_slice5	Model 1
0920F_slice6	Model 1
0920G_slice10	Model 1
0920G_slice11	Model 1
0920G_slice12	Model 1
0920G_slice13	Model 1
0920G_slice8_left	Model 1
0920G_slice8_right	Model 2
0920G_slice9_left	Model 1
0920G_slice9_right	Model 1
0920I_slice4	Model 1
0920I_slice5_left	Model 1
0920I_slice5_right	Model 1
0920I_slice6	Model 1
0920I_slice7	Model 1
0920I_slice8	Model 1
0920J_slice10	Model 1
0920J_slice11	Model 1
0920J_slice12	Model 1
0920J_slice13	Model 1
0920J_slice8_left	Model 2
0920J_slice9	Model 1

Table 2. Brain region grouping

Abbreviated region name	Region description	NUTIL brain regions included
VIS	Visual cortical areas	'Anterior area, layer 1', 'Anterior area, layer 2/3', 'Anterior area, layer 4', 'Anterior area, layer 5', 'Anterior area, layer 6a', 'Anterior area, layer 6b', 'Anterolateral visual area, layer 1', 'Anterolateral visual area, layer 2/3', 'Anterolateral visual area, layer 4', 'Anterolateral visual area, layer 5', 'Anterolateral visual area, layer 6a', 'Anterolateral visual area, layer 6b', 'Anteromedial visual area, layer 1', 'Anteromedial visual area, layer 2/3', 'Anteromedial visual area, layer 4', 'Anteromedial visual area, layer 5', 'Anteromedial visual area, layer 6a', 'Anteromedial visual area, layer 6b', 'Lateral visual area, layer 1', 'Lateral visual area, layer 2/3', 'Lateral visual area, layer 4', 'Lateral visual area, layer 5', 'Lateral visual area, layer 6', 'Lateral visual area, layer 6a', 'Lateral visual area, layer 6b', 'Laterointermediate area, layer 1', 'Laterointermediate area, layer 2/3', 'Laterointermediate area, layer 4', 'Laterointermediate area, layer 5', 'Laterointermediate area, layer 6a', 'Laterointermediate area, layer 6b', 'Posterolateral visual area, layer 1', 'Posterolateral visual area, layer 2/3', 'Posterolateral visual area, layer 4', 'Posterolateral visual area, layer 5', 'Posterolateral visual area, layer 6a', 'Posterolateral visual area, layer 6b', 'Postrhinal area, layer 1',

		'Postrhinal area, layer 2/3', 'Postrhinal area, layer 4', 'Postrhinal area, layer 5', 'Postrhinal area, layer 6a', 'Postrhinal area, layer 6b', 'Primary visual area, layer 1', 'Primary visual area, layer 2/3', 'Primary visual area, layer 4', 'Primary visual area, layer 5', 'Primary visual area, layer 6a', 'Primary visual area, layer 6b', 'Rostrolateral area, layer 1', 'Rostrolateral area, layer 2/3', 'Rostrolateral area, layer 4', 'Rostrolateral area, layer 5', 'Rostrolateral area, layer 6', 'Rostrolateral area, layer 6a', 'Rostrolateral area, layer 6b', 'posteromedial visual area, layer 1', 'posteromedial visual area, layer 2/3', 'posteromedial visual area, layer 4', 'posteromedial visual area, layer 5', 'posteromedial visual area, layer 6a', 'posteromedial visual area, layer 6b'
V1	Primary visual cortex	'Primary visual area, layer 1', 'Primary visual area, layer 2/3', 'Primary visual area, layer 4', 'Primary visual area, layer 5', 'Primary visual area, layer 6a', 'Primary visual area, layer 6b'
HVAs	Higher visual areas	'Anterior area, layer 1', 'Anterior area, layer 2/3', 'Anterior area, layer 4', 'Anterior area, layer 5', 'Anterior area, layer 6a', 'Anterior area, layer 6b', 'Anterolateral visual area, layer 1', 'Anterolateral visual area, layer 2/3', 'Anterolateral visual area, layer 4', 'Anterolateral visual area, layer 5', 'Anterolateral visual area, layer 6a', 'Anterolateral visual area, layer 6b', 'Anteromedial visual area, layer 1',

		'Anteromedial visual area, layer 2/3', 'Anteromedial visual area, layer 4', 'Anteromedial visual area, layer 5', 'Anteromedial visual area, layer 6a', 'Anteromedial visual area, layer 6b', 'Lateral visual area, layer 1', 'Lateral visual area, layer 2/3', 'Lateral visual area, layer 4', 'Lateral visual area, layer 5', 'Lateral visual area, layer 6', 'Lateral visual area, layer 6a', 'Lateral visual area, layer 6b', 'Laterointermediate area, layer 1', 'Laterointermediate area, layer 2/3', 'Laterointermediate area, layer 4', 'Laterointermediate area, layer 5', 'Laterointermediate area, layer 6a', 'Laterointermediate area, layer 6b', 'Posterolateral visual area, layer 1', 'Posterolateral visual area, layer 2/3', 'Posterolateral visual area, layer 4', 'Posterolateral visual area, layer 5', 'Posterolateral visual area, layer 6a', 'Posterolateral visual area, layer 6b', 'Postrhinal area, layer 1', 'Postrhinal area, layer 2/3', 'Postrhinal area, layer 4', 'Postrhinal area, layer 5', 'Postrhinal area, layer 6a', 'Postrhinal area, layer 6b', 'Rostrolateral area, layer 1', 'Rostrolateral area, layer 2/3', 'Rostrolateral area, layer 4', 'Rostrolateral area, layer 5', 'Rostrolateral area, layer 6', 'Rostrolateral area, layer 6a', 'Rostrolateral area, layer 6b', 'posteromedial visual area, layer 1', 'posteromedial visual area, layer 2/3', 'posteromedial visual area, layer 4', 'posteromedial visual area, layer 5', 'posteromedial visual area, layer 6a', 'posteromedial visual area, layer 6b'

dLGN	Dorsal lateral geniculate nucleus of the thalamus	Manually defined
LP	Lateral posterior nucleus of the thalamus	Manually defined
LD	Lateral dorsal nucleus of the thalamus	Manually defined
RSP	Retrosplenial cortex	'Retrosplenial area, dorsal part, layer 1', 'Retrosplenial area, dorsal part, layer 2/3', 'Retrosplenial area, dorsal part, layer 5', 'Retrosplenial area, dorsal part, layer 6a', 'Retrosplenial area, dorsal part, layer 6b', 'Retrosplenial area, lateral agranular part, layer 1', 'Retrosplenial area, lateral agranular part, laer 2/3', 'Retrosplenial area, lateral agranular part, layer 4', 'Retrosplenial area, lateral agranular part, layer 5', 'Retrosplenial area, lateral agranular part, layer 6a', 'Retrosplenial area, lateral agranular part, layer 6b', 'Retrosplenial area, ventral part, layer 1', 'Retrosplenial area, ventral part, layer 2/3', 'Retrosplenial area, ventral part, layer 4', 'Retrosplenial area, ventral part, layer 5', 'Retrosplenial area, ventral part, layer 6a', 'Retrosplenial area, ventral part, layer 6b'
Thal	Thalamus	'Anterodorsal nucleus', 'Anteromedial nucleus, dorsal part', 'Anteromedial nucleus, ventral part', 'Anteroventral nucleus of thalamus', 'Central lateral nucleus of the thalamus', 'Central medial nucleus of the thalamus', 'Dorsal part of the lateral geniculate complex, core', 'Dorsal part of the lateral geniculate complex, ipsilateral zone', 'Dorsal part of the lateral geniculate complex, shell', 'Ethmoid nucleus of the thalamus', 'Interanterodorsal nucleus of the thalamus', 'Interanteromedial nucleus of the thalamus', 'Intergeniculate leaflet of the lateral geniculate complex', 'Intermediate geniculate nucleus', 'Intermediodorsal nucleus of the thalamus',

		'Lateral dorsal nucleus of thalamus', 'Lateral posterior nucleus of the thalamus', 'Medial geniculate complex, dorsal part', 'Medial geniculate complex, medial part', 'Medial geniculate complex, ventral part', 'Mediodorsal nucleus of thalamus', 'Paracentral nucleus', 'Paraventricular nucleus of the thalamus', 'Posterior complex of the thalamus', 'Posterior intralaminar thalamic nucleus', 'Posterior limiting nucleus of the thalamus', 'Reticular nucleus of the thalamus', 'Submedial nucleus of the thalamus', 'Thalamus', 'Ventral anterior-lateral complex of the thalamus', 'Ventral medial nucleus of the thalamus', 'Ventral part of the lateral geniculate complex', 'Ventral posterolateral nucleus of the thalamus', 'Ventral posterolateral nucleus of the thalamus, parvicellular part', 'Ventral posteromedial nucleus of the thalamus', 'Ventral posteromedial nucleus of the thalamus, parvicellular part'
HPF	Hippocampal formation	'Dentate gyrus, granule cell layer', 'Dentate gyrus, molecular layer', 'Dentate gyrus, polymorph layer', 'Entorhinal area, lateral part, layer 1', 'Entorhinal area, lateral part, layer 2', 'Entorhinal area, lateral part, layer 3', 'Entorhinal area, lateral part, layer 5', 'Entorhinal area, lateral part, layer 6a', 'Entorhinal area, medial part, dorsal zone, layer 1', 'Entorhinal area, medial part, dorsal zone, layer 2', 'Entorhinal area, medial part, dorsal zone, layer 3', 'Entorhinal area, medial part, dorsal zone, layer 5', 'Entorhinal area, medial part, dorsal zone, layer 6', 'Field CA1', 'Field CA2', 'Field CA3', 'Hippocampal formation', 'Parasubiculum', 'Postsubiculum', 'Prosubiculum', 'Subiculum', 'dorsal hippocampal commissure',

		'ventral hippocampal commissure'
SS	Somatosensory cortex	'Primary somatosensory area, barrel field, layer 1', 'Primary somatosensory area, barrel field, layer 2/3', 'Primary somatosensory area, barrel field, layer 4', 'Primary somatosensory area, barrel field, layer 5', 'Primary somatosensory area, barrel field, layer 6a', 'Primary somatosensory area, barrel field, layer 6b', 'Primary somatosensory area, lower limb, layer 1', 'Primary somatosensory area, lower limb, layer 2/3', 'Primary somatosensory area, lower limb, layer 4', 'Primary somatosensory area, lower limb, layer 5', 'Primary somatosensory area, lower limb, layer 6a', 'Primary somatosensory area, lower limb, layer 6b', 'Primary somatosensory area, mouth, layer 1', 'Primary somatosensory area, mouth, layer 2/3', 'Primary somatosensory area, mouth, layer 4', 'Primary somatosensory area, mouth, layer 5', 'Primary somatosensory area, mouth, layer 6a', 'Primary somatosensory area, mouth, layer 6b', 'Primary somatosensory area, nose, layer 1', 'Primary somatosensory area, nose, layer 2/3', 'Primary somatosensory area, nose, layer 4', 'Primary somatosensory area, nose, layer 5', 'Primary somatosensory area, nose, layer 6a', 'Primary somatosensory area, nose, layer 6b', 'Primary somatosensory area, trunk, layer 1', 'Primary somatosensory area, trunk, layer 2/3', 'Primary somatosensory area, trunk, layer 4', 'Primary somatosensory area, trunk, layer 5', 'Primary somatosensory area, trunk, layer 6a', 'Primary somatosensory area, trunk, layer 6b', 'Primary somatosensory area, unassigned, layer 1', 'Primary somatosensory area, unassigned, layer 2/3', 'Primary somatosensory area, unassigned, layer 4', 'Primary somatosensory area, unassigned, layer 5', 'Primary somatosensory area, unassigned, layer 6a', 'Primary somatosensory area, unassigned, layer 6b', 'Primary somatosensory area, upper limb, layer 1', 'Primary somatosensory area, upper limb, layer 2/3', 'Primary somatosensory area, upper limb, layer 4', 'Primary somatosensory area, upper limb, layer 5', 'Primary somatosensory area, upper limb, layer 6a', 'Primary somatosensory area, upper limb, layer 6b',

		'Supplemental somatosensory area, layer 1', 'Supplemental somatosensory area, layer 2/3', 'Supplemental somatosensory area, layer 4', 'Supplemental somatosensory area, layer 5', 'Supplemental somatosensory area, layer 6a', 'Supplemental somatosensory area, layer 6b'
AUD	Auditory cortex	'Dorsal auditory area, layer 1', 'Dorsal auditory area, layer 2/3', 'Dorsal auditory area, layer 5', 'Dorsal auditory area, layer 6a', 'Dorsal auditory area, layer 6b', 'Posterior auditory area, layer 2/3', 'Posterior auditory area, layer 4', 'Posterior auditory area, layer 5', 'Posterior auditory area, layer 6a', 'Posterior auditory area, layer 6b', 'Primary auditory area, layer 1', 'Primary auditory area, layer 2/3', 'Primary auditory area, layer 5', 'Primary auditory area, layer 6a', 'Ventral auditory area, layer 1', 'Ventral auditory area, layer 2/3', 'Ventral auditory area, layer 4', 'Ventral auditory area, layer 5', 'Ventral auditory area, layer 6a', 'Ventral auditory area, layer 6b'
MO	Motor cortex	'Primary motor area, Layer 1', 'Primary motor area, Layer 2/3', 'Primary motor area, Layer 4', 'Primary motor area, Layer 5', 'Primary motor area, Layer 6a', 'Primary motor area, Layer 6b', 'Secondary motor area, layer 1', 'Secondary motor area, layer 2/3', 'Secondary motor area, layer 5', 'Secondary motor area, layer 6a', 'Secondary motor area, layer 6b'
TEa	Temporal association areas	'Temporal association areas, layer 1', 'Temporal association areas, layer 2/3', 'Temporal association areas, layer 4', 'Temporal association areas, layer 5', 'Temporal association areas, layer 6a', 'Temporal association areas, layer 6b'

InC	Insular cortex	'Agranular insular area, dorsal part, layer 1', 'Agranular insular area, dorsal part, layer 5', 'Agranular insular area, dorsal part, layer 6a', 'Agranular insular area, dorsal part, layer 6b', 'Agranular insular area, posterior part, layer 1', 'Agranular insular area, posterior part, layer 2/3', 'Agranular insular area, posterior part, layer 5', 'Agranular insular area, posterior part, layer 6a', 'Agranular insular area, posterior part, layer 6b', 'Agranular insular area, ventral part, layer 5', 'Agranular insular area, ventral part, layer 6a'
ACC	Anterior cingulate cortex	'Anterior cingulate area, dorsal part, layer 1', 'Anterior cingulate area, dorsal part, layer 2/3', 'Anterior cingulate area, dorsal part, layer 5', 'Anterior cingulate area, dorsal part, layer 6a', 'Anterior cingulate area, dorsal part, layer 6b', 'Anterior cingulate area, ventral part, 6a', 'Anterior cingulate area, ventral part, 6b', 'Anterior cingulate area, ventral part, layer 1', 'Anterior cingulate area, ventral part, layer 2/3', 'Anterior cingulate area, ventral part, layer 5'
HY	Hypothalamus	'Anterior hypothalamic nucleus', 'Anterodorsal preoptic nucleus', 'Anteroventral preoptic nucleus', 'Arcuate hypothalamic nucleus', 'Dorsomedial nucleus of the hypothalamus', 'Hypothalamus', 'Lateral hypothalamic area', 'Paraventricular hypothalamic nucleus', 'Periventricular hypothalamic nucleus, anterior part', 'Periventricular hypothalamic nucleus, intermediate part', 'Periventricular hypothalamic nucleus, posterior part', 'Periventricular hypothalamic nucleus, preoptic part', 'Posterior hypothalamic nucleus', 'Ventrolateral preoptic nucleus', 'Ventromedial hypothalamic nucleus', 'Ventromedial preoptic nucleus'
GP	Globus pallidus	'Globus pallidus, external segment', 'Globus pallidus, internal segment'
IC	Inferior colliculus	'Inferior colliculus, dorsal nucleus', 'Inferior colliculus, external nucleus'
CLA	Claustrum	'Claustrum'

SC	Superior colliculus	'Superior colliculus, motor related, deep gray layer', 'Superior colliculus, motor related, deep white layer', 'Superior colliculus, motor related, intermediate gray layer', 'Superior colliculus, motor related, intermediate white layer', 'Superior colliculus, optic layer', 'Superior colliculus, superficial gray layer', 'Superior colliculus, zonal layer', 'brachium of the superior colliculus', 'superior colliculus commissure'
AMYG	Amygdala	'Anterior amygdalar area', 'Basolateral amygdalar nucleus, anterior part', 'Basolateral amygdalar nucleus, posterior part', 'Basolateral amygdalar nucleus, ventral part', 'Basomedial amygdalar nucleus, anterior part', 'Basomedial amygdalar nucleus, posterior part', 'Central amygdalar nucleus, capsular part', 'Central amygdalar nucleus, lateral part', 'Central amygdalar nucleus, medial part', 'Cortical amygdalar area, anterior part', 'Cortical amygdalar area, posterior part, lateral zone', 'Intercalated amygdalar nucleus', 'Lateral amygdalar nucleus', 'Medial amygdalar nucleus', 'Posterior amygdalar nucleus', 'amygdalar capsule'

3. Results

In this thesis, I aimed to establish two-timeframe monosynaptic rabies virus tracing as a tool that can be used to identify candidate brain regions contributing to a particular episode of learning and plasticity via changes in the strength of their connectivity. In this section, I explain three main steps towards establishing this tool: First, in an *in vitro* system, I confirmed functionality of the components needed for two-timeframe tracing (TTT), including a helper virus AAV, a rabies virus carrying genes for both a fluorophore and inducible Cre recombinase, a tdTomato reporter mouse line, and application of 4OHT to activate the inducible Cre recombinase.

The next experiments described are two verification experiments *in vivo*. The first of these aimed to establish how effectively 4OHT can induce tdTomato expression (the "snapshot") in rabies virus-infected neurons, so that the "false positive rate" (the fraction of Timeframe 1 neurons that are not captured in the tdTomato snapshot) could be estimated. The goals of the second experiment were to ensure a) that starter cells survive long enough to enable rabies virus tracing well into Timeframe 2, and b) that a majority of rabies virus-infected cells survive the full duration of the experiment, as well. These were achieved by injecting helper virus and rabies virus in visual cortex, and using repeated two-photon imaging of rabies virus-infected neurons over a one-month period of time.

At the end of this section, I present results from the final step in establishing TTT as a tool to investigate brain-wide changes in connectivity: benchmarking the tool by implementing it with a paradigm known to induce plasticity. I chose ocular dominance (OD) plasticity, induced by temporary monocular deprivation (MD), because it is one of the most established plasticity paradigms. Using TTT, I labeled inputs to binocular visual cortex (bV1) during Timeframe 1, as a baseline set of inputs, and during Timeframe 2, which corresponded to the episode of MD. I then analyzed the inputs to bV1 in each timeframe, in brain regions known to contribute to OD plasticity as well as throughout the brain.

3.1. *In vitro* TTT in organotypic cultures

In a set of proof-of-principle experiments to test the basic functionality of viral constructs, I used organotypic slice cultures from tdTomato mouse hippocampus and cortex. The use of an *in vitro* model allowed a sharp reduction in the amount of animal experiments that would have otherwise been needed to validate the components of this new tool. Additionally, expression of viral payload in these cultures is generally much quicker than *in vivo* in the mouse brain, and so outcomes of experiments could be assessed on shorter timescales.

A caveat to using cultures from tdTomato mice is that this Ai9 mouse line is known to have some "leaky" spurious expression of tdTomato, in the absence of Cre recombinase ("007909 - Ai9 or Ai9(RCL-tdT) Strain Details," n.d.). I indeed observed that most cultures contained a few neurons (between two and ten) expressing tdTomato, following injection of an AAV that did not express Cre, such as the helper virus. Although spurious expression is expected in the

mouse line, I found that spurious expression was highly correlated with whether some AAV had been injected. I investigated whether Cre recombinase could be inadvertently expressed by contamination of the helper virus, and confirmed through polymerase chain reaction (PCR) experiments that Cre is not expressed via that construct. The neurons that express tdTomato in the absence of Cre can be distinguished easily from neurons that express tdTomato after Cre-induced recombination of the transgene, because spurious expression is not as bright as true expression ("007909 - Ai9 or Ai9(RCL-tdT) Strain Details," n.d.). Taken together with the very low number of neurons in which spurious expression occurs, I do not consider this a problem for interpretation.

The experiments described in this section of the Results were performed together with my supervisor, Pieter Goltstein, as well as several Masters students who I supervised.

3.1.1. Viral vector tests

Available helper viruses for monosynaptic rabies virus tracing generally use a red fluorescent protein to label starter cells, which in our system would overlap with the red fluorescent protein expressed via the reporter gene in the tdTomato snapshot. I therefore replaced the mCherry fluorophore with an mTurquoise2 fluorophore in the pAAV-CMV-TVAmCherry-2A-oG plasmid, such that three distinct fluorophores would be expressed in TTT experiments (gift from Marco Tripodi; Addgene plasmid # 104330; Ciabatti et al., 2017). I chose to express both the TVA receptor and rabies virus glycoprotein, along with the mTurquoise2 fluorophore, in one bicistronic (i.e., containing genes for two proteins) viral vector.

I first tested whether the helper virus infects neurons and expresses its constructs. I injected virus (AAV1.hSyn.TVA.mTurquoise2.F2A.oG.WPRE.SV40) into the CA1 region of hippocampal slice cultures (n=18) from tdTomato reporter mice. I imaged live cultures using an epifluorescence microscope after one week's time to allow for ramp-up of expression of the viral payload. All cultures expressed mTurquoise2, in a dense cluster of "starter cells" located at the injection region (Fig. 3.1A, Supp. Fig. 5A), demonstrating that the virus is expressed in neurons.

Next, I confirmed that the helper virus expresses not only its fluorophore, but also the proteins necessary for monosynaptic rabies virus tracing. I injected rabies virus (RABV.N2c$^{\Delta G}$.eGFP.T2A.^{ERT2}Cre^{ERT2}(EnvA)) into CA1 of these cultures 8 days after the helper virus injection, targeting the injection to the area expressing mTurquoise2, as identified by epifluorescence imaging. Five days after rabies virus injection, I imaged the live cultures, and observed continued mTurquoise2 expression along with rabies virus eGFP expression (Fig. 3.1B, Supp. Fig. 5A). Expression of the rabies virus eGFP was present throughout the culture, not only in starter cells, as confirmed by overlaying epifluorescence images from each channel and comparing the extent of expression. In most cultures, the density of eGFP+ neurons was too high to allow for counting individual neurons accurately, providing evidence that rabies virus tracing is very efficient in this system. From these experiments, I concluded that the bicistronic helper virus: a) expresses a functional TVA receptor that allows rabies virus to enter starter cells and b) expresses sufficient glycoprotein to allow rabies virus to infect inputs to starter cells.

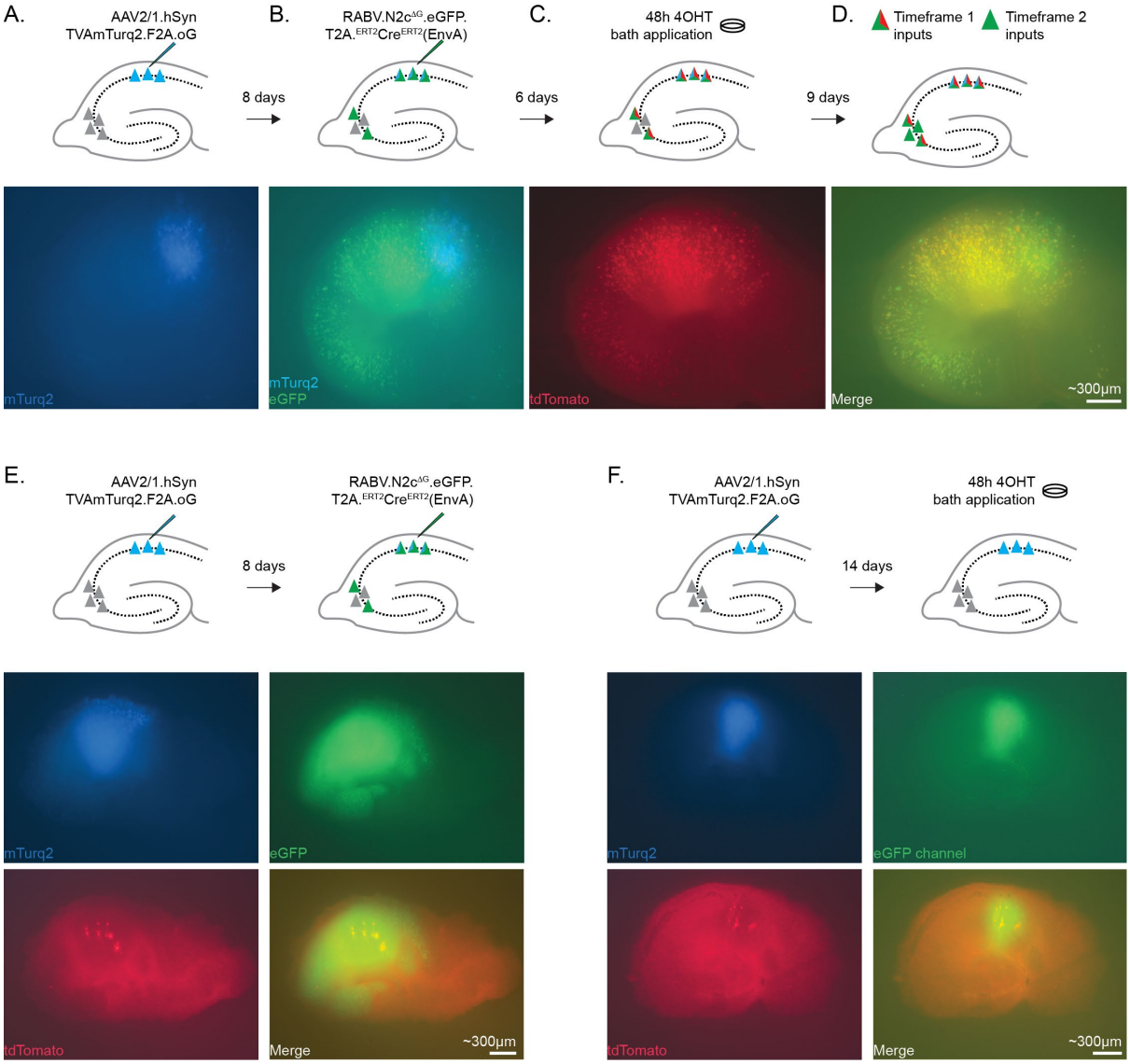

Figure 3.1 | *In vitro* validation of TTT components. A-D, Top: Schematic of TTT tracing method in organotypic hippocampal cultures, including intervals between each step (black arrows). **A-D, Bottom:** Epifluorescence images of an example culture expressing mTurquoise2, eGFP, and tdTomato after application of TTT constructs. All images were made in the same imaging session. The channel(s) displayed in each column are intended to show which fluorophore(s) are associated with each step of TTT. **A:** A helper virus AAV, expressing a TVA receptor-mTurquoise2 fusion protein, and optimized rabies virus glycoprotein (oG), is injected into CA1 of a tdTomato hippocampal organotypic culture. Blue triangles represent starter cells, which express the helper virus. Neurons in CA1 express mTurquoise2. **B:** EnvA-pseudotyped rabies virus carrying eGFP and inducible Cre is injected into CA1 eight days after helper virus injection. Starter cells express eGFP and mTurquoise2. Infected inputs to starter cells express eGFP. **C:** Cultures are moved to medium containing 1µM 4OHT for 48 hours to induce tdTomato snapshot. Rabies virus-infected inputs express eGFP and tdTomato. **D:** After 4OHT is removed, neurons newly infected over the subsequent days express only eGFP. **E:** *Top:* Schematic of TTT control experiment where 4OHT is excluded, but the timeline in A-D is otherwise followed. *Bottom:* Example culture injected with helper virus and then rabies virus, but not treated with 4OHT. Neurons in the injection region (CA1) expresses mTurquoise2 and eGFP. eGFP expression extends throughout the culture, reflecting traced neurons. Neurons expressing tdTomato are sparse, reflecting random spurious recombination in the mouse line used. **F:** *Top:* Schematic of TTT control experiment where rabies virus injection is excluded, but the timeline in A-D is otherwise followed. *Bottom:* Example culture injected with helper virus and treated with 4OHT. Bleedthrough of mTurquoise2 expression in the eGFP channel is visible, but eGFP is not expressed. tdTomato is expressed only sparsely, in the absence of Cre recombinase. **Epifluorescence images:** Organotypic hippocampal cultures are approximately 2.2mm x 1.3mm in size. Scaling is approximate and based on confocal images of organotypic cultures from other experiments.

3.1.2. tdTomato Snapshot tests

The goal of the snapshot at the end of Timeframe 1 is to label all neurons that are infected with rabies virus with a second fluorophore, tdTomato, so that these Timeframe 1 neurons can later be distinguished from eGFP-only Timeframe 2 neurons that were not yet infected at the time of the snapshot. Expression of tdTomato is dependent on three components being present in a given neuron: the tdTomato mouse reporter gene, inducible Cre recombinase carried by the rabies virus, and 4OHT induction of Cre activity. We tested whether excluding either rabies virus, or 4OHT, from an experiment in organotypic cultures from tdTomato reporter mice would lead to any degree of aberrant tdTomato expression.

To test if 4OHT is required for tdTomato expression in TTT, I excluded 4OHT treatment from a subset of cultures (n=2). In these cultures, I injected helper virus and rabies virus, and imaged in the mTurquoise2, eGFP, and tdTomato channels (Fig. 3.1E, Supp. Fig. 5B). tdTomato expression was seen in only very few (between two and ten) neurons in each culture, while rabies virus eGFP is observable in hundreds of neurons. This indicates that, without 4OHT, inducible Cre does not cause sizeable tdTomato expression.

To test whether helper virus and 4OHT alone could induce tdTomato expression, I injected helper virus, but not rabies virus, in two cultures. I treated these cultures with 4OHT two weeks after helper virus injection (Fig. 3.1F, top). tdTomato was limited to spurious expression in very few neurons in this condition, as well (Fig. 3.1F, bottom row images).

We additionally confirmed that, when all three components are present, tdTomato is expressed in rabies virus-infected neurons. Cultures expressing helper virus and rabies virus were treated with 4OHT for 48 hours, and imaged five days after treatment. We observed tdTomato expression colocalized with eGFP expression (Fig. 3.1D). The tdTomato snapshot is therefore dependent on both rabies virus infection and 4OHT treatment.

3.1.3. Temporal dynamics of 4OHT induction of Cre recombinase *in vitro*

In order for a neuron to undergo recombination of the transgene and thereby express tdTomato, the inducible Cre recombinase protein (carried by the rabies virus) must be expressed in the neuron at a time when 4OHT is at an active concentration. We therefore needed to quantify the overlap in the timeline of inducible Cre ramp-up, and 4OHT clearance. To do so, we used a non-transsynaptic, G-pseudotyped rabies virus that infects neurons via their axon terminals (RABV.N2c.dG.eGFP.T2A.ERT-CRE-ERT(N2cG)). As there are no starter cells for the virus to continue spreading transsynaptically from, only one “timeframe” is labeled. This means that, after 4OHT application, variations in how many eGFP-expressing neurons co-express tdTomato are likely due to relative differences in the time needed for expression of inducible Cre expression and the active concentration of 4OHT.

I first estimated how long it takes for inducible Cre to express after a neuron is infected with rabies virus, by injecting G-pseudotyped rabies virus, and then applying 4OHT after various time intervals (Fig. 3.2A). I then imaged the cultures and counted neurons expressing either eGFP, or tdTomato, or both fluorophores (Fig. 3.2B). Recombination and expression of the tdTomato snapshot should only occur in conditions where enough time passes between

rabies virus injection and 4OHT application. By quantifying how many infected neurons express only eGFP, and not tdTomato, we can estimate the percentage of neurons that did not have inducible Cre while 4OHT was present. The percentage of eGFP-only neurons, as a fraction of all infected cells, decreases as the time between rabies virus injection and 4OHT application increases (Fig. 3.2C). However, even when 4OHT is only present in the first day after rabies virus injection, most neurons are able to undergo recombination (Fig. 3.2C, far left bar; percent not expressing tdTomato: 12.1% ± 2.8%, n = 3 cultures). This result has two possible explanations, which are not mutually exclusive: that expression of rabies virus inducible Cre is rapid, and/or that 4OHT could remain at active concentration in the culture after cultures are moved from 4OHT-containing medium to normal cell culture medium.

I then investigated the second of these two possibilities in more detail. I estimated how long 4OHT remains at an active concentration by repeating the previously described experiment, but with only hours between rabies virus injection and 4OHT application. In addition to shortening this interval, I also shortened the duration of 4OHT application to only four hours, instead of 24 hours. Here, too, a majority of neurons express both tdTomato and eGFP. When 4OHT is applied immediately after rabies virus injection, and removed four hours later, only 41.4% ± 1% of neurons express only eGFP (n = 4 cultures, Fig. 3.2D, far left). Given that more than half of the neurons were still able to undergo recombination of the transgene, we concluded that the window in which 4OHT is at an active concentration is longer than expected.

In summary, from these experiments, we concluded that expression of inducible Cre is rather fast, and clearance of 4OHT is rather slow. We expect ramp-up of inducible Cre to be similarly fast *in vivo*, but expect to not face as much of a problem with 4OHT *in vivo*, because the mouse's metabolism of the compound is likely more effective than clearance of 4OHT in isolated organotypic cultures (Manns et al., 1993; Robertson and Katzenellenbogen, 1982; Valny et al., 2016).

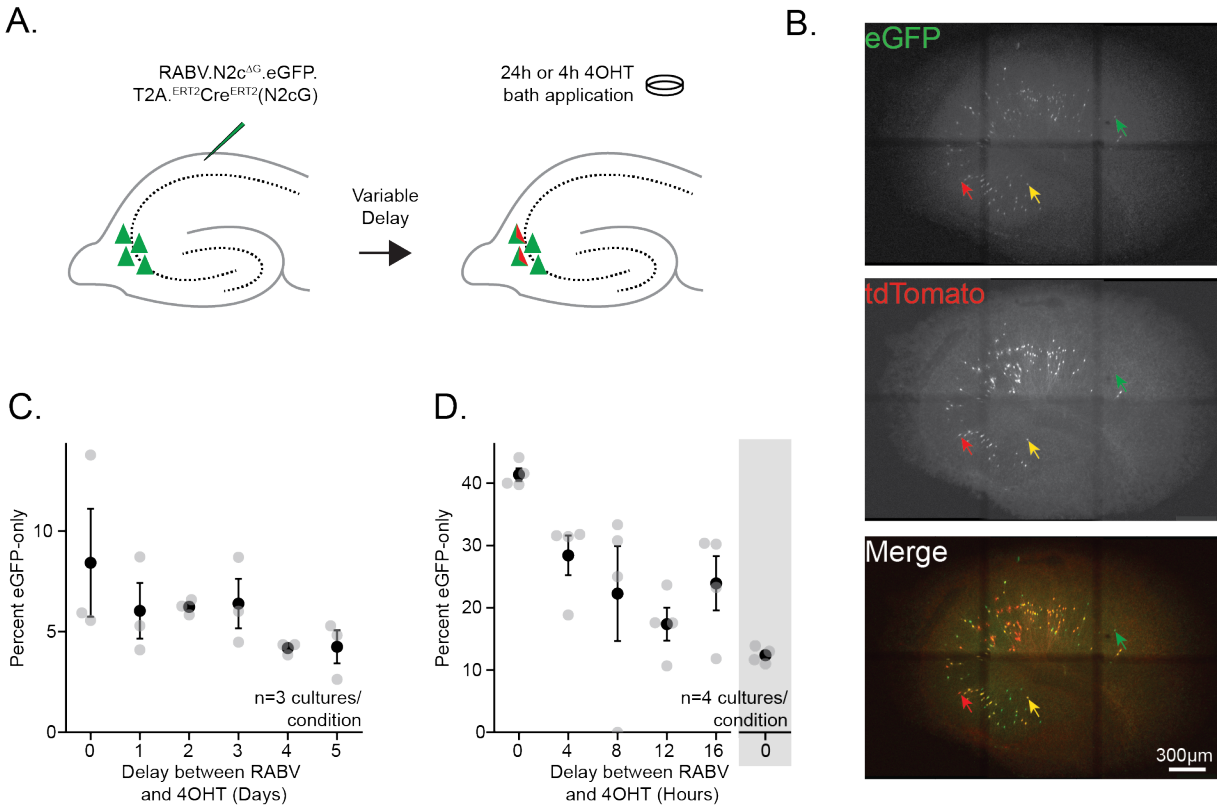

Figure 3.2 | Temporal dynamics of rabies virus Cre recombinase expression *in vitro*. **A:** Schematic of experiment. Non-transsynaptic rabies virus is injected in CA1. Cultures are treated with 4OHT after a delay period of days or hours (see x-axes of 2C, D) to induce tdTomato expression in neurons expressing inducible Cre. **B:** Example confocal images of a culture treated with 4OHT from 12-16 hours post rabies virus injection; fixed and imaged seven days after rabies virus injection. Most infected neurons co-express tdTomato. Green arrow: eGFP-only neuron. Yellow arrow: Double-labeled neuron. Red arrow: tdTomato-only neuron. **C:** Efficiency of recombination changes over five days, shown as percentage of rabies virus-infected neurons expressing only eGFP. Percent eGFP-only decreases as number of days between virus injection and 4OHT increases, indicating higher efficiency after longer rabies virus expression times. **D:** Efficacy of recombination changes over 24 hours. Percentage of rabies virus-infected neurons expressing only eGFP decreases as number of hours between virus injection and 4OHT increases. Gray box: 4OHT is applied for 24 hours immediately after rabies virus injection, rather than only for four hours. Gray dots represent individual cultures. Black dots and bars are mean ± SEM.

3.1.4. Clearance rate of 4OHT in organotypic cultures

To better estimate how long 4OHT remains active in hippocampal cultures, we repeated the previous experiments, but applied 4OHT at various intervals *prior* to rabies virus injection (Fig. 3.3A). For these experiments, the rabies virus was injected after 4OHT was removed from the culture plate, meaning that any recombination that occurs is due to 4OHT that has not yet been cleared from the tissue, even after the medium no longer contains the drug. We expected the proportion of neurons co-expressing eGFP and tdTomato to increase as the delay between 4OHT and rabies virus injection increases, because 4OHT is likely to wash out over time (Manns et al., 1993; Robertson and Katzenellenbogen, 1982). Indeed, the longer we waited to inject rabies virus, the higher the percentage of observed eGFP-only cells, suggesting that the remaining activity of 4OHT does progressively decrease over several days (Fig. 3.3B; $p<0.001$, one-way ANOVA with Tukey's HSD post-hoc test). Interestingly, even when 4OHT is removed three days before rabies virus injection, there is still enough 4OHT present to induce tdTomato expression in almost half of infected neurons (Fig. 3.3B, percentage of neurons that express only eGFP with 72-hour 4OHT interval: 54.3% ± 6.1%, n =

12 cultures). A previous experiment included a control condition, where no 4OHT was applied (Fig. 3.1E). There, I found that tdTomato expression did not colocalize with eGFP expression, showing that the inducible Cre rarely, if ever, is active in the absence of 4OHT. Therefore, the observation of tdTomato expression when rabies virus is injected after 4OHT removal is most likely not due to spurious recombination, but rather to 4OHT remaining in the tissue.

Taken together, we found that the rabies virus payload is expressed on a shorter timescale than expected, and that 4OHT remains able to induce the tdTomato snapshot with approximately 50% success three days after its removal from the cell culture medium. The slow time of 4OHT decomposition is a major consideration for these *in vitro* experiments, preventing us from drawing firm conclusions about, for example, the rate of synapse formation in hippocampal cultures.

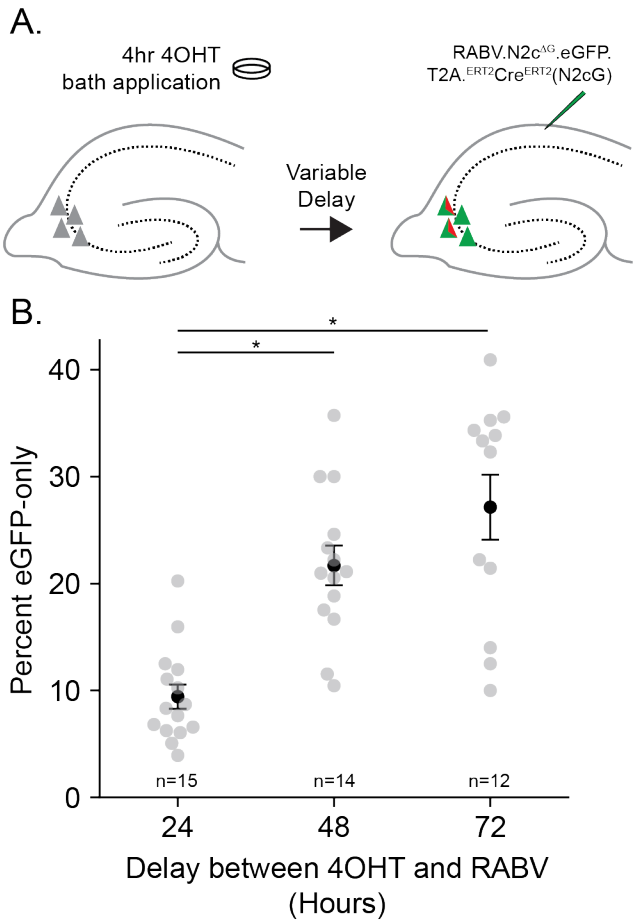

Figure 3.3 | Temporal dynamics of 4OHT *in vitro*. A: Schematic of experiment. TTT "steps" are inverted, such that 4OHT is applied before injection of non-transsynaptic rabies virus. At 4OHT application, no fluorescence is expressed (gray triangles). After rabies virus injection, infected neurons express either eGFP alone, or eGFP and tdTomato (green, red triangles). **B:** Percentage of neurons expressing only eGFP increases as delay between 4OHT removal and rabies virus injection increases. *p<0.001.

3.1.5. Two-timeframe tracing *in vitro*

In the initial *in vitro* experiment described above, I traced inputs to a dense population of starter cells, which resulted in the large majority of neurons in the culture being labeled during Timeframe 1, reflecting strong overall connectivity within these cultures (Opitz-Araya and Barria, 2011). This likely creates a ceiling effect, leaving very few cells unlabeled and able to be infected during Timeframe 2. Not only is connectivity high in hippocampal cultures, but also the rate of turnover is substantial (Opitz-Araya and Barria, 2011). For these reasons, we aimed to label fewer cells during Timeframe 1. In addition, this modification allowed us to pharmacologically manipulate connectivity and measure the effect using TTT. We implemented two approaches for reducing the number of Timeframe 1 inputs: first, by drastically lowering the number of starter cells per culture, and second, by performing TTT experiments in co-cultured hippocampal slices, in which connections form at low rates between two adjacent slices, but only one slice is injected with helper and rabies viruses.

Two-timeframe tracing using single-cell electroporation (SCE) of the helper construct was conducted according to the timeline in Figure 3.4A-D, in essentially the same manner as the experiment described in Figure 3.1A-D. Single-cell electroporation of a plasmid AAV (pAAV) helper construct into three CA1 neurons, resulting in only one to three starter cells, yielded far sparser rabies virus tracing when compared to expressing the helper construct via virus injection. Visual confirmation of starter cell expression was rarely possible, due to dim fluorescence of the membrane-bound mTurquoise2 fluorophore. As such, rabies virus was broadly injected into CA1 of the cultures two days after SCE. Approximately 5% of electroporated and injected cultures showed rabies virus tracing a few days after injection. Labeled inputs to starter cells were still dense (Fig.3.4E, G), but cell counts could be manually done, in contrast to helper virus injected cultures (Fig. 3.1). Cell counts of eGFP-only and double labeled neurons in CA1 and CA3 of four cultures showed that most labeled neurons were double labeled, and only a small fraction (CA1: 2.1%±0.9%, CA3: 4.3%±0.2%) were labeled with only eGFP (putative Timeframe 2 neurons; Fig. 3.4F). This fraction is small, in part, because of the prolonged clearance time of 4OHT in cultures. We concluded that TTT is, in principle, feasible *in vitro*, but that baseline connectivity in a single hippocampal culture is too dense to allow for experimental manipulation of Timeframe 1 and Timeframe 2 input fractions.

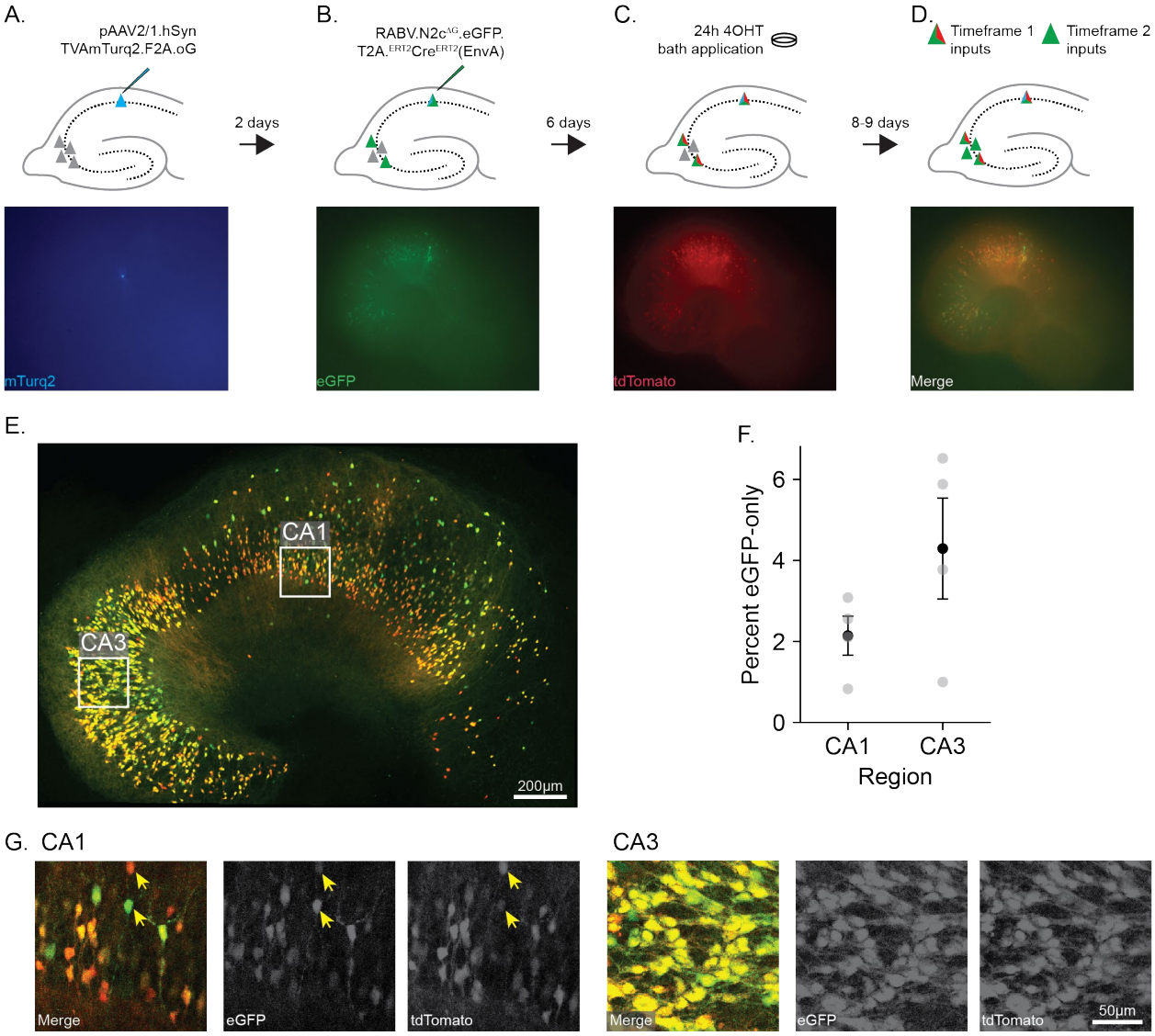

Figure 3.4 | Two-timeframe tracing *in vitro* using single-cell electroporation of helper construct. A-D, Top: Schematic of TTT tracing method in organotypic hippocampal cultures, including intervals between each step (black arrows). **A-D, Bottom**: Epifluorescence images from two example cultures; one (left) expressing mTurquoise2 three days after SCE of helper construct, and one (right three images) expressing eGFP and tdTomato after SCE, rabies virus injection, and 4OHT application, imaged three days after removal of 4OHT. These three images were made in the same imaging session. The channel(s) displayed in each column are intended to show which fluorophore(s) are associated with each step of TTT. **A:** Three neurons are electroporated in CA1, resulting in one to three starter cells. **B:** Rabies virus is injected two days after SCE, resulting in eGFP labeling of inputs to starter cell(s). **C:** 4OHT bath application induces tdTomato snapshot in rabies virus-infected neurons. **D:** After 4OHT is removed, neurons newly infected over the subsequent days express only eGFP. **E:** Example confocal image of culture in which TTT was performed using SCE expression of helper construct. Neurons express eGFP and/or tdTomato; overlap of fluorophores shown in yellow. **F:** Percentage of all labeled neurons that express only eGFP in CA1 and CA3 of four cultures treated as described in A-D. **G.** Close-ups of CA1 and CA3 regions outlined in white boxes in E. Labeling in CA3 is denser than in CA1. Yellow arrows: neurons classified as double-labeled, Timeframe 1 inputs, which show different degrees of expression in each channel.

3.1.6. Two-timeframe tracing in co-cultures

While SCE of the helper construct successfully reduced the density of tracing, the method had an exceedingly low throughput. I therefore turned to a different approach: use of organotypic co-cultures. Two organotypic hippocampal slices maintained in co-culture are able to form functional connectivity with each other (Stoppini et al., 1997). I took advantage

of this to further the TTT *in vitro* validation experiments. Using co-cultures had two key benefits over single cultures. First, it allowed us to confirm that newly-formed synapses could also be infected by rabies virus. And second, it gave the option to use helper virus injections, a method of expressing constructs with a much higher throughput than SCE, and achieve sparse expression in the culture that was not injected.

Two-timeframe tracing in co-cultured hippocampal slices was performed as described in Figure 3.5A. Cultures were arranged mirroring each other, with their dentate gyri in contact. Only one of these cultures was injected with helper virus and then rabies virus (top culture in Fig. 3.5A, B, C). All cultures were treated with 4OHT. Cultures were fixed and imaged ten days after being removed from 4OHT. I observed neurons expressing eGFP and, in a fraction of cells, co-expression of tdTomato in the non-injected culture (Fig. 3.5C, top row, bottom culture). As neurons in the non-injected cultures were not connected with the injected culture and, by extension, with starter cells when the cultures were prepared, we can be certain that these synapses had only formed during the experiment. Rabies virus is therefore able to infect newly-formed synapses.

The mean number of labeled input cells in the non-injected culture was 296 ± 138 (n=4; mean ± standard deviation; Fig. 3.5E, left). As expected, labeling in the injected cultures was much denser than in the non-injected cultures, and was unable to be quantified (Fig. 3.5C, top row).

We calculated the percentage of eGFP-only inputs in the non-injected culture, and found that 6.7% ± 4.5% of inputs were putatively labeled during Timeframe 2 in control conditions (n = 3 cultures, Fig. 3.5D, “No TTX Control”). While the majority of labeled inputs were double labeled, as in single-culture TTT experiments, the percentage of inputs appearing to belong to Timeframe 2 is approximately doubled in the co-culture TTT experiments. The fraction of “true” Timeframe 2 neurons is not possible to determine in these conditions, due to the slow clearance of 4OHT.

Achieving sparse expression and a higher proportion of Timeframe 2 neurons allowed us to implement TTT in conjunction with manipulations of neuronal activity. The goal of TTT is to identify changes in connectivity that happen alongside of, or as a result of, changes in neuronal activity which might be caused by some episode of plasticity. In the following experiment, we aimed to influence connectivity by blocking overall neuronal activity in hippocampal co-cultures. To this end, we used tetrodotoxin (TTX), a sodium channel blocker, which was added at three different concentrations to the cell culture medium. We traced inputs to the injected culture during silencing of activity with TTX (Timeframe 1) and after TTX was removed (Timeframe 2) (Fig. 3.5B). The expectation was that silencing activity would reduce labeling during Timeframe 1, but have little to no effect on labeling in Timeframe 2, which would increase the proportion of neurons labeled during Timeframe 2, relative to control cultures.

Applying TTX led to fewer neurons being traced with rabies virus in both timeframes, compared to controls (Fig. 3.5E; $p<0.01$, one-way ANOVA with Tukey’s HSD post-hoc test).

This unexpected finding could be the result of TTX inhibiting growth of axons between the two co-cultured hippocampal slices (Yamada et al., 2010). If fewer axons grow into the neighboring culture while TTX is present in Timeframe 1, there would be fewer connections to be labeled during Timeframe 2. I found the effect of TTX on overall tracing to be dose-dependent, with most cultures in the 100nM condition (the highest concentration used) showing no traced cells in the non-injected culture. These cultures are excluded from the data presented in Figure 3.5D. This drastic effect of TTX is likely due to two factors. First, rabies virus transsynaptic spread is activity dependent, which means with less neuronal activity, we can expect to see fewer traced neurons (Beier et al., 2017). Second, as neuronal activity plays a role in axonal growth in cortical cultures, silencing activity via TTX may inhibit neurite growth in these cultures as well (Uesaka et al., 2005). Reduced axonal branching may be slowing the process by which neurons in the non-injected culture form synapses with neurons in the injected culture.

The effect of TTX on the apparent fraction of neurons labeled during Timeframe 2 (expressing only eGFP) is also dose-dependent. At 10nM TTX, no difference from controls was observed ($p=1.0$, one-way ANOVA with Tukey's HSD post-hoc test). The effect of 50nM and 100nM TTX was also equivalent ($p=0.99$). High-dose TTX groups (50nM, 100nM) showed significantly higher percentages of eGFP-only cells compared to low- and no-TTX groups (10nM, no TTX control) ($p<0.05$ for all comparisons in Tukey's HSD post-hoc test).

While the expectation for this experiment was that TTX would reduce labeling in Timeframe 1, the results showed that TTX reduced tracing substantially in both timeframes. This suggests that blocking activity not only inhibits synaptic connectivity during Timeframe 1 but also impairs axonal growth and synapse formation, leading to fewer connections available for labeling during Timeframe 2. The dose-dependent effect of TTX further emphasizes the role of neuronal activity in rabies virus tracing.

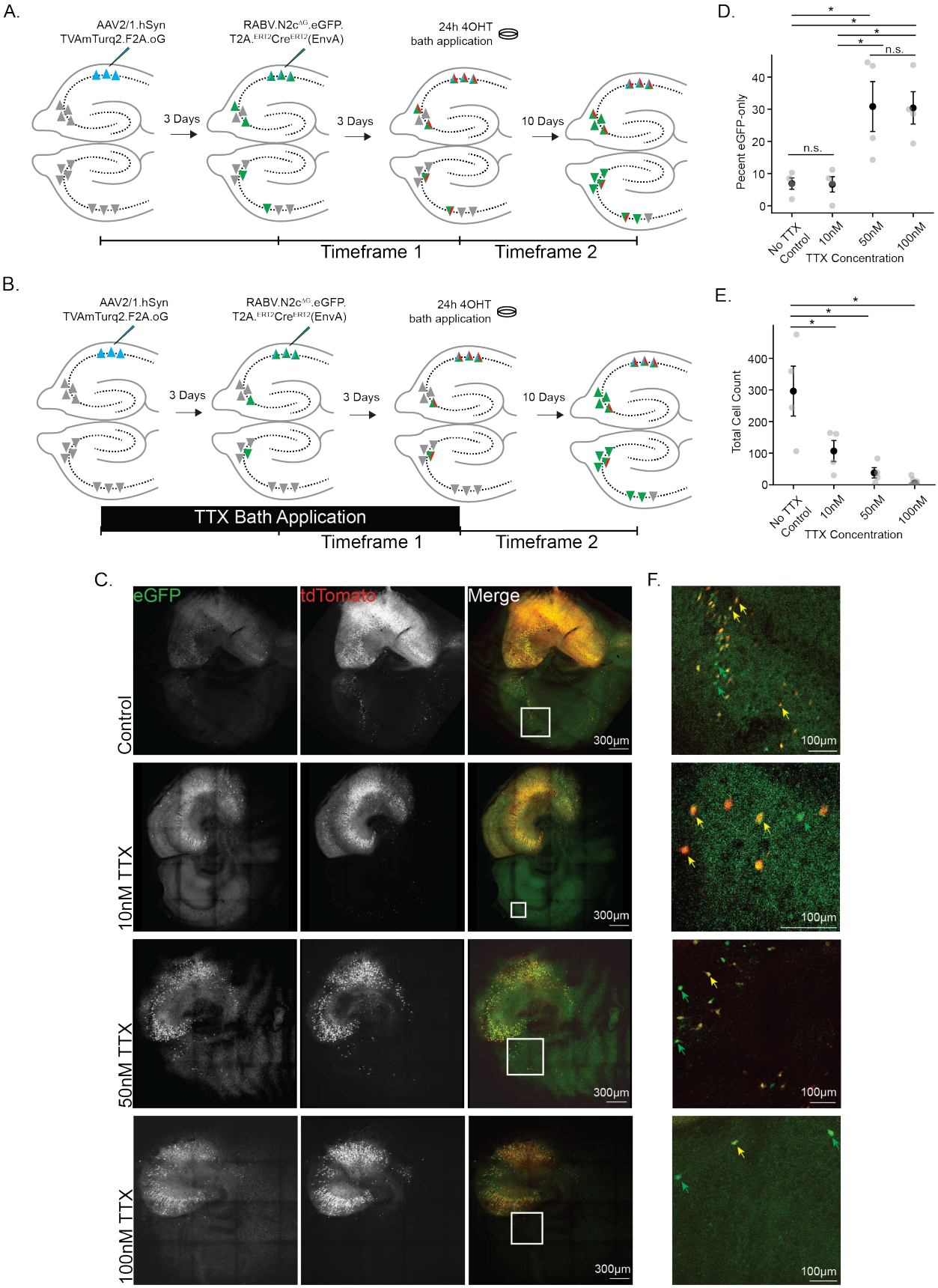

Figure 3.5 | Two-timeframe tracing in co-cultures. A: Schematic of two-timeframe tracing in co-cultures of two "mirrored" hippocampal slices. Helper virus and rabies virus are injected, three days apart, in the top ("injected") culture. Note very sparse labeling in the bottom ("non-injected") culture in comparison to the injected culture. Cultures are treated with 4OHT for 24 hours, marking the end of Timeframe 1. After 4OHT is removed, newly-infected Timeframe 2 neurons express only

eGFP. **B:** Two-timeframe tracing interleaved with TTX treatment to suppress neuronal firing in Timeframe 1. Procedure is the same as in A, except cultures were kept in medium containing TTX from the time of culture preparation until removal of 4OHT. **C:** Two-channel confocal images of example co-cultures from each condition (from top to bottom): no TTX control, 10nM TTX, 50nM TTX, 100nM TTX. White boxes: regions shown in F. **D:** Percent of eGFP-only labeled neurons in the non-injected culture for control cultures and cultures treated with TTX during Timeframe 1. *p<0.05. **E:** As in D, but for the total count of all labeled neurons. *p<0.05. **F:** Enlarged images of traced, non-injected cultures shown in C. Green arrows: eGFP-only, putative Timeframe 2 neurons. Yellow arrows: eGFP+ tdTomato+ Timeframe 1 neurons.

3.2. *In vivo* TTT validation

The experiments in organotypic cultures provided proof-of-principle evidence for TTT components, but by definition do not provide any information about how these components interact in the intact mouse brain. *In vivo*, factors like the circulatory system and the immune system influence, for example, absorption and metabolism of 4OHT. Therefore, to validate TTT *in vivo* in mice, I performed three verification experiments, prior to implementing the tool in conjunction with a standard plasticity paradigm, monocular deprivation.

3.2.1. Quantification of Timeframe 1 snapshot efficacy

Two-timeframe tracing expands the functionality of classical monosynaptic rabies virus tracing through the tdTomato snapshot, which marks the end of Timeframe 1 by labeling neurons infected up to that point in time with the tdTomato fluorophore. As such, in addition to verifying the basic functionality of the viruses being used, we needed to quantify the ability of 4OHT to label Timeframe 1 inputs *in vivo*. We expected that not all Timeframe 1 inputs would successfully express tdTomato, due to potential imperfections in the transgenic mouse line and in delivery of 4OHT. Therefore, I quantified the "false positive rate" of neurons that, in a full TTT experiment, would express only eGFP despite being already infected during Timeframe 1. This is the fraction of true Timeframe 1 neurons, which only appear to have been labeled during Timeframe 2.

To quantify the false positive rate, I used 12 tdTomato reporter mice and a non-transsynaptic rabies virus. This virus is pseudotyped with glycoprotein, rather than with EnvA, and as such does not depend on TVA receptor expression to infect neurons. Rather, this rabies virus infects neurons via axon terminals in the injection region. Crucially, non-transsynaptic rabies virus cannot further infect neurons by transsynaptic spread, because no glycoprotein is expressed. This virus was injected into multiple layers of the cortex and, in a subset of mice, hippocampus. The virus infects neurons via axon terminals in the injection region. After 10 days of expression of the genes carried by the rabies virus, I began the 4OHT treatment. Since a non-transsynaptic rabies virus is used in this experiment, no neurons become infected with rabies virus after the 4OHT treatment, and so all rabies virus-infected neurons should express tdTomato by the time of experiment readout (Fig. 3.6A, B).

To determine the optimal dose of 4OHT that would maximize efficacy of the snapshot without causing negative side effects for the mouse's health, I tried four different protocols, in a 2 x 2 design. Mice were injected either on one day (10 days after rabies virus injection) or on two subsequent days (10 and 11 days after), and received a total dose of either 100mg/kg or 200mg/kg. Confocal imaging of brain slices showed tracing in cortex and various thalamic nuclei that presumably had axons in the injection region, depending on the cortical region

that was injected with rabies virus (Fig. 3.6D). To assess the efficacy of the tdTomato snapshot for each of these four conditions, I counted how many neurons throughout the whole brain expressed only eGFP (false positives), as a percentage of the number of all labeled cells. In a perfect system, one would expect all neurons to express both fluorophores, and to find no eGFP-only neurons. Instead, I found that all conditions resulted in a fraction of rabies virus-infected neurons expressing only eGFP (Fig.3.6C, green bars). This means that not all Timeframe 1 neurons express tdTomato, despite being infected with rabies virus at the time of the snapshot. A large majority of Timeframe 1 neurons do express tdTomato, though, in all four of the conditions tested (percentage of Timeframe 1 neurons expressing tdTomato across all conditions: 84% ± 6.6%, mean ± standard deviation, n = 12 mice). There was no significant difference in the percentage of neurons expressing only eGFP across groups, though one should note that the sample size in each condition is low (Kruskal-Wallis test, p=0.38). We chose to use the 4OHT treatment with two subsequent injections, and a total dose of 200mg/kg, in all two-timeframe tracing experiments that follow, as it had the lowest false positive rate, and because no mice showed negative side effects that could be attributed to the 4OHT injection in any of the groups. The false positive rate that we expect and need to take into consideration in the TTT experiments *in vivo* is therefore 11.9% ± 4.4%. This experiment does not provide information on *why* tdTomato does not express in these false positive neurons; the following section describes an experiment that begins to address this question.

As our *in vitro* experiments showed, the tdTomato reporter mouse line shows some spurious expression of the fluorophore (Fig. 3.1E, F, bottom row of epifluorescence images). In the *in vivo* experiments, spurious tdTomato could pose a problem for interpreting results if enough Timeframe 2 neurons, which should express only eGFP, would “leak” and also express tdTomato. They would then appear to have been labeled during Timeframe 1. To test whether spurious tdTomato expression can influence results of TTT experiments, I assessed the percentage of neurons expressing only tdTomato in this *in vivo* experiment, as well. I found that, across groups, the mean percentage of tdTomato-only neurons throughout the brain ranged from 2.5% to 8.2% (Fig. 3.6C, red bars).

In this experiment, as there are no “Timeframe 2” neurons, we could not yet assess whether this amount of spurious tdTomato expression could substantially sway the measured proportion of Timeframe 2 neurons. We first needed an estimate of how many true Timeframe 2 neurons we can expect to see, which was obtained when implementing the full TTT paradigm (section 3.3).

3.2.2. Determining the cause of false positive eGFP-only neurons

There are two mechanistic explanations for why a rabies virus-infected neuron of a tdTomato reporter mouse used in TTT experiments would not express tdTomato after 4OHT application: either 4OHT failed to induce the inducible Cre recombinase, or, the tdTomato transgene was unable to undergo recombination even in the presence of Cre recombinase. I performed a proof-of-principle experiment in one mouse to confirm that both mechanistic explanations contribute to the false positive set of neurons in TTT experiments. In this

experiment, I used an AAV that expresses two proteins: eGFP, and Cre recombinase. Here, Cre does not depend on 4OHT to enter the nucleus. I injected this virus into the cortex of a tdTomato reporter mouse, waited three weeks for the ramp-up of expression of proteins, and then perfused the mouse. Like in the previous experiment, I imaged the brain and then counted all labeled neurons. In this experiment, we assume that Cre is always able to enter the nucleus of the cell. If a cell expresses only eGFP, and not tdTomato, then an imperfection in the mouse line leading to failed recombination of the transgene is likely the explanation. In this experiment, 183 neurons were fluorescently labeled (the total number of labeled neurons is substantially less than in experiments using rabies virus, because only neurons in the injection region express a viral payload). Of these neurons, 6.0% expressed only eGFP. In the previous experiment using non-transsynaptic rabies virus, approximately 12% of neurons expressed only eGFP, but that fraction encompasses false positive neurons resulting from both mechanistic explanations. That this current experiment results in 6% of neurons expressing only eGFP indicates that *both* 4OHT treatment and the transgenic mouse line contribute to the false positive eGFP-only neurons seen in TTT experiments.

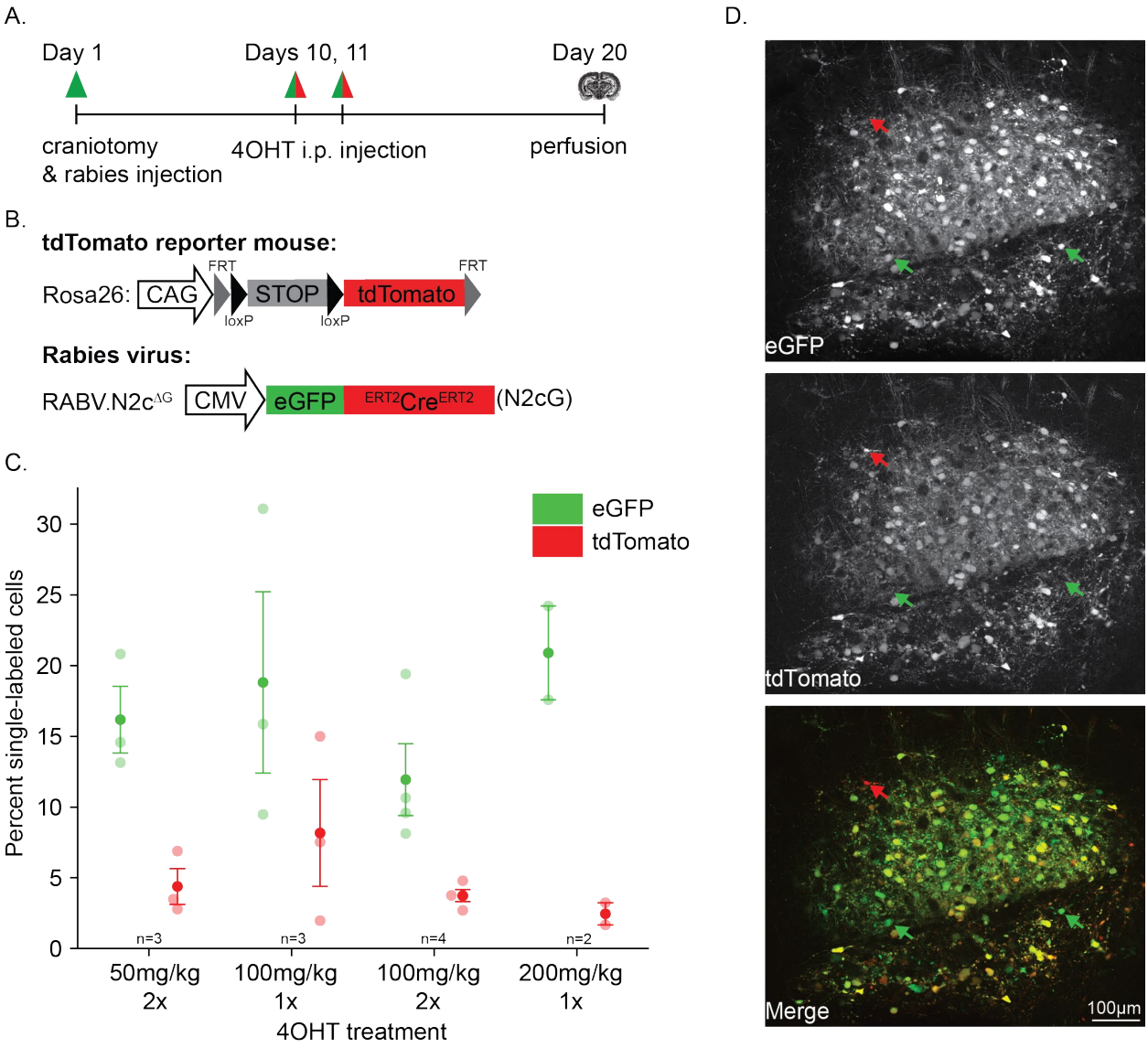

Figure 3.6 | Quantification of Timeframe 1 tdTomato snapshot efficacy. A: Timeline of experiment. Non-transsynaptic rabies virus was injected into visual or somatosensory cortex of all mice, and additionally into hippocampus in a subset. I.p. injection(s) of 4OHT took place on day 10, or on days 10 and 11, post-rabies virus injection. Mice were perfused after 20 days. **B:** Schematics describing the genetic constructs in the experiment. *Top:* The tdTomato reporter mouse line contains a transgene inserted at the Rosa26 locus, consisting of a Floxed STOP codon preceding the gene for the tdTomato fluorophore. The insert is flanked by FRT sites. *Bottom:* The non-transsynaptic rabies virus carries genes for eGFP and inducible Cre recombinase, replacing the glycoprotein gene. **C:** Quantification of single-labeled neurons (either eGFP+ or tdTomato+) as a fraction of total labeled neurons. Dots represent values for individual mice. **D:** Confocal image of rabies virus-infected neurons in the thalamus of a mouse treated with two injections of 50mg/kg 4OHT. Green arrows indicate eGFP-only neurons that fail to express tdTomato snapshot. Red arrows indicate spurious tdTomato expression in the absence of eGFP expression.

3.2.3. Long-term survival of rabies virus-infected neurons in visual cortex

In order to quantify changes in connectivity with TTT, it is crucial that starter cells support transsynaptic rabies virus tracing for the full duration of the experiment, and that rabies virus-infected neurons survive. The strain of rabies virus used in initial monosynaptic rabies virus tracing experiments was of the SAD-B19 strain, which has high cytotoxicity compared to the CVS-N2c strain used here (Reardon et al., 2016). The CVS-N2c rabies virus strain allows longer survival times for infected neurons, of approximately one month (Reardon et al., 2016). I characterized the survival times of starter cells and rabies virus-infected cells under

our conditions using chronic two-photon imaging. Both the helper virus and the rabies virus used in the TTT experiments had not been characterized with regard to how long starter cells survive after initially being infected with rabies virus, or how long input neurons infected with rabies virus generally survive. I assessed starter cell survival and rabies virus-infected cell survival in the same experiment. First, I injected helper virus and rabies virus following the protocol we established for the full TTT experiment. Then, in order to follow the fate of infected neurons over time, I performed repeated two-photon imaging of rabies virus-traced neurons in visual cortex through a cranial window over several weeks, beyond the duration of a full TTT experiment (Fig. 3.7A, D). While two-photon imaging was only possible in cortex, we assume that survival of rabies virus-infected neurons is similar throughout the brain, and so findings regarding cell survival in visual cortex are extended to the whole brain. This experiment was successfully completed in two mice.

Box 2. Sparse, but strong, helper virus expression.

For *in vivo* TTT experiments, it is crucial to have a number of starter cells that is not too high, but in which each starter cell is infected with a high titer of virus. One way to accomplish this is by using a helper virus that is dependent on an additional AAV. In contrast to *in vitro* organotypic culture experiments, the helper virus used *in vivo* is FlpO-dependent. This system is analogous to the Cre-Lox system, in that FlpO protein binds at FRT sites in RNA or DNA and can either remove or invert the construct between the FRT sites, depending on the orientation of these sites. Injecting diluted FlpO AAV in combination with a high titer of the helper virus AAV means that few cells will be infected with FlpO, but in these cells, many copies of the helper virus will be present. By making the helper virus dependent on FlpO and diluting the FlpO AAV, we were able to inject high titers of helper virus while infecting a sparse number of neurons.

I compared eGFP-expressing neurons in each subsequent pair of two-photon imaging sessions for each field of view, to assess three parameters: which neurons newly appeared, which neurons disappeared, and the total number of neurons. Doing so required reidentifying neurons across imaging sessions. If a neuron was absent in a session due to a misaligned imaging plane or other error, and then was clearly reidentified in a later imaging session, it was not counted as having disappeared. Only cells that remained absent were counted as lost.

The appearance of newly-labeled neurons is used as a qualitative proxy for starter cell survival because the mTurquoise2 fluorophore expressed by the helper virus is membrane-bound, and was not clearly visible with *in vivo* two-photon microscopy. In both mice, the number of eGFP-expressing neurons in all fields of view continued to increase for at least 20 days after rabies virus injection (Fig. 3.7B, green lines). Newly-labeled neurons expressing eGFP cannot appear if there is no surviving starter cell that the virus can transsynaptically spread from, which suggests that the starter cells in these experiments were viable for that duration. As the TTT experiment lasts only 17 days after rabies virus injection, I concluded

that the duration of starter cell survival in our paradigm allows for continued transsynaptic spread throughout both timeframes.

To estimate survival of neurons infected with rabies virus, I analyzed the loss of eGFP-expressing cells across imaging sessions (Fig. 3.7B, black lines). In all but one field of view, the fraction of neurons lost between sessions does not exceed 6% until 25 days post rabies virus injection (Fig. 3.7C). I concluded that the large majority of neurons infected with rabies virus survived for longer than the duration of the TTT experiments described in the following section.

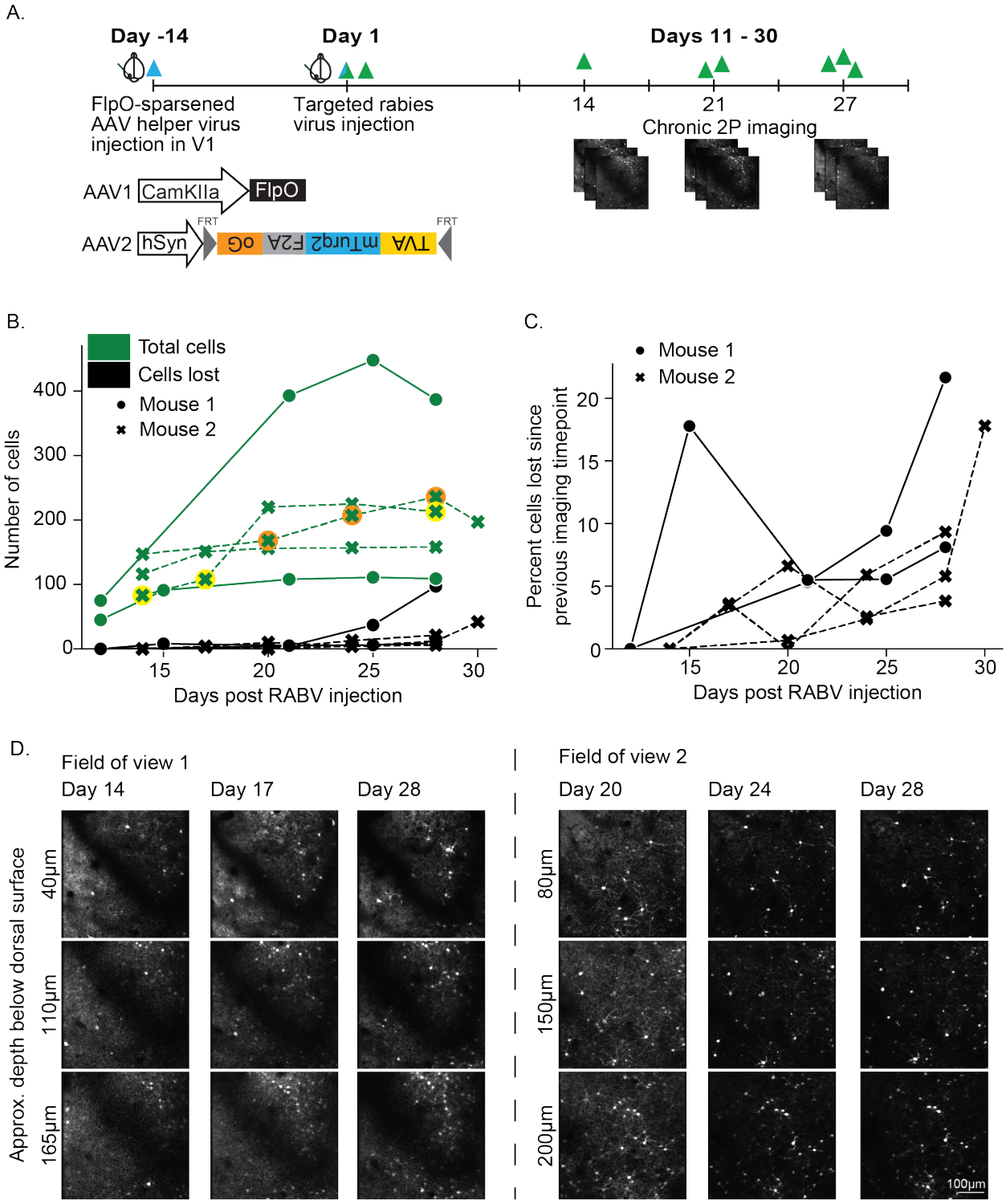

Figure 3.7 | Visualization of rabies virus expression in visual cortex over one month. A: Timeline of experiment. I injected FlpO-dependent helper virus in visual cortex of tdTomato mice, then injected EnvA-pseudotyped rabies virus 14 days later in the same region. Ramp-up of rabies virus-eGFP expression was imaged through a cranial window every three days, from 11 to up to 30 days post-rabies virus injection. **B:** *Green lines:* Number of eGFP+ cells in a given 500µm x 500µm field of view, on a given day post-rabies virus injection. *Black lines:* Number of eGFP-expressing cells lost from a field of view since the preceding imaging point. Each line is one FOV; markers represent two different mice. Yellow circles indicate data points corresponding to example images in D, Field of View 1; orange circles correspond to D, Field of View 2. **C:** eGFP+ cells lost since previous imaging point, as a fraction of total number of cells in the field of view. Each line is one field of view; markers represent two different mice. **D:** Two example fields of view from two-photon imaging in one example mouse, at three imaging planes in L1 and upper L2/3 (rows) and three sessions (columns).

3.3. Applying TTT to ocular dominance plasticity

Once we had characterized the crucial components of two-timeframe tracing, we tested whether TTT is an approach that can identify brain regions contributing to OD plasticity. OD plasticity, induced by temporary MD, has several well-known functional and structural correlates. During MD, the response distribution in bV1 shifts towards the open eye. This functional plasticity of responses is accompanied by plasticity of spines, which are the protrusions from dendrites that are used as proxies for excitatory synapses. More specifically, there is an increase in spine turnover, with a net increase in spine number that also remains elevated after the eye is reopened (Hofer et al., 2009). We set out to determine whether the percentage of eGFP-only, Timeframe 2 inputs to bV1 would be significantly altered by an episode of OD plasticity. We chose bV1 as the starter cell region and, by extension, the brain region to trace from, because of these known effects of MD. We wanted to determine whether differences would be found in the overall amount of rabies virus tracing, as well as in brain regions projecting to bV1, with a particular focus on the regions that are also known to show changes in structure or function during MD.

3.3.1. Ocular dominance shifts during monocular deprivation in adult mice

OD plasticity readily occurs in young mice during the critical period, but occurs with high variability and not in all conditions in adult mice (Sato and Stryker, 2008). To measure the effect of MD on OD and thereby confirm that OD plasticity takes place in these experimental conditions, I employed functional (IOS) imaging of the visual cortex contralateral to the deprived eye in anesthetized mice. I presented visual stimuli to one eye at a time, alternatingly covering the other eye with a plastic cup-shaped shutter. The strengths of responses to stimulation of each eye were used to calculate the ocular dominance index (ODI, see section 2.5.3), a measure of relative response strength where 0 indicates no eye preference, 1 indicates complete dominance of the contralateral eye, and -1 indicates compete dominance of the ipsilateral eye. I repeated the imaging experiment four times for each mouse: three times during Timeframe 1, to establish a baseline ODI, and once at the end of Timeframe 2 (for example responses in two imaging sessions, see Fig. 3.8B; for timeline including imaging sessions, see Fig. 3.10A, red asterisks). In all mice in these experiments, the left visual cortex was imaged. In mice undergoing MD, the right eye was sutured closed for up to eight days.

In a group of 11 adult mice (Fig. 3.8A, median age at onset of MD: P81), a period of MD lasting 7.5 ± 0.19 days led to a significant decrease in ODI (Fig. 3.8C, baseline ODI: 0.24 ± 0.027, post-MD ODI: 0.052 ± 0.026, $p<0.0001$, paired t-test). We conclude that adult OD plasticity takes place under our specific experimental conditions.

In juvenile mice, the shift in OD in V1 towards the open eye is largely mediated by suppression of closed-eye inputs; in adult mice, as used in these experiments, the OD shift is usually dominated by strengthening of open-eye inputs (Sawtell et al., 2003). I analyzed the responses to ipsilateral and contralateral stimulation to assess whether the OD shift observed here was primarily driven by either closed-eye suppression, or open-eye strengthening (Fig. 3.8D). The mean response amplitude for either eye did not change significantly during MD

(Mean amplitudes (ΔR/R) across eight blocks: baseline ipsi/open eye: (-2.78 ± 0.39)*10^{-5}, post-MD ipsi: (-2.9 ± 0.37)*10^{-5}, p=0.65, paired t-test; baseline contra/previously closed eye: (-4.33 ± 0.68)*10^{-5}, post-MD contra: (-3.51 ± 0.45)*10^{-5}, p=0.11, paired t-test). Thus, the shift in ODI appears to be mediated by both weak closed-eye suppression, and weak open-eye strengthening, rather than being dominated by changes in responses to one eye in particular.

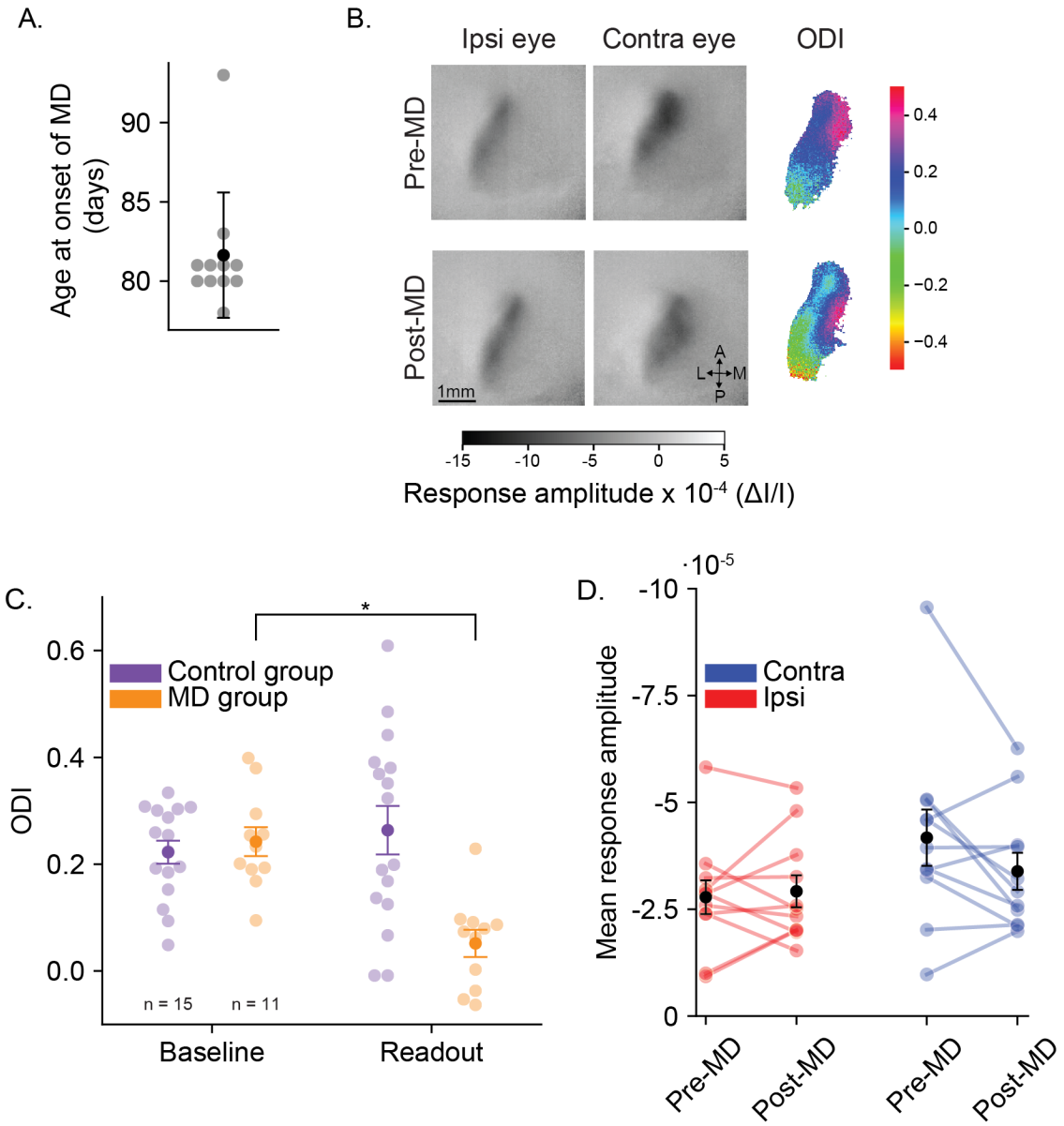

Figure 3.8 | Monocular deprivation induces ocular dominance shifts in adult mice. A: Distribution of mouse age on the day of eye suture for the 11 mice in the MD condition in the TTT experiment. Dark bar + point: mean ± standard deviation. Light points: individual mice. **B:** IOS imaging response maps from an example mouse, obtained immediately before eye suture (top), and immediately after eye opening (bottom). *Left:* mean response amplitude after stimulation of the ipsilateral (open) eye. *Center:* mean response amplitude after stimulation of the contralateral (previously closed) eye. A, L, M, P: anterior, lateral, medial, posterior directions. Lighter-colored pixels indicate weaker responses, as visible for the contralateral (previously closed) eye response after MD. *Right:* pixel-wise ODI in binocular visual cortex. **C:** ODIs for all mice in the TTT experiment. Baseline values are averaged over three imaging sessions. Readout values are obtained immediately after eye opening for MD mice, and at a comparable time point for control mice. **D:** Response amplitudes after stimulation of the ipsilateral (red) or contralateral (blue) eye, for mice in the MD group, pre-eye suture (average over three baseline sessions) and post-eye suture. Lines connect points corresponding to the same mouse. **C, D:** Dark bars + points: mean ± SEM. Light points: values for individual mice.

3.3.2. 4OHT does not influence the shift in ODI

The 4OHT injection to induce the tdTomato snapshot occurs on the days immediately preceding eye suture (Fig. 3.10A). To exclude the possibility that 4OHT influences OD plasticity, I performed a subset of experiments in which mice were treated according to the normal timeline, but the 4OHT injections were omitted. ODI after MD was not qualitatively different for mice that did or did not receive 4OHT (Supp. Fig. 1A; ODI post-MD, with 4OHT: 0.052 ± 0.026 (n = 11 mice), without 4OHT (n = 4 mice): 0.036 ± 0.039). Due to the small sample size (n = 4 control mice, 4 MD mice) with a large variance, I did not perform statistical tests. The eye-specific responses are also qualitatively similar to mice who received 4OHT (Supp. Fig. 1B). Thus, treatment with 4OHT did not seem to change the general pattern of OD plasticity observed.

To summarize, the functional imaging data collected in this experiment demonstrate that MD in adult mice induces a shift in OD towards the open eye under our experimental conditions. This shift is not driven primarily by either suppression of closed-eye inputs or by strengthening of open-eye inputs, but rather involves changes in both response amplitudes. Additionally, 4OHT treatment did not have a noticeable impact on OD plasticity, indicating that the observed effect is not merely an artifact of 4OHT application.

3.3.3. Starter cell expression lies primarily in binocular visual cortex

In *in vitro* experiments and in the *in vivo* verification experiment, visibility of helper virus expression was limited by the fact that the mTurquoise2 protein was fused to the membrane-bound TVA receptor. To improve visibility of starter cells, we designed a new AAV vector to express the helper construct that is tricistronic (see Fig. 3.9D) instead of bicistronic (see Fig. 3.7A). In the new, tricistronic virus, mTurquoise2 is not fused to the TVA receptor, because an additional 2A cleavage site was inserted into the construct between the genes for these two proteins. In addition, we included the gene for a small HA tag directly following the mTurquoise2 gene, which enables immunolabeling of starter cells. In tricistronic vectors, the first gene (the TVA receptor, in this case) is expressed most strongly, followed by the last gene (here, glycoprotein) (Liu et al., 2017). This newly-designed FlpO-dependent virus expresses *in vivo* and enables rabies virus tracing, but is still brighter at membranes than in the cytosol, making it difficult to obtain sharp images of starter cell somas. This could be because the mTurquoise2 is still targeted to the membrane via intracellular trafficking of proteins, or because cleavage of the proteins only occurs after localization to the membrane. Nonetheless, visibility of starter cells was incrementally improved with these changes made to the helper virus, which aided in proper localization of starter cell expression in V1.

I targeted helper virus injection (and, by extension, starter cell expression) to bV1 using IOS imaging to retinotopically map the visual cortex through a cranial window (Fig. 3.9A). Starter cell location, assessed by epifluorescence imaging of mTurquoise2 expression through the cranial window, was compared to the functional response mapping (Fig. 3.9B, Supp. Fig. 2). In all but one mouse, mTurquoise2 (starter cell) expression colocalizes with the lateral part of the functionally-defined primary visual cortex, indicating that a majority of starter cells in a

large majority of mice are located in bV1. One mouse was unable to be analyzed in this way due to poor mTurquoise2 visibility through the cranial window.

Visual cortex connectivity varies strongly by layer. L4 is considered the major input layer from thalamic nuclei, while L2/3 connects mostly to other cortical regions (Niell, 2015). Therefore, knowing the distribution of starter cells by cortical layer is important, because this determines where we can expect to see rabies virus-traced inputs to starter cells. To assess in which layers starter cells were present, I outlined the region expressing mTurquoise2 in confocal images of brain slices, and then registered the coordinates of the outlined region to the Allen Brain Atlas as described above. I was able to quantify this for 21 of 26 mice included in the MD tracing experiment (Fig. 3.9E). Starter cells in the remaining five mice could not be localized due to missing or poor-quality imaging data in the mTurquoise2 channel. All 21 mice had starter cells in L2/3 and L4; all but one mouse had starter cells in L5. Six mice had starter cells in L6. In addition to a post-hoc analysis of the cortical layers of starter cells, I also assessed which brain regions the starter cells were in, via registration of the images to the Allen Brain Atlas. This post-hoc registration complements the functional mapping of bV1, because the functional mapping does not rely on anatomical atlas estimates of regions. I was able to assess the anatomical location of starter cells in 21 of the 26 mice in the TTT experiment (Fig. 3.9E). In 20 of these 21 mice, starter cells were present in V1. In six of these 20 mice, starter cells were also present in the posteromedial HVA (PM). In one mouse, which is still included in further analyses, starter cells were present in somatosensory cortex (SS) and the rostrolateral HVA (RL). The anterior-posterior spread of starter cells varied by mouse. In the analyzed mice, starter cells were visible in 13.9 ± 5.2 imaging planes, corresponding to 256µm ± 84µm. The variability in the exact locations of the starter cells across mice means that pooling the results of the rabies virus tracing will result in noise introduced by this variation.

The number of starter cells directly affects how many rabies virus-infected input cells we can expect to see. To rule out starter cell number as a confounding variable that could influence differences between MD and control mice, I counted starter cells in all mice where this was possible. It was only possible to quantify the number of starter cells in 14 mice, because despite using the newly-designed tricistronic AAV, the mTurquoise2 expression is largely membrane-bound and it is therefore difficult to identify individual mTurquoise2-expressing neurons (n=7 MD mice, 7 control mice; Fig. 3.9F). There is no significant difference in number of starter cells between groups (Control: 193 ± 53; MD: 165 ± 46; p=0.7, t-test), which argues that differences between groups in number of rabies virus-infected cells or percentage of eGFP-only cells are not due to starter cell differences. Additionally, there is no correlation between the number of starter cells and the percentage of eGFP-only neurons when data is pooled across MD and control conditions (Pearson correlation coefficient = -0.34, p = 0.28).

Incidentally, in analyzing the starter cell distribution, we found that mTurquoise2-expressing neurons do not express tdTomato (Fig. 3.9C). This was unexpected, as starter cells are infected with rabies virus prior to 4OHT application, and so are therefore Timeframe 1 neurons. We use a FlpO-dependent helper virus to allow for strong expression of the helper

virus in a sparse set of neurons (Fig. 3.9D). The FlpO protein interacts not only with our helper virus (Fig. 3.9D, center), but also with the tdTomato reporter mouse's transgene insert, which is flanked by FRT sites (Fig. 3.9D, bottom). As FlpO recombines the helper AAV in starter cells, it also removes the transgene from the DNA in those cells. Therefore, tdTomato expression and mTurquoise2 expression are mutually exclusive for any given cell in a TTT experiment. Note that this does not present a problem for interpretation of results, however, because starter cells can be excluded from the set of Timeframe 2 neurons based on where mTurquoise2 expression is found. Although individual neurons expressing mTurquoise2 could not be accurately identified, diffuse mTurquoise2 expression is visible using confocal microscopy.

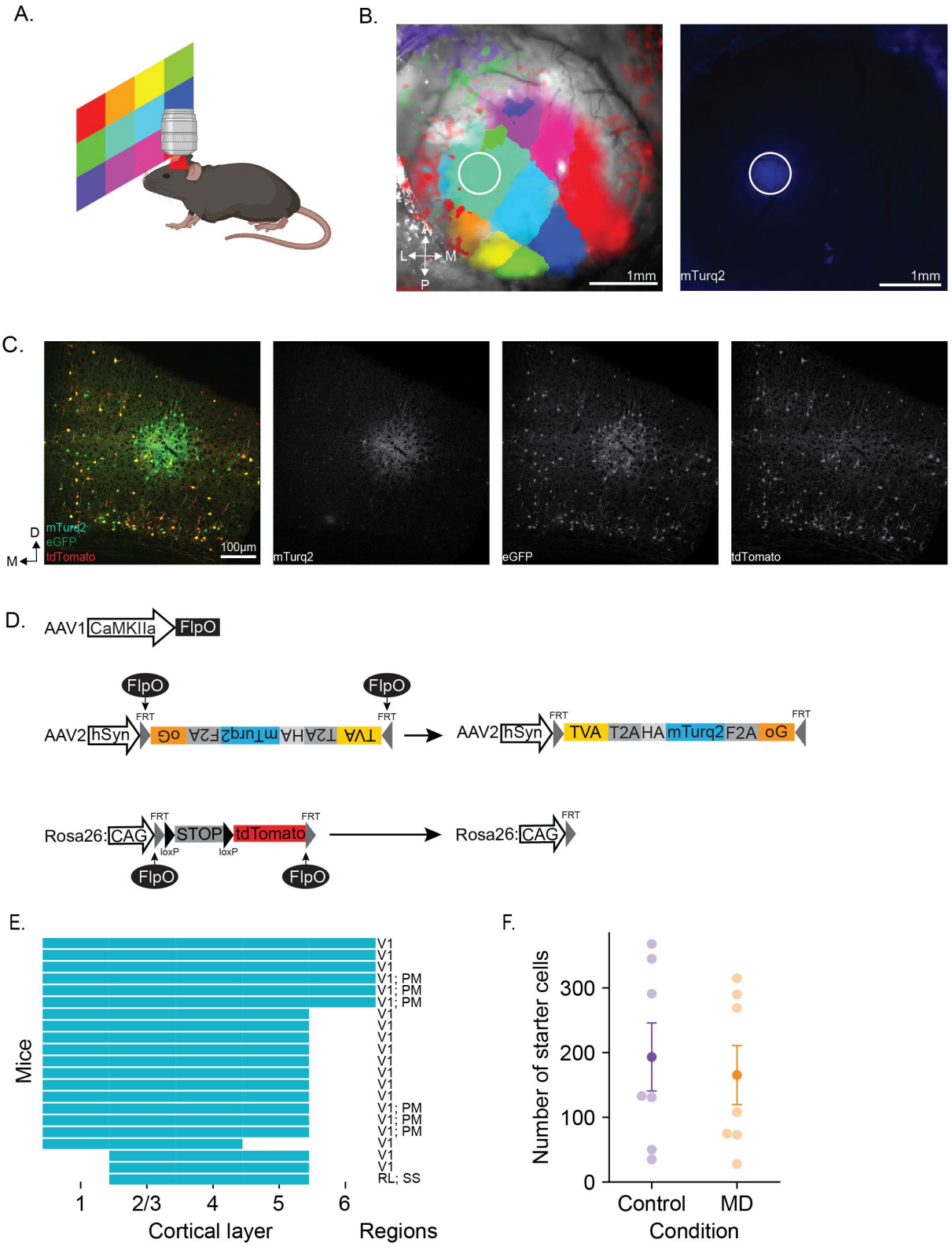

Figure 3.9 | Functional and anatomical characterization of starter cell region. A: Schematic of retinotopic mapping using IOS imaging. Drifting gratings are presented on a screen, placed in the mouse's right field of view, at the location of one of the colored squares in each trial. IOS signals are collected via an objective placed over a cranial window in the mouse's left visual cortex and detected by a sCMOS camera. **B:** mTurquoise2 label, indicating helper virus expression, is located in lateral V1, i.e. the binocular region. *Left*: brightfield image of blood vessels through cranial window of an example mouse, overlaid with response map calculated from retinotopic mapping, where the color indicates which region of the visual field in A is most strongly activating a given pixel. *Right*: epifluorescence image in mTurquoise2 channel showing expression in lateral visual cortex. White circles indicate the same location, relative to blood vessel pattern, in both images. **C:** Coronal section showing

starter cells in L2/3-L5 that express mTurquoise2, and eGFP, but not tdTomato. *Left:* merged confocal image of one plane in the starter cell region from a mouse in a TTT experiment; mTurquoise2, eGFP, and tdTomato. *Right:* single-channel confocal images of the same plane. mTurquoise2 is primarily membrane-bound, and is therefore not sharply visible in the confocal image. eGFP colocalizes with mTurquoise2 in the starter cell region, but is also present in many surrounding neurons. tdTomato does not express in neurons expressing mTurquoise2, but is present in double-labeled neurons in the surrounding region. **D:** Starter cells are unable to express the tdTomato transgene. *Top*: FlpO is expressed under the CaMKIIa promoter. *Middle, left:* FlpO interacts at FRT sites in the helper virus. *Bottom, left*: FlpO interacts at FRT sites in the tdTomato reporter mouse's transgene. *Middle, right*: FlpO inverts the helper construct. *Bottom, right:* FlpO removes the tdTomato transgene in starter cells. **E:** Cortical layers, and brain regions, containing mTurquoise2-expressing cells for 21 of the 26 mice in the TTT experiment. V1: primary visual cortex. PM: posteromedial HVA. RL: rostrolateral HVA. SS: somatosensory cortex. **F:** Number of starter cells in seven control mice (193 ± 53) and seven MD mice (165 ± 46) of the 26 mice in the TTT experiment.

3.3.4. Brain-wide analysis reveals overall increased fraction of Timeframe 2 neurons after MD

Is TTT sensitive enough to detect changes in inputs to bV1 following MD? To answer this question, I analyzed the percentage of rabies virus-infected neurons that are putatively labeled during Timeframe 2, and therefore during OD plasticity. This set of neurons expresses only eGFP, and so I report findings as the percentage of all fluorescently labeled neurons expressing only eGFP. Timeframe 1 neurons are differentiated by their expression of tdTomato. Reporting Timeframe 2 inputs as a percentage of total inputs allows us to account for differences across mice in factors that influence the overall number of labeled neurons. These factors include the number of starter cells and, in all likelihood, individual differences across mice that affect connectivity and neuronal firing. Comparing the percentages across groups (control mice and MD mice) allows us to identify the portion of eGFP-only, putative Timeframe 2 neurons that are due to OD plasticity, rather than to other factors contributing to the eGFP-only population of cells. There are two other main factors: false positive Timeframe 1 neurons (see Fig. 3.6) and baseline levels of continued labeling by the rabies virus (see Fig. 3.7).

I compared the percentage of labeled neurons expressing only eGFP throughout the brain, in control mice and MD mice, and found that a significantly higher percentage of inputs are eGFP-only in MD mice, relative to controls (Fig. 3.10B; percent eGFP-only, MD: 45.6% ± 3.15% (n = 11), control: 35.57% ± 2.10% (n = 15), p = 0.01, t-test). On a whole-brain level, MD appears to induce an increase in rabies virus tracing, which may be indicative of plasticity in the connectivity patterns in bV1.

Importantly, the mean percentages of eGFP-only neurons across both groups are higher than the 11.9% false-positive rate calculated in the non-transsynaptic rabies virus control experiment (Fig. 3.6). This argues that the population of eGFP-only neurons in TTT mice are not only a result of failed snapshots of Timeframe 1 neurons, but also from continued transsynaptic spread of the rabies virus during Timeframe 2. We can therefore assume that most eGFP-only neurons are indeed labeled during Timeframe 2.

The difference observed in percentage of putative Timeframe 2 neurons could also be the result of a systematic difference in how many neurons were labeled. For example, in a mouse with a larger number of starter cells, we would expect to see more neurons labeled during Timeframe 1, which could theoretically limit the remaining available presynaptic partners that could be infected during Timeframe 2, leading to a ceiling effect. In the current dataset,

for the mice where the number of starter cells could be determined for all mice. We would predict that mice with more labeled neurons overall would show a lower percentage of eGFP-only neurons. But the number of neurons observed may be confounded by another factor: Comparing raw numbers of traced neurons across mice does not account for differences in how complete the confocal imaging was for that mouse. Several slices needed to be excluded from analysis because of poor data quality (see Table 1 in Methods). To account for differences in the amount of imaged tissue per mouse, we calculated the number of labeled cells per square millimeter of tissue imaged, and compared these density values across groups (Fig. 3.10D). There is no significant difference in density between groups (cells per imaged mm^2: MD: 26.9 ± 5.0 (n = 11), Control: 39.1 ± 4.8 (n = 15), p = 0.09, t-test). Since the density value for the whole brain for a mouse could be affected strongly if, for example, a slice with a densely-labeled region is excluded, this density value is also accounted for on a region-by-region basis in the following analyses. Furthermore, the percentage of eGFP-only inputs is higher for MD mice as compared to controls for a given range of neuron densities (Fig. 3.10E). Taken together, we can rule out number of labeled neurons as an explanation for why MD mice have a higher percentage of neurons labeled during Timeframe 2, relative to controls.

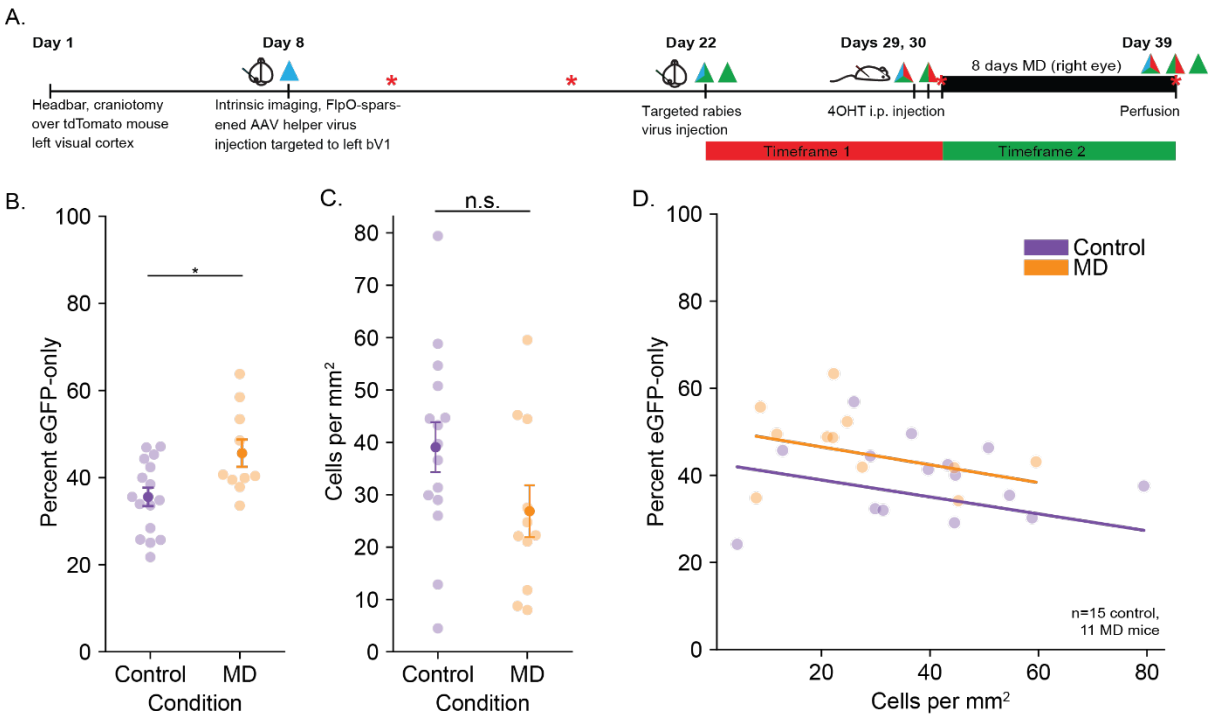

Figure 3.10 | Two-timeframe tracing shows a whole brain effect of monocular deprivation. A: Timeline of experiment interleaving two-timeframe tracing with monocular deprivation. A headbar implant and craniotomy were performed in the first surgery (Day 1). One week later, helper virus was injected to functionally-identified binocular V1 (Day 8). Rabies virus was injected on Day 22, after two weeks of helper virus ramp-up, marking the beginning of Timeframe 1, lasting seven days. The tdTomato snapshot, marking the end of Timeframe 1, was induced by two subsequent injections of 4OHT on Days 29 and 30. In half of the mice, the right eye was sutured on Day 31 to begin a 7-to-8-day episode of monocular deprivation. A control group did not undergo eye suture. Ocular dominance was measured in three IOS imaging sessions (red asterisks) preceding Timeframe 2, and one imaging session following Timeframe 2 immediately preceding the end of the experiment (Day 39). **B:** Percent of all labeled neurons that express only eGFP, throughout the brain. Mice that experienced monocular deprivation show a significantly higher percentage of green-only cells. **C:** Number of traced neurons for each mouse. **D:**

Number of traced neurons per mm^2 of brain tissue imaged for each mouse. **E:** Percent of all traced neurons expressing only eGFP, as a function of number of cells per mm^2. Lines are one-dimensional linear polynomials fit to the data points for each group.

3.3.5. Grouping of brain regions preceding region-wise analysis

Having established that the brain-wide difference in Timeframe 2 labeling is most likely attributable to the experimental manipulation (MD), rather than to inconsistencies in data acquisition or variability in number of rabies virus-infected neurons, I next set out to identify possible effects on a region-wise basis. The registration pipeline (Fig. 2.1D, E) reported more than 400 unique brain regions with rabies virus-labeled neurons in our dataset. However, there is uncertainty present in the registration process[1]. I took a conservative approach by grouping the detailed brain regions assigned to each neuron based on the Allen Atlas into 21 broader regions, which were imaged in almost all mice (Supp. Fig. 3). For each of these 21 regions, the Allen Atlas regions that I grouped together are listed in Table 2 in the Methods section. In short, I grouped all layers for a given cortical region, grouped subdivisions of sensory areas, and grouped hippocampal formation regions including subiculum and entorhinal cortex. By grouping together smaller, more detailed regions such as 'Primary visual area, layer 6a' with all other primary visual area layers, I aim to compensate for potential offsets in which neurons are assigned to which layers. Similarly, by grouping regions of somatosensory cortex that represent individual body areas, I report effects in somatosensory cortex as a whole, without the result being potentially skewed by imperfect registration to the Atlas.

For three thalamic nuclei known to project to the visual cortex (dLGN, LP, and LD), I manually defined the outline of the region in each slice containing labeling for this region. These three regions were selected because, given dense rabies virus tracing, I could identify them with high confidence. As these regions provide substantial input to visual cortex, and as dLGN in particular plays a role in visual system plasticity, it was vital to have an accurate assignment of neurons to each of these regions (Allen et al., 2016; Rose and Bonhoeffer, 2018). Unfortunately, these manually-identified regions cannot be individually corrected for the amount of tissue imaged, as these regions do not have a measurement for the number of pixels imaged. I therefore use the value for pixels imaged in "thalamus" as a whole, when calculating cells per millimeter of tissue imaged for each mouse.

The software used does not report number of pixels imaged for each hemisphere individually. For regions with bilateral labeling (V1, HVAs), I use the number of pixels imaged for the whole region, across hemispheres, to calculate the density value in each hemisphere. As the

[1] Here it must be noted that there is a caveat in analyzing primary visual cortex as a separate region from surrounding higher visual areas in this data set. During the brain clearing process, the tissue swells in a non-isometric fashion. As such, it is not always possible to register brain slices using the QUINT workflow (see Methods) precisely enough to identify these smaller cortical regions with certainty. Conclusions about these regions individually are therefore interpreted lightly.

relevant metric is whether these density values differ across mice, rather than whether density of several regions differs within a mouse, the lack of hemisphere-specific data regarding pixels imaged does not interfere with interpretation.

3.3.6. Hypothesis-driven analysis of inputs to visual cortex

One of the central questions in this thesis is whether induction of OD plasticity correlates with increased Timeframe 2 labeling in brain regions known to contribute to OD plasticity. Once we confirmed that MD induces a difference in Timeframe 2 labeling on a whole-brain scale, we analyzed three brain regions that have strong projections to bV1 and are strong candidate regions for contributing to the OD shift observed in bV1: the dLGN, local connectivity within V1, and V1 contralateral to the injection region (Antonini et al., 1999; Qin et al., 2023; Restani et al., 2009; see 4.2.2). Since MD is associated with structural plasticity in these regions, we expected to see altered Timeframe 2 labeling of inputs, as well. All mice undergoing TTT showed rabies virus-traced neurons in all of these regions (Supp. Fig. 3).

I compared the percentage of eGFP-only inputs in these most relevant regions, while controlling for differences across mice in the total number of neurons labeled. I excluded mice with fewer than 100 labeled neurons in one of these regions from analysis for that region (callosally-projecting V1: two MD mice and one control mouse removed). These are strong projections with dense labeling (Fig. 3.11A). As such, if a mouse has very few neurons labeled in a region, it is the result of missing imaging data.

Together, these three regions have significantly higher percentages of eGFP-only inputs in MD mice compared to control mice (MD: 43.6% ± 2.4% (n = 11), control: 31.2% ± 2.0% (n = 15); $p<0.01$, ANCOVA, main effect of condition; Fig. 3.11B). The percentage of eGFP-only inputs varied by region ($p < 0.01$, ANCOVA, main effect of region). The interaction between condition and brain region did not reach statistical significance ($p = 0.23$), suggesting that the directionality of the effect of MD on the fraction of eGFP-only inputs is consistent across dLGN, local V1 inputs, and callosally-projecting V1 inputs. Indeed, post-hoc testing only revealed a significant effect of MD in dLGN (MD: 39.1% ± 4.4% (n = 11), control: 22.8% ± 2.3% (n = 15); $p=0.01$, Tukey's HSD post-hoc test). I observe the same trend for V1, in particular for the callosally-projecting V1 inputs (MD: 52.3 ± 6.6% (n = 11), control: 35.2% ± 3.6% (n = 15); $p=0.07$, Tukey's HSD post-hoc test). The covariate for number of cells per millimeter of imaged tissue was significant ($p < 0.01$), indicating that the number of cells per millimeter of imaged tissue is related to the percentage of eGFP-only inputs in these key areas (Fig. 3.11C).

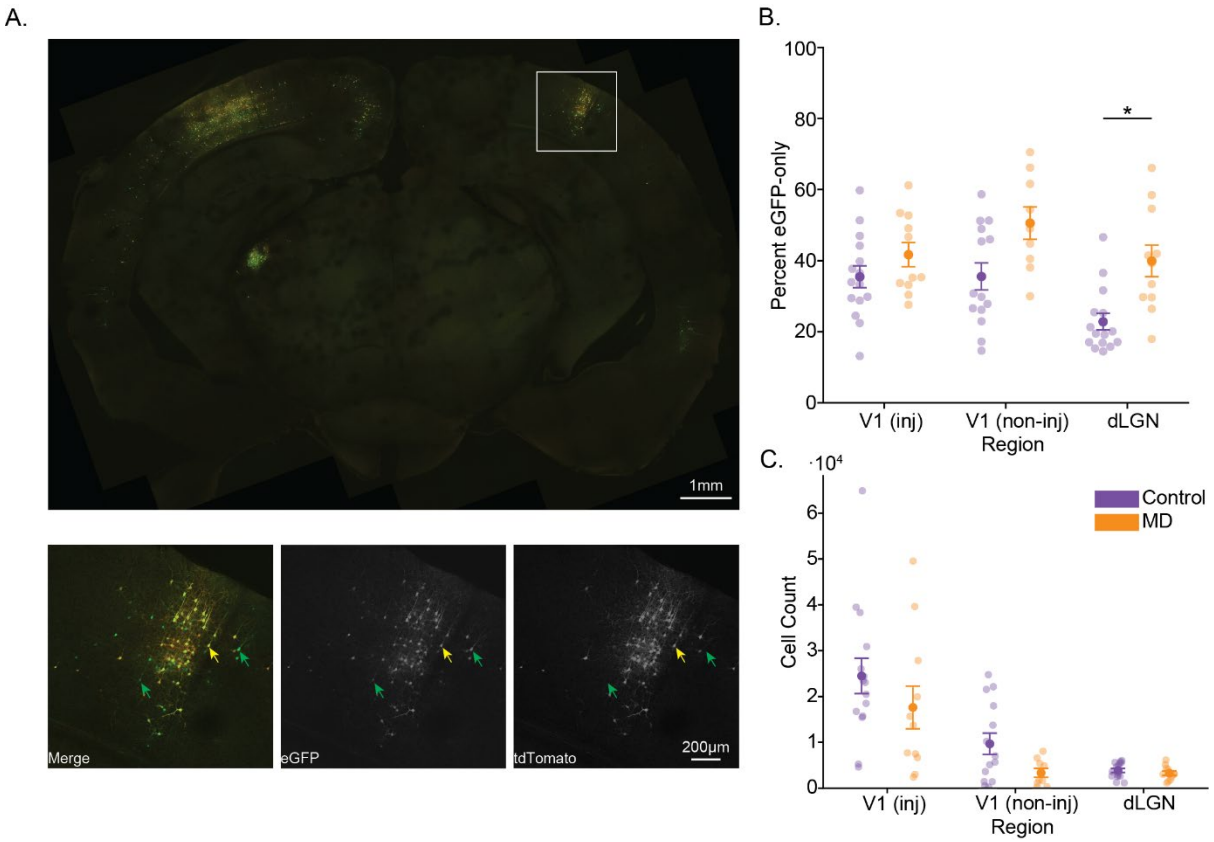

Figure 3.11 | TTT in regions known to be involved in OD plasticity. A: *Top:* Confocal image of a coronal brain slice showing rabies virus tracing in the three regions analyzed here: Primary visual cortex ipsilateral to the virus injections (V1 (inj)), primary visual cortex contralateral to the virus injections (V1 (contra-inj)), and dLGN. *Bottom:* Close-up of white square, showing inputs in the contralateral visual cortex. Green arrows: eGFP-only, putative Timeframe 2 neurons. Yellow arrows: double labeled Timeframe 1 neuron. **B:** Percent eGFP-only neurons in three feedforward regions. **C:** Total number of cells.

3.3.7. Feedback projections to visual cortex

We analyzed connectivity in regions providing feedback projections to bV1; namely, HVAs (Fig. 3.12D), the lateral posterior nucleus of the thalamus (LP), and retrosplenial cortex (RSP; Fig. 3.12E). Feedback to V1 is important for integrating spatial information, regulating visual attention, and context-dependent suppression (Briggs, 2020). The role of these regions in adult OD plasticity has recently been explored (Craddock et al., 2023), but is less clear than for feedforward projections.

I compared percentages of eGFP-only inputs, while accounting for the total number of labeled cells in each region in each mouse brain. In feedback regions, too, MD mice had a significantly higher percentage of eGFP-only inputs compared to controls (Fig. 3.12A; MD: 50.4% ± 2.0% (n = 11), control: 38.0% ± 1.9% (n = 15), $p<0.0001$, ANCOVA, main effect of condition). Post-hoc testing revealed that one of these four regions, the HVAs in the non-injected hemisphere, showed a significant effect of MD (MD: 56.0% ± 3.8%, control: 37.5% ± 4.9%, $p<0.05$, Tukey's HSD post-hoc test). There was no significant variation in the percentage of eGFP-only inputs among the different regions ($p=0.41$), and no significant interaction between condition and region ($p=0.57$). The total number of labeled cells was not a significant covariate in feedback regions (Fig. 3.12B; $p=0.53$). This indicates that the

differences observed in eGFP-only inputs between conditions and regions are not strongly driven by variations in the total number of labeled cells.

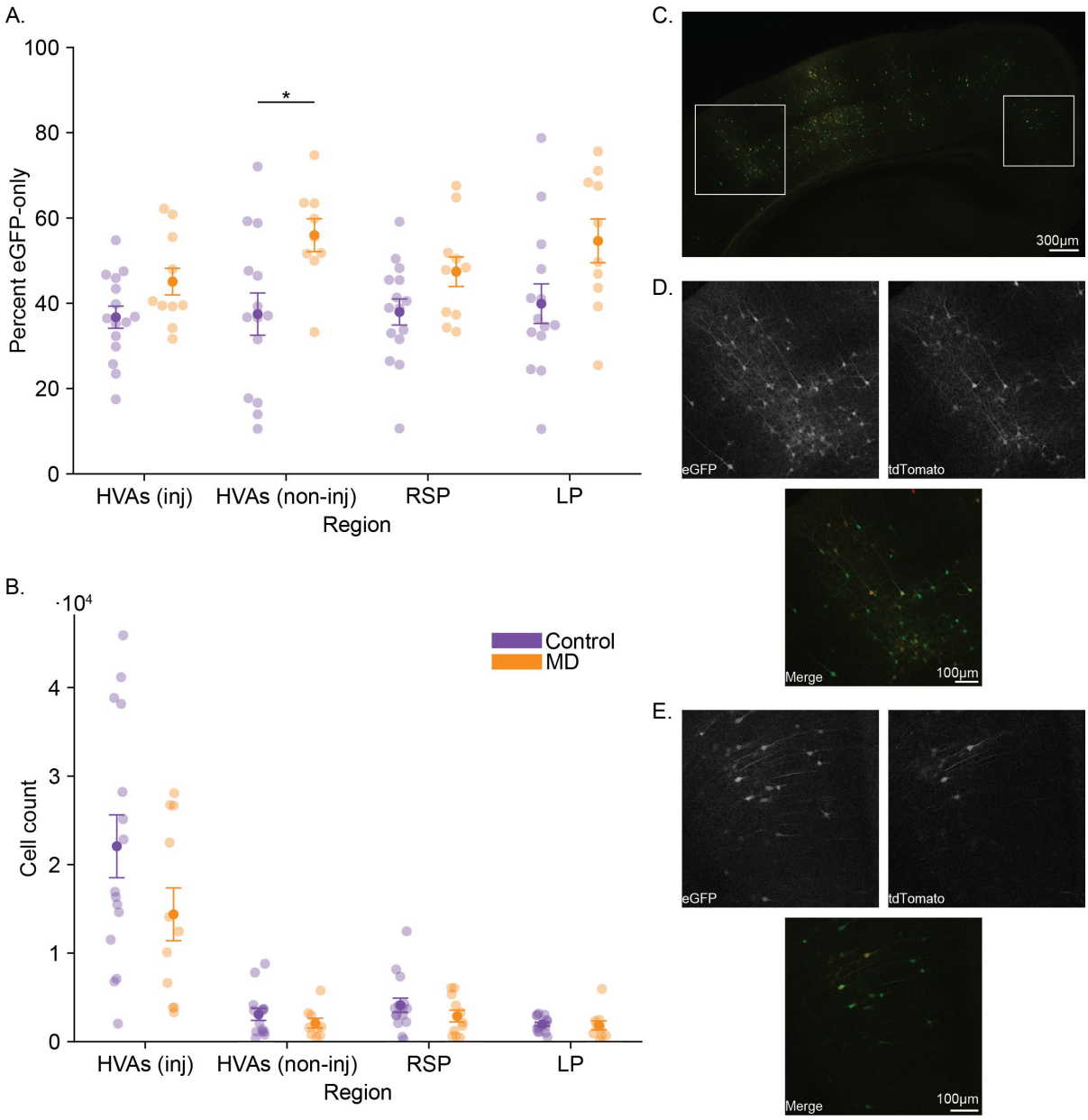

Figure 3.12 | Regions providing feedback projections to V1 have higher percentages of eGFP-only cells in MD mice. A: Percent eGFP-only neurons in four feedback regions: higher visual areas ipsilateral to the virus injection region (HVAs (inj)), higher visual areas contralateral to the virus injection region (HVAs (non-inj)), retrosplenial cortex (RSP), and lateral posterior nucleus of the thalamus (LP). **B:** As in A, but for total number of cells labeled in each region in each mouse. **C:** Confocal image of the dorsal part of a coronal brain slice, ipsilateral to the virus injection region, showing rabies virus tracing in V1, as well as HVAs and RSP. **D:** Close-up of left white square in C, showing inputs in a lateral HVA. **E:** As in D, for RSP.

One main advantage of TTT as an approach is the ability to survey the whole brain, without predefining regions where one expects to see an effect. Further analyses of the results of the TTT experiment are exploratory, rather than hypothesis-driven. While the registration pipeline reported more than 400 unique brain regions with rabies virus-labeled neurons in our dataset, there is uncertainty present in the processing pipeline. I report regions with an

average of at least 50 neurons per mouse, to partially compensate for small errors in registration. These are grouped by whether or not the region is considered part of the cortex.

3.3.8. Nonvisual cortical projections to V1

In addition to visual cortical areas described previously, we identify seven other cortical regions with substantial numbers of labeled cells: (in order of decreasing mean number of neurons) somatosensory cortex (SS), auditory cortex (AUD), hippocampal formation (including entorhinal cortex and subiculum; HPF), anterior cingulate cortex (ACC), motor cortex (MO), temporal association areas (TEa), and the insular cortex (InC; Fig. 3.13B). It is important to note that not all of these regions were imaged in all mice, and so the number of samples being compared varies. A summary of which mice are excluded from analysis of which regions can be found in Supplementary Figure 3. I compared the mean percentage of eGFP-only neurons in each of these regions, in MD mice and controls, while accounting for the number of traced cells in these regions (Fig. 3.13A). For these non-visual cortical regions, there is not a significant effect of MD on the percentage of eGFP-only neurons ($p=0.37$, ANCOVA). There is, however, a significant effect of the interaction between condition and brain region, suggesting that one or more regions may vary in how MD affects the percentage of eGFP-only cells in that region ($p < 0.001$). Post-hoc tests show that the InC has a higher percentage of eGFP-only cells in control mice, making it the only region in which we see a significant difference where control mice have a higher fraction of eGFP-only cells than MD mice ($p<0.01$, Tukey's HSD post-hoc test).

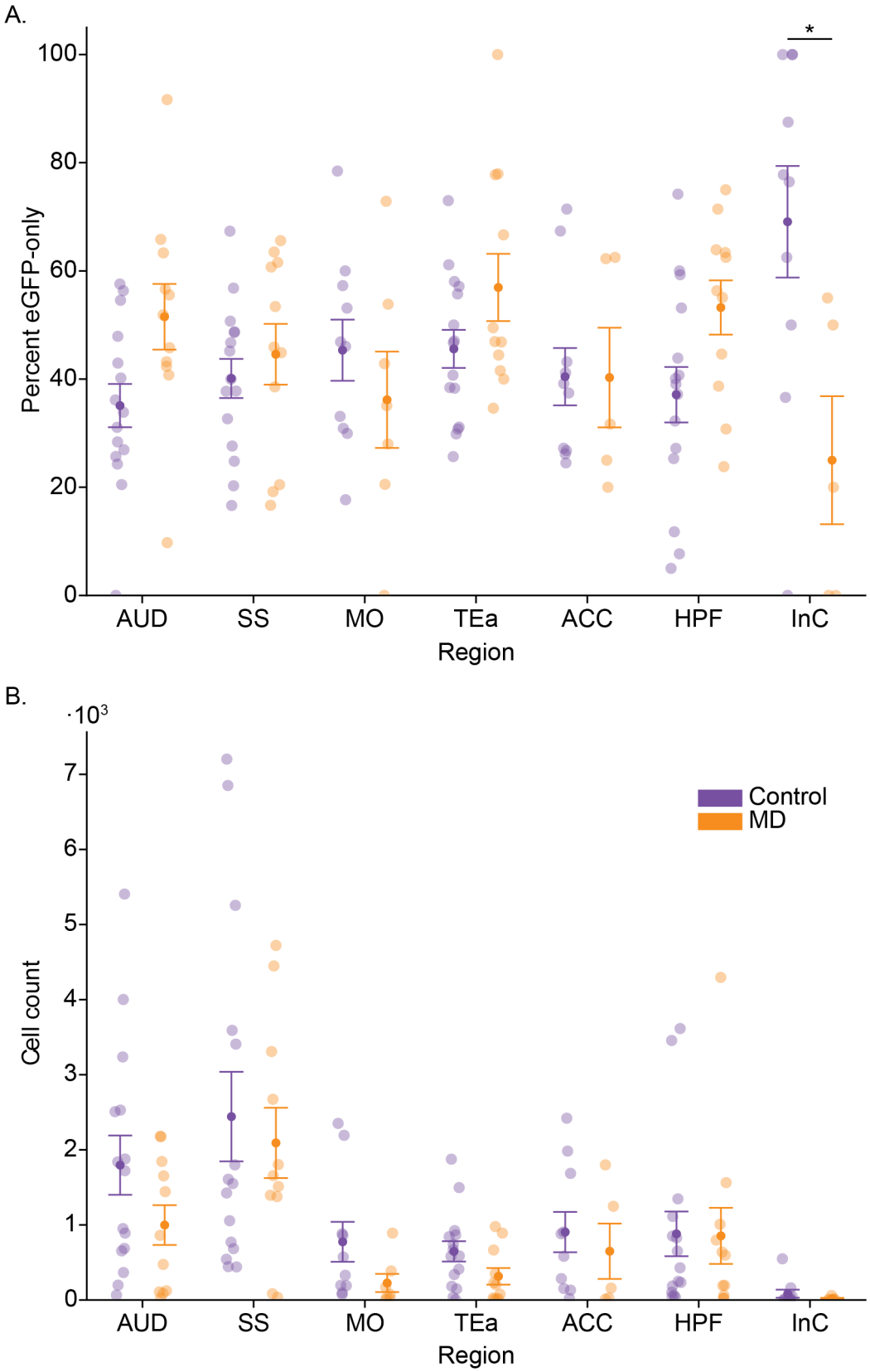

Figure 3.13 | Nonvisual cortical projections to V1. A: Percent eGFP-only neurons in eight cortical regions. **B:** Total number of cells labeled in each region. AUD: auditory cortex; SS: somatosensory cortex; MO: motor cortex; TEa: temporal association areas; ACC: anterior cingulate cortex; HPF: hippocampal formation; InC: insular cortex.

3.3.9. Subcortical projections to V1

In addition to the dLGN and LP, five subcortical regions show substantial amounts of labeling. These are, in order of decreasing mean number of neurons, the lateral dorsal nucleus of the thalamus (LD), superior colliculus (SC), hypothalamus (HY), claustrum (CLA), and amygdala (AMYG) (Fig. 3.14B). Taken together, subcortical regions do not have a higher percentage of eGFP-only inputs in MD mice as compared to controls ($p=0.71$, ANCOVA). There is a main effect of region, though, indicating that some regions may have a higher fraction of eGFP-only inputs across MD and control mice (Fig. 3.14A). Indeed, post-hoc analysis identified SC in MD mice as significantly different from five other condition-region pairs (MD:SC vs. Control:LD, $p<0.01$; MD:SC vs. Control: hypothalamus, $p<0.01$; MD:SC vs. MD:hypothalamus, $p<0.05$; MD:SC vs. MD:LD, $p<0.05$; Tukey's HSD post-hoc test). No significant difference was identified between any pair of condition-region combinations that did not contain MD:SC. In short, SC showed a pattern of Timeframe 1 versus Timeframe 2 labeling that was apparently distinctive from several of the other subcortical brain regions analyzed.

Since comparisons between regions are done using percentages of inputs found within each region, finding a significant difference driven by region and not by condition of MD or control is unexpected. It suggests that, regardless of induced experience-dependent plasticity, labeling of SC changes over the course of the experiment differentially from other regions.

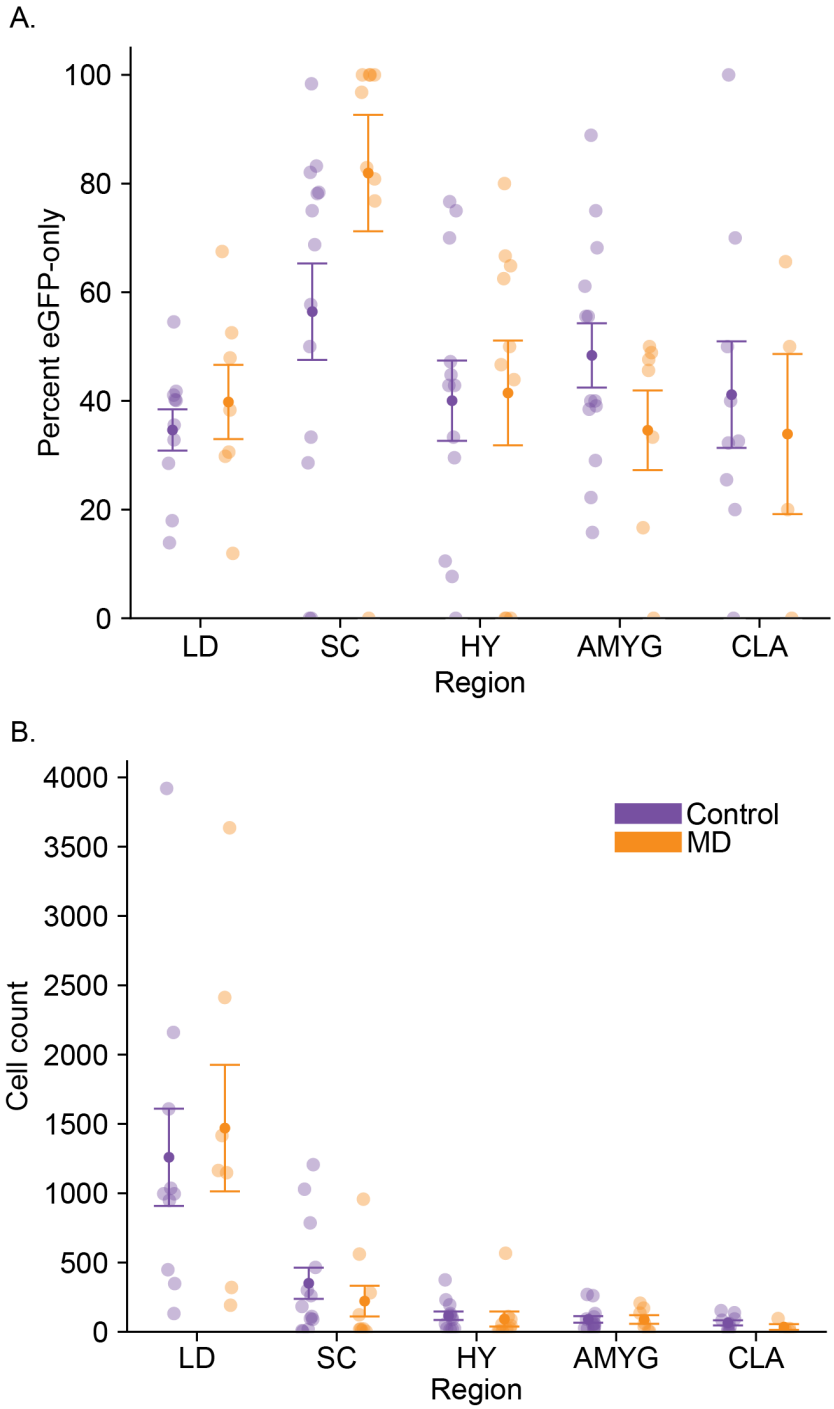

Figure 3.14 | Subcortical projections to V1. A: Percent eGFP-only neurons in four subcortical regions. **B:** Total number of cells labeled in each region in each mouse. LD: lateral dorsal nucleus of the thalamus; SC: superior colliculus; HY: hypothalamus; AMYG: amygdala; CLA: claustrum.

3.3.10. Relationship between shift magnitude and Timeframe 2 labeling

Ocular dominance plasticity induced by MD, especially in adult mice, shows a high variability with regard to effect size. Given the variability observed in the percent eGFP-only cells across MD mice, we investigated whether there was a relationship between the functional readout (change in ODI) and the readout obtained with TTT (percentage of eGFP-only inputs). To test this, I plotted the ODI at the end of the MD period (and at a comparable experimental timepoint for control mice) against the percentage of eGFP-only cells for both control and

MD mice, for the whole brain and for each group of brain regions described above. These variables do not show a correlation in any of the four groups of regions (Supp. Fig. 4, $p>0.05$ for all regions, Spearman's correlation). Possible explanations for the apparent incongruity between plasticity as measured by TTT, and that measured by IOS imaging, are presented in the Discussion (section 4.2.5).

4. Discussion

In this thesis, I developed and validated a novel approach for studying neuroplasticity in the whole mouse brain: two-timeframe monosynaptic rabies virus tracing (TTT). Conventional monosynaptic rabies virus tracing has emerged as a powerful tool for mapping inputs to starter cells (Callaway and Luo, 2015), but this method does not include a temporal component. We therefore cannot use this method alone to draw conclusions about how connectivity changes in response to experience. TTT addresses limitations in existing methods by enabling the visualization of circuit changes over time, capturing the dynamics of neuronal connectivity during learning or plasticity.

The essence of TTT lies in the conditional expression of eGFP and tdTomato. I confirmed the reliability of these expression patterns *in vitro* (Fig. 3.1). The expression of rabies virus-eGFP is not limited to starter cells, and the expression of tdTomato requires both rabies virus-inducible Cre and 4OHT application. With some limitations, I was also able to demonstrate that the likelihood of rabies virus tracing decreases as neuronal activity decreases, by applying TTX to the cell culture medium and observing a drastic drop in number of neurons labeled during this blockade of activity (Fig. 3.5).

I showed that a majority of Timeframe 1 neurons express the tdTomato snapshot, by performing a control experiment in which all neurons can be expected to express tdTomato (Fig. 3.6). The percentage of neurons that did not express tdTomato (~11.9%) is substantially lower than the percentage of eGFP-only cells in control mice in TTT experiments (~35.6%). As such, we can assume that the majority of eGFP-only neurons in TTT experiments are labeled during Timeframe 2.

Since the timeline of a TTT experiment is quite long, with regard to other monosynaptic rabies virus tracing work (see e.g., Han et al., 2024; Shao et al., 2024; Yao et al., 2023), it was vital to confirm that both starter cells and rabies virus-infected cells would, for the most part, survive until the end of the experiment. I confirmed that a majority of rabies virus-infected neurons, and a population of starter cells large enough to enable continued labeling of cells, survive for at least 25 days after rabies virus injection (Fig. 3.7). A TTT experiment ends 17 days after rabies virus injection, and so I expect that the majority of infected neurons survive for the full duration of such an experiment.

I implemented TTT in conjunction with a well-established plasticity-inducing paradigm: adult ocular dominance plasticity (Sawtell et al., 2003). OD plasticity appeared well-suited for testing TTT because much is already known about the effects of MD in adult mice. We could therefore form strong hypotheses about which brain regions would be identified as candidate contributors to OD plasticity, if TTT were to be functional. I performed two-timeframe tracing in conjunction with monocular deprivation, to test if induction of plasticity would yield differences in the output (namely, percentage of eGFP-only cells) of control mice and MD mice. Overall, I found that the percentage of eGFP-only neurons is higher in MD mice as compared to controls, and that this difference is not merely a side

effect of having more traced cells in control mice. The brain regions that are the primary contributors to the brain-wide difference in percentage of eGFP-only neurons are regions that we expected to be affected by MD: the dLGN, and the HVAs contralateral to the injection region, which are ipsilateral to the deprived eye. In addition to dLGN and contralateral HVAs, we expected to observe an effect of MD in V1 contralateral to the injection region, but this difference failed to reach statistical significance after post-hoc testing.

4.1. Characterization of Two-timeframe Tracing

Here, I have characterized properties of TTT, including the functionality of two new viral vectors and the novel 4OHT-induced snapshot labeling of Timeframe 1 neurons. In the following, I discuss the strengths and shortcomings of each component of the TTT experiment: the helper virus and starter cells, the rabies virus, the snapshot of Timeframe 1 neurons, and whole brain imaging. Additionally, I identify ways to improve the implementation of each of these components, with the aim of demonstrating TTT's potential to be widely implemented in studies of plasticity.

4.1.1. The helper construct and starter cells

The first step in a monosynaptic rabies virus tracing experiment is to express the helper construct in a set of neurons that will then become starter cells. Here, I compare the FlpO-dependent helper virus strategy used in these TTT experiments to other available options for helper construct expression. I also present the evidence in favor of our selected strategy: it allowed for rabies virus tracing of several thousand input neurons, and allowed for long-term survival of the starter cells. With the exception of a few identified disadvantages, FlpO-dependent helper virus expression worked well in the experiments presented here. The disadvantages are the difficulty faced in visualizing starter cells and the possibility of off-target expression; ways to overcome these disadvantages are discussed at the end of this section.

4.1.1.1. Approaches to supplying TVA receptor and glycoprotein to starter cells

Monosynaptic rabies virus tracing requires expression of the TVA receptor and rabies virus glycoprotein in "starter" cells (Wickersham et al., 2007b). The approach I use to do so, a single bi- or tricistronic plasmid or AAV, has the advantage of containing genes for the TVA receptor, glycoprotein, and a fluorophore in one single vector. As such, the relative titer of the TVA receptor and glycoprotein is held constant across mice and across starter cells within a mouse, and starter cells all express the complete set of genes needed for a starter cell, preventing multisynaptic tracing as a result of "hidden" glycoprotein expression in neurons not labeled with the starter cell fluorophore. Additionally, I have implemented this construct as a stand-alone virus (*in vitro*), and as a FlpO-dependent vector (*in vivo*), which allows for strong expression in a sparse set of neurons in the injection region, via titration of the FlpO AAV concentration.

Since the EnvA ligand has a very high affinity for the TVA receptor (Federspiel et al., 1994; Seidler et al., 2008), while glycoprotein is required for transsynaptic spread, a starter cell

requires more glycoprotein than TVA receptors (Lavin et al., 2020). Several other approaches have been developed to balance the expression levels of these starter cell genes, mitigating the risk of either excess TVA receptor expression, or insufficient glycoprotein. One approach is to inject two separate Cre-dependent AAVs; one for the TVA receptor and a fluorophore, and another for the glycoprotein (Watabe-Uchida et al., 2012). The approach allows independent titration of each virus, but it is possible for neurons to express Cre and only glycoprotein, if the AAV carrying TVA is absent from a subset of neurons. These neurons would not be identifiable as starter cells, because the fluorophore used to identify starter cells is only carried by the same AAV that carries the TVA receptor gene. It is therefore possible that not all rabies virus-labeled inputs are monosynaptically connected to TVA receptor-expressing starter cells. It is also possible for a neuron to only express the TVA receptor, and not glycoprotein, which would lead it to be erroneously identified as a starter cell. These issues weaken the interpretation of results obtained with this helper virus expression scheme.

Another option is to inject one Cre-dependent AAV that expresses the TVA receptor, a fluorophore, and a tetracycline transactivator (tTA), and one tTA-dependent AAV for glycoprotein and another fluorophore (Liu et al., 2017). This approach allows independent titration and ensures that glycoprotein is only expressed in TVA receptor-expressing neurons. However, the use of two fluorophores for helper virus expression limits the fluorophores available for identifying the different sets of input neurons.

4.1.1.2. The helper construct used in TTT experiments mediates strong labeling by the rabies virus

Our helper construct configuration does not allow independent titration of TVA receptor and glycoprotein expression, which means TVA expression could have been too high, or glycoprotein could have been too low. High expression levels of the TVA receptor are primarily a concern in cases where a Cre-dependent helper virus is used, and high titers lead to expression in neurons also in Cre-negative mice (Lavin et al., 2020). Expression of the helper construct in unintended neuronal subtypes can pose problems for interpretation of results. In this thesis, I focused on achieving reliable and efficient transsynaptic tracing by prioritizing glycoprotein expression. As a consequence, I put less emphasis on other aspects of monosynaptic rabies tracing, such as ensuring cell type specificity of starter cells.

In the initial *in vitro* experiments (see Fig. 3.1), the helper virus was injected undiluted and independent of any recombinase. The experiment resulted in dense labeling, such that the number of rabies virus-infected cells could not be accurately quantified. The dense tracing provides convincing evidence that the amount of glycoprotein in this configuration was more than sufficient.

In all of our *in vivo* experiments, using either the FlpO-dependent bicistronic AAV (verification experiment, Fig. 3.7) or the FlpO-dependent tricistronic AAV (TTT-MD experiments, Fig. 3.10) resulted in an overall, brain-wide number of neurons infected with rabies virus on the order of 10^4. In most monosynaptic rabies virus tracing studies using

helper viruses, the total number of inputs throughout the mouse brain is not directly reported; in several studies that perform rabies virus tracing from midbrain structures (Faget et al., 2016; Ogawa et al., 2014; Watabe-Uchida et al., 2012), and one from cortex (Sun et al., 2019), the total number of inputs is rather on the order of 10^3. While the number of inputs also depends on the number of starter cells (in TTT-MD experiments, 132 ± 121, median ± standard deviation, n = 14 mice), the relationship between number of inputs and number of starter cells is non-linear, and is best fit by a linear model applied to log-transformed data (Tran-Van-Minh et al., 2023). Therefore, the number of rabies virus-traced inputs likely relies more on the expression of glycoprotein *in* starter cells, than on the overall *number* of starter cells, for the range of starter cell numbers in the TTT-MD experiment.

One explanation for the large difference in the number of rabies virus-traced inputs in most studies, compared to the TTT experiments here, could be that the timeline of TTT includes 17 days of rabies virus tracing. Most monosynaptic tracing experiments using CVS-N2c rabies virus last only seven to ten days (see e.g., Han et al., 2024; Shao et al., 2024; Yao et al., 2023). But, because TTT allows distinguishing between neurons likely infected during the first ten days of tracing, versus in the remaining week, we can loosely compare the number of Timeframe 1 inputs to the numbers reported in other studies. Across controls and MD mice, the total number of Timeframe 1 neurons observed throughout the brain is 9,535 ± 7,696 (median ± standard deviation). We can therefore conclude that our helper virus system leads to substantial glycoprotein expression that is on par with, or exceeding, other helper construct systems.

4.1.1.3. Titer of helper virus does not interfere with neuron survival, but may lead to off-target expression

While the primary factor for neuronal survival in TTT experiments is undoubtedly the rabies virus, there is some evidence that the helper virus expression can influence cytotoxicity, as well (Lavin et al., 2020). To address the concern of cytotoxicity resulting from expression of the TVA receptor gene, I performed chronic two-photon imaging of monosynaptic rabies virus tracing in visual cortex (Fig. 3.7; discussed in 4.1.2.1). The main result here was that starter cells survive long enough to enable rabies virus tracing for at least 28 days after helper virus injection, and so we did not perform further experiments to determine the independent roles of helper virus and rabies virus in cytotoxicity. However, there is a small caveat in using the results of this experiment to confirm starter cell survival in the TTT-MD experiment: the helper virus used in the verification experiment is the bicistronic version, whereas we used a redesigned, tricistronic helper virus for the TTT-MD experiments (see section 3.3.3). It is unlikely that the change drastically reduces starter cell survival, and rabies virus is expected to cause cell death well before the AAV, but the possibility should nevertheless not be entirely dismissed.

Using our specific protocol, I observed occasional expression of mTurquoise2 outside of the injection region. However, in those cases, mTurquoise2 was never observed as

somatic expression, and often could not be conclusively distinguished from autofluorescence.

The other main concern resulting from a high titer of an AAV carrying the TVA receptor gene is expression of the recombinase-dependent helper virus in neurons lacking the recombinase (Lavin et al., 2020). I used a FlpO-expressing AAV under the CaMKII promoter, to restrict expression of the F-FLEXed helper virus to excitatory neurons, and I did not control for expression of helper virus in neurons not expressing FlpO. Therefore, I do not make the assumption that all starter cells are excitatory neurons. If one wanted to estimate the leakiness of FlpO-dependent helper virus expression, a bicistronic FlpO AAV that also expresses a fluorophore could be co-injected with the helper virus. The degree of colocalization of the FlpO-associated fluorophore and the helper virus-associated mTurquoise2 would indicate whether the helper virus expression is truly restricted to excitatory neurons. In cases where neuronal subtype of starter cells is important, a confirmation could be performed post-hoc, via immunolabeling for excitatory neuronal markers.

4.1.1.4. Suggested improvements for helper construct expression

While the current system for expressing the genes needed in starter cells proved sufficient for the TTT-MD experiments, there are additional optimizations that are conceivable for future experiments. First, the fluorophore associated with the helper virus could be switched from mTurquoise2, to a far-red or near-infrared fluorescent protein. The excitation and emission spectra of mTurquoise2 overlap substantially with those for eGFP (Mastop et al., 2017). Near-infrared fluorophores, such as miRFP2 (Babakhanova et al., 2022), would have much less overlap with the other TTT fluorophores, but may come with the disadvantage of being challenging to image with typical Ti:Sapphire lasers used for many two-photon microscopes (Kim et al., 2019).

An additional option for the starter cell expression process is *in vivo* single-cell electroporation (SCE) to transfect a sparse set of neurons with a plasmid AAV helper construct (Haas et al., 2001; Marshel et al., 2010). In my i*n vitro* experiment, SCE of no more than three neurons in CA1 resulted in labeling of hundreds of presynaptic partners (Fig. 3.4E). *In vivo,* we therefore can expect SCE to result in labeling of fewer inputs than after viral expression of helper construct, but enough inputs to still be able to draw meaningful conclusions.

There are further possibilities enabled by transfection of single cells, such as using a functional readout of a functional property like orientation selectivity or ocular dominance, and selecting which cells to transfect based on this measurement. The measurement of function could be made with whole-cell recording, which also enables transfection of the helper construct via the same pipette (Rancz et al., 2011). Alternatively, SCE could be employed, and then a genetically encoded calcium indicator (GECI) expressed in the starter cell could be used for a functional readout of starter cell properties (Wertz et al., 2015). In the context of TTT and OD plasticity, knowing the ODI of a single starter cell would have enabled us to compare the effect of MD on

connectivity with neurons that preferred the deprived eye, versus MD's effect on projections to open eye-preferring neurons. More generally, selecting starter cells by their function in TTT experiments would allow finer dissection of the circuits contributing to functional plasticity of inputs to individual neurons. The throughput of such an experiment would be low, though, due to the possibility of the only starter cell dying before the end of the experiment.

To summarize, the established helper construct expression strategy meets the requirements and priorities of the TTT experiment: long neuronal survival times, genetic control of the starter cell population, and high levels of glycoprotein in starter cells.

4.1.2. Characterization of rabies virus tracing

Rabies virus is not yet fully understood, in either its harmful wild type form or in its modified version as a tracer in neuroscience (Bastos et al., 2023; "Rabies," 2024; Rogers and Beier, 2021). We do know, though, that EnvA-pseudotyped rabies virus should only be able to enter neurons expressing the TVA receptor, it should only further infect first-order inputs to TVA-expressing neurons, and it is detrimental to cell health (Callaway and Luo, 2015). The key unknowns regarding this rabies virus primarily have to do with the factors that increase the likelihood of a given input neuron becoming infected. These factors are: a) the specificity of the rabies virus in which synapses it crosses, b) the extent to which tracing correlates with neuronal activity, and c) the extent to which tracing correlates with the strength of the connection between two neurons (Rogers and Beier, 2021). In the following, I discuss results from our experiments and from previous work in the field that contribute to our understanding of what rabies virus tracing, in the context of TTT, means.

4.1.2.1. Properties of the rabies virus used in TTT experiments

I validated what is already known about rabies viruses for the batch designed and used in my TTT experiments. I confirmed that, upon injection, the EnvA-pseudotyped rabies virus can only infect neurons expressing the TVA receptor, meaning that it is safe for use in S1 laboratory settings. In the *in vitro* SCE experiments, most cultures did not show any rabies virus-infected neurons, which was assessed by the absence of eGFP expression and attributed to unsuccessful SCE. Similarly, in a few cases *in vivo* in mice that were not included in further analysis, the injection of rabies virus was not properly targeted to the starter cell region. Consequently, these mice with no rabies virus-infected starter cells also showed no rabies virus eGFP expression. Together, these results confirmed that infection with the particular EnvA-pseudotyped rabies virus used here is also restricted to TVA receptor-expressing neurons.

The initial rabies virus variant used in monosynaptic tracing was the SAD-B19 strain, which has disadvantages such as relatively low efficiency of transsynaptic tracing and relatively poor cell survival times of less than two weeks (Osakada et al., 2011; Reardon et al., 2016). In contrast, I used the CVS-N2c strain. Introduced and characterized by Reardon and colleagues, this strain results in labeling of approximately an order of magnitude more presynaptic neurons than the SAD-B19 strain, and infected neurons

survive for approximately one month (Reardon et al., 2016). I independently validated the cell survival rate in the repeated imaging experiment, where I found that an overwhelming majority of rabies virus-infected neurons were still visible at the last *in vivo* imaging time point, up to 27 days post-rabies virus injection (Fig. 3.7). Additionally, there is evidence that that CVS-N2c strain does not infect glial cells and demonstrates strong retrograde specificity in its tracing, infecting only monosynaptically connected neurons (Reardon et al., 2016). As such, we can be confident that eGFP-expressing cells are neurons that provide monosynaptic input to starter cells.

4.1.2.2. Second and third generation rabies viruses

While the survival time of neurons infected with our rabies virus is sufficient for TTT experiments, there are other generations of modified rabies viruses that are even less toxic (Chatterjee et al., 2018; Jin et al., 2023b). These allow for neuronal survival times of several months and up to a year. The rabies virus we use is ΔG, meaning the "G" gene coding for glycoprotein is removed from the rabies virus's genome (Wickersham et al., 2007a). Rabies virus glycoprotein is known to contribute to apoptosis of rabies virus-infected cells because it triggers caspase 3 activity, and it interferes with mitochondrial respiration (Faber et al., 2002). As glycoprotein is necessary for transsynaptic spread, removing this gene prevents the rabies virus from crossing synapses. G-deleted rabies virus is considered the first generation.

The second generation is a double-deletion virus, where both the G gene and the L gene, which codes for an RNA polymerase, are deleted (Chatterjee et al., 2018; Tordo et al., 1988). The rabies virus RNA polymerase interferes with the microtubule cytoskeleton of a neuron, which enhances intracellular trafficking of rabies virus proteins, hinting at why deletion of the L gene improves survivability (Bauer et al., 2015). Neurons infected with this rabies virus survive for over four months, with little to no effect on normal functionality of the cells (Jin et al., 2024). The most recent third generation is again a single deletion, where only L is removed, which allows for cell survival rates comparable to second-generation rabies viruses with the advantage of being able to grow to higher titers during preparation, compared to rabies viruses lacking G (Jin et al., 2023b). These advances have dramatically changed the timescales of experiments that one can perform using monosynaptic rabies virus tracing. Implementation of either of these less-toxic rabies viruses would be beneficial in future TTT experiments, as one could trace a larger set of baseline input by lengthening Timeframe 1.

The second generation rabies virus was not yet widely available when the experiments presented here were in preparation. Additionally, when using first generation ΔG and third generation ΔL rabies viruses in the same laboratory, there is a risk of interaction between these two viruses leading to a functional, infectious, polysynaptic rabies virus (Hidaka et al., 2018; Jin et al., 2023c). As such, we continued to use the first generation ΔG rabies virus throughout.

4.1.2.3. Limitations of rabies virus tracing experiments

We have established that the rabies virus in TTT experiments allows for a large majority of infected neurons to survive for the duration of the experiment. There are, however, other disadvantages of using rabies virus tracing which need to be taken into consideration for TTT experiments. These drawbacks include: a) ΔG rabies virus causes an inflammatory response in the brain (Huang and Sabatini, 2020), b) rabies virus tracing undersamples some neuronal subtypes (Albisetti et al., 2017; Wall et al., 2013), and c) rabies virus labels only a subset of monosynaptically connected neurons, with estimates ranging from 5% to 40% of a cell's inputs (DeNardo et al., 2015; Rossi et al., 2019; Wertz et al., 2015).

Neuroinflammation can occur with the introduction of any substance into the brain, including more commonly-used AAVs (Chan et al., 2021). The neuroinflammatory response to rabies virus infection during monosynaptic tracing involves activation of microglia, recruitment of leukocytes not normally found in the brain (Huang and Sabatini, 2020), abnormal transcription profiles (Kim et al., 2021), and suppression of spontaneous neuronal firing, among other effects (Liu et al., 2023). In short, rabies virus can affect the normal functionality of the brain, even though most of the infected neurons survive for several weeks.

Can we still draw robust conclusions from TTT experiments, given that the rabies virus used alters signaling pathways, spontaneous firing, and other factors that are involved in plasticity? I would argue that yes, it is possible, because the control group experiences the same effects of the rabies virus, and because of previous work combining functional two-photon imaging with monosynaptic rabies virus tracing. A study from Wertz and colleagues (2015) measured orientation selectivity of V1 neurons infected with an SAD-B19 rabies virus expressing GCaMP6s, a GECI. Orientation tuning, a crucial property of V1 neurons that depends on the delicate interplay of excitatory and inhibitory inputs to a cell (Hubel and Wiesel, 1962; Troyer et al., 1998), was found to be unperturbed in neurons expressing the rabies virus-GCaMP over ten days (Wertz et al., 2015). Work by Reardon and colleagues characterizing the CVS-N2c$^{\Delta G}$ rabies virus, the strain used in the TTT experiments, also used rabies virus to introduce a GECI (GCaMP6f) into monosynaptically connected neurons. They performed awake *in vivo* imaging and report that neuronal firing is consistent with running behavior, and that the response magnitude was unaltered for at least 17 days post-rabies virus injection (Reardon et al., 2016). Coincidentally, TTT experiments also last approximately 17 days after rabies virus injection, allowing us to infer that potential adverse effects of the rabies virus infection are not consequential for interpreting results obtained with TTT in the context of the applied plasticity paradigm.

In addition to the health of infected neurons, we need to consider which neurons may categorically *not* be infected with rabies virus, despite providing monosynaptic input to starter cells. Rabies virus has been shown to undersample certain classes of inputs, such as neuromodulatory inputs (Wall et al., 2013) and nonpeptidergic, unmyelinated sensory neurons (Albisetti et al., 2017). Potential explanations for undersampling or complete

absence of rabies virus tracing for specific classes of neurons includes noncanonical synapse types, low firing rates, and absence of presynaptic receptor types involved in endocytosis of rabies virus (Ginger et al., 2013; Rogers and Beier, 2021; Tritsch and Sabatini, 2012). Since not all neuron types can be infected with rabies virus, we should not draw conclusions from negative results using this method. If a neuron type appears to be completely absent from the set of inputs to starter cells, additional verification experiments would be needed before making that conclusion.

Categorical differences between a neuron's true, full set of inputs and the rabies virus-labeled set of inputs are accompanied by further quantitative differences between these sets. Rabies virus does not infect every input to each starter cell; rather, transsynaptic spread is an ongoing process (Callaway and Luo, 2015). Longer durations of tracing and higher expression levels of glycoprotein lead to higher proportions of total inputs being labeled, but it is unlikely that any duration or amount of glycoprotein would yield a fully-traced connectome of a starter cell (Callaway and Luo, 2015). Additionally, attempts to improve tracing efficiency by overexpressing glycoprotein need to be approached cautiously, as overexpression of glycoprotein is implicated in rabies virus-induced apoptosis (Morimoto et al., 1999).

While the incompleteness of rabies virus tracing could be considered a downside to the method, the fact that some input neurons are more likely to be labeled than others could also be seen as a strength, as knowing which factors make an input more likely to be labeled lends another angle to the interpretation of the results.

4.1.2.4. Factors that may influence rabies virus transsynaptic spread

Transsynaptic spread of rabies virus from starter cells is, as discussed, incomplete and influenced by factors that are only partially understood. There are several factors that may influence the likelihood of an input cell being infected by rabies virus, such as neuronal activity and strength of the connection (Beier et al., 2017; Lerner et al., 2015; Rogers and Beier, 2021). However, there is not yet a clear consensus on the exact roles of these factors, or on whether they play a role at all (Ginger et al., 2013; Rogers and Beier, 2021). The lack of clarity may stem from varying definitions of "strength" in reference to connectivity. While some research groups clearly differentiate between the functional strength of a connection as measured by electrophysiology versus "strong" rabies virus tracing (Lerner et al., 2015; Watabe-Uchida et al., 2012), others use exclusively anatomical data to draw conclusions about the strength of a projection (Ye et al., 2022). In discussing the factors that influence rabies virus transsynaptic spread here, I distinguish between three factors that may influence tracing: the strength of structural connectivity, the strength of functional connectivity, and neuronal firing.

Structural connectivity (i.e., how many neurons connect two brain regions, and how many synapses connect two neurons) likely influences rabies virus transsynaptic spread simply by increasing the total number of synapses on starter cells that, if traced, would lead to rabies virus infection in the projecting brain region. Therefore, rabies virus can be indicative of the relative strength of structural connectivity. Although strong structural

connectivity will often correlate with strong functional connectivity, this is not necessarily the case, as in the experiments done by Lerner and colleagues (2015).

Functional connectivity, or, the degree to which afferents influence activity in the recipient brain region, seems less likely to directly correlate with the likelihood of rabies virus transsynaptic spread. Lerner and colleagues' work on projections to two populations of neurons in the substantia nigra pars compacta (SNc) directly compare structural connectivity, assessed using rabies virus tracing, and functional connectivity, determined with optogenetic stimulation and whole-cell patch clamp recordings (2015). They found that stimulation of dorsolateral striatum (DLS) inputs to SNc elicits a stronger inhibitory post-synaptic current (IPSC) compared to stimulation of dorsomedial striatal inputs. Yet this difference could not be fully explained by the number of rabies virus-traced cells in the respective regions. Further electrophysiology experiments showed that DLS inputs had a higher quantal IPSC amplitude than DMS inputs to SNc, providing a mechanistic explanation for the stronger functional connectivity found between DLS and SNc (Lerner et al., 2015). In their experiments, structural connectivity measured by monosynaptic rabies virus tracing did not predict functional connectivity, suggesting that the likelihood of rabies virus tracing is not necessarily affected by the strength of functional connectivity between two regions.

The third factor that influences rabies virus tracing is neuronal activity or firing. The influence of neuronal activity and of the functional relevance of connectivity were disentangled in work by Beier and colleagues (2017), which used monosynaptic rabies virus tracing to study cocaine-induced plasticity of inputs to ventral tegmental area (VTA) neurons. They found that mice treated with cocaine showed more labeling in the globus pallidus external segment (GP) than control mice, and that the increase in labeling was due to increased neuronal activity in this pathway. However, the functional connectivity between the GP and VTA remained limited, as measured by optogenetic stimulation of the GP and whole-cell recordings of VTA neurons in cocaine-treated and control mice (Beier et al., 2017). The authors interpreted this finding as evidence that rabies virus transsynaptic spread is more likely to occur at active synapses, regardless of the functional contribution of the input at that synapse.

Additional evidence demonstrating that rabies virus tracing is more likely at active synapses comes from the *in vitro* experiment I performed using TTX to silence organotypic co-cultures during Timeframe 1. Such pharmacological silencing resulted in reduced tracing in TTX-treated cultures, compared to control cultures (Fig. 3.5). A caveat to this interpretation is that there are at least two potential explanations: TTX may reduce tracing through reduction of firing (Rátkai et al., 2021), or TTX may reduce tracing by preventing the formation of connectivity between the two co-cultures (Uesaka et al., 2005). Since cultures are kept on medium containing TTX from the start, the blockade of activity may have prevented the growth of axons from one co-culture into the other. Indeed, TTX has been shown to reduce axonal branching in organotypic cultures (Uesaka et al., 2005; but see Wilkemeyer and Angelides, 1996, for conflicting result in organotypic

thalamocortical cultures). However, TTX leads to a substantial reduction in rabies virus tracing not only in the non-injected culture, but also in the injected culture, where there is presumably already a high degree of connectivity. Therefore, I conclude that reduction of activity is the more likely explanation for the findings in this experiment.

Monosynaptic rabies virus tracing using the CVS-N2c strain, like in TTT experiments, is a powerful tool that enables identification of long-range and local inputs to starter cells, but it is essential to consider the limitations of this tool and the factors that influence which inputs are more likely to be labeled than others. The virus is more likely to label active connections, and regions that have strong structural connectivity. Functional connectivity does not appear to play a role. When interpreting results of TTT, we therefore only use the results to infer structural connectivity and activity, without drawing conclusions about whether a brain region provides a functionally relevant input to the starter cell population, as these characteristics have been shown to not correlate (Bauer et al., 2021; Rompani et al., 2017).

4.1.3. 4OHT induction of tdTomato expression via inducible Cre

The final component of TTT is the novel component: the "snapshot" that labels Timeframe 1 neurons. I tested the reliability of 4OHT induction of tdTomato expression, because labeling of Timeframe 1 neurons is crucial for the TTT experiments. The reliability of the tdTomato snapshot determines the degree to which we can distinguish between Timeframe 1 and Timeframe 2 neurons, and so it is vital to understand the mechanisms and shortcomings of the procedure.

4.1.3.1. What conditions lead to expression of tdTomato in TTT experiments?

I first assessed what conditions are necessary for tdTomato to express in a TTT experiment, using organotypic cultures and a set of exclusion experiments (Fig. 3.1E, F). Importantly, here I distinguish between spurious tdTomato expression (see section 3.1) and "true" tdTomato expression. Spurious expression does not influence interpretation of results in TTT experiments, because it can easily be distinguished from true, brighter expression of tdTomato that colocalizes with eGFP expression.

In principle, recombination of the reporter mouse transgene, and the resultant tdTomato expression in a given neuron, depends on the following conditions: a) the tdTomato transgene, preceded by a floxed STOP codon; b) rabies virus-mediated expression of inducible Cre recombinase; and c) 4OHT induction of Cre recombinase. When either rabies virus (b) or 4OHT (c) is deliberately excluded from an *in vitro* or *in vivo* experiment, we indeed do not observe extensive tdTomato expression (Fig. 3.1E, F). Additionally, when the FlpO used in *in vivo* experiments excises the transgene in starter cells, there is no tdTomato expression (Fig. 3.9C, D), demonstrating the obvious importance of the tdTomato transgene (a) for expression of the fluorophore. When all three conditions *are* met, the tdTomato snapshot is expressed in a majority of rabies virus-infected neurons.

4.1.3.2. How effectively does the snapshot procedure induce tdTomato expression?

The three conditions discussed above are not *always* sufficient for tdTomato expression in a neuron. In a fraction of neurons in tdTomato mice where the rabies virus and 4OHT are present, tdTomato is nevertheless not expressed. We refer to the percentage of neurons where all three conditions have the potential to be met, but tdTomato is not expressed, as a false positive rate. I use the term "false positive," because a Timeframe 1 input that is missed by the snapshot appears as a false positive, eGFP-only Timeframe 2 neuron, rather than a double-labeled Timeframe 1 neuron. I quantified this false positive rate in an *in vivo* verification experiment. There, I used the non-transsynaptic rabies virus, which enters neurons at axons rather than requiring TVA receptor expression. The experiment was designed such that, at the time of readout, all eGFP-expressing neurons should contain the tdTomato transgene, and inducible Cre, which had been induced by 4OHT application. Therefore, if the system had a 100% efficacy rate, all eGFP-expressing neurons would have also expressed tdTomato.

Instead, we found that injection of 100mg/kg of 4OHT on two subsequent days led to a false positive rate of 11.9% (Fig. 3.6C). While this number is informative, there are some factors to consider when interpreting this experiment. First, I did not only inject the non-transsynaptic rabies virus in visual cortex in this experiment, but also in other cortical regions and, in several mice, in hippocampus. As a result, this pilot experiment may be more generalizable to future TTT experiments than an experiment only looking at inputs to visual cortex. However, the current result may also provide a less accurate false positive estimate for the TTT-MD experiments focusing on visual cortex, if the snapshot systematically differentially affects various brain regions or neuron types.

4.1.3.3. Why does the tdTomato snapshot not reach 100% efficacy?

There are several possible causes for a neuron to not express tdTomato, after the snapshot of Timeframe 1 neurons, in spite of the necessary conditions (see above) being met. We can reasonably assume that, if a neuron expresses enough eGFP to be detectable, there is also a non-negligible amount of Cre recombinase expressed in the neuron. Under this assumption, further causes of failed tdTomato expression can be grouped into two mechanistic explanations: either the rabies virus-inducible Cre remains unable to enter the nucleus and therefore unable to induce recombination, or the transgene is absent or otherwise unable to undergo recombination in the nucleus. In short, either the 4OHT induction of Cre fails, or the transgenic mouse line fails. If false positives can primarily be attributed to the 4OHT application being suboptimal in some way, then there is a possibility to remedy this with better 4OHT treatment, such as additional days of i.p. injections or a different application method. For example, 4OHT application can also take place through oral gavage (Whitfield et al., 2015) or in food pellets (Kiermayer et al., 2007). I therefore attempted to disentangle these two possible mechanisms of snapshot failure in a verification experiment. I injected an AAV carrying a bicistronic construct expressing eGFP and Cre recombinase into the cortex of a tdTomato mouse. Here, Cre is not dependent on 4OHT, which means that all neurons should express the eGFP gene carried by the virus, as well as the Cre-dependent tdTomato

transgene. The fact that 5% of neurons expressed only eGFP strongly suggests that 4OHT application is not the sole factor influencing the false positive rate in the non-transsynaptic rabies virus verification experiment (Fig. 3.6). Even without reliance on 4OHT induction, a portion of the neurons that contain Cre (indicated by expression of eGFP) failed to express the tdTomato transgene, which points to either the transgene or intracellular trafficking of Cre as causes of false-positive eGFP-only neurons.

One possible explanation for the finding that 5% of neurons expressing Cre did not undergo recombination involves chromatin structure. DNA in a cell is organized into tightly packed chromatin with the help of histones and other proteins (Schalch, 2017). The Rosa26 locus, where the tdTomato transgene is located, may be more or less accessible in different brain structures or different times during development, depending on chromatin organization (Vooijs et al., 2001).

There are other experiments and analyses one could perform, to gain a clearer understanding of why the tdTomato snapshot fails in some neurons. Here, I describe two possible experiments that did not fall within the scope of the current project, but which would likely provide additional insight into the tdTomato snapshot process. First, one could analyze whether the false positive rate changes based on distance to the nearest capillary or other blood vessel type. I apply 4OHT systemically by i.p. injection, and it enters the brain by crossing the blood-brain barrier. It could be possible that the concentration of 4OHT is not high enough to induce the inducible Cre protein for neurons further away from blood vessels, particularly capillaries. One could perform the same verification experiment described, using non-transsynaptic rabies virus and 4OHT treatment, and then use antibodies to label blood vessels in the perfused brain. It would then be possible to calculate the distance to the nearest capillary for each neuron. A smoothing filter could then be used to plot a rolling average of the percentage of eGFP-only false-positive neurons throughout the brain. If the local false positive rate changes as a function of distance from the nearest blood vessel, then it would be possible to use distance to assess the likelihood of a neuron failing to express the tdTomato snapshot.

The second experiment I propose would complement the eGFP-Cre AAV experiment, by distinguishing between transgene errors and intracellular trafficking errors. The aim is to quantify the proportion of false positive neurons that have Cre recombinase in the nucleus, versus those that do not have it in the nucleus, but may have Cre elsewhere in the cell. This quantification would indicate whether 4OHT failed to bind to the inducible Cre recombinase for a particular neuron. If Cre is able to enter the nucleus, it is more likely that tdTomato expression failed because of a problem with the transgene, like accessibility. An experiment to disentangle these possibilities would consist of repeating the verification experiment using non-transsynaptic rabies virus, with a few alterations. One could use a rabies virus that carries inducible Cre recombinase and eGFP that includes a nuclear localization sequence. Then, instead of imaging expression of the fluorophores *in situ*, one would perform fluorescence-activated cell sorting (FACS; Hulett et al., 1969) on dissociated cell nuclei of the brain. One would use antibodies to

fluorescently label Cre recombinase, as well as oligonucleotides to label RNA for the tdTomato fluorophore. Cells would then be sorted based on eGFP expression, presence of (presumably induced) Cre in the nucleus, and transcription of the tdTomato transgene. A comparison of the number of eGFP+, Cre+, tdTomato- cells, versus eGFP+, Cre-, tdTomato- cells would indicate the ratio of false positives due to 4OHT and inducible Cre, compared to false positives due to the transgenic mouse line.

4.1.3.4. How is the false positive rate incorporated into interpretation of results?

In the TTT-MD experiments, I report effects as the fraction of eGFP-only neurons, without adjusting the values to account for the estimated false positive rate. As many of these eGFP-only neurons were presumably infected with rabies virus during Timeframe 1, I do not refer to the full population of eGFP-only neurons as "Timeframe 2" neurons. It is possible to correct the measured fraction, to estimate the fraction of "true" Timeframe 2 neurons, though. The calculation of putative Timeframe 2 neurons is as follows:

$$TF2 = (number\ of\ double\ labeled\ cells) * \frac{100}{100 - FP}$$

where TF2 is the fraction of neurons estimated to have been infected after the injection of 4OHT, and FP is the 11.9% false positive rate. As the fraction of eGFP-only neurons increases, the difference between this fraction and the fraction of "true" Timeframe 2 neurons decreases. Instead of using this correction, I report the raw percentage of eGFP-only neurons for the following reasons.

The primary reason for not reporting the fraction of putative Timeframe 2 neurons is the risk of type 1 error, particularly with parametric statistical tests. If we correct for the false positive rate, the difference between groups as a fraction of the total value increases. We chose to minimize the risk of reporting a significant difference between groups that is not actually present in order to gain a better understanding of the robustness and strength of TTT as a new methodological approach.

Additionally, I did not quantify the false positive rate for individual brain regions, which may show variation. Potential reasons for why brain regions may vary include distance from blood vessels and therefore in how quickly 4OHT is delivered and cleared, as well as variations in chromatin structure that could influence how accessible the transgene is (Jahn et al., 2018; Vooijs et al., 2001; discussed in 4.1.3.3) Taken together, a more conservative approach is to report the true percentage of eGFP-only neurons, rather than reducing the value to an estimated, putative percentage of true Timeframe 2 neurons.

4.1.3.5. How long does 4OHT remain active, after application?

The transition between Timeframe 1 and Timeframe 2 in a TTT experiment depends critically on the time course of clearance of 4OHT from the tissue. As long as 4OHT is present at active concentrations, neurons newly traced by the rabies virus will be able to express tdTomato, meaning they will be classified as Timeframe 1 inputs. It is therefore critical to determine how long 4OHT remains active, to be able to align any plasticity paradigm to this time course.

In the *in vitro* experiments in organotypic cultures, the results indicated that 4OHT remains active in the culture long after it has been removed from the culture medium (Fig. 3.2, 3.3). The slow time course of 4OHT clearance rendered it difficult to interpret the results of TTT experiments in this system. Since I could not accurately pinpoint the effective end of Timeframe 1, defined by the time when 4OHT no longer induces tdTomato expression in newly-labeled cells, we could not use this set of experiments to draw strong conclusions about changes in connectivity in organotypic cultures.

Since we aim to implement TTT as a way to investigate brain-wide plasticity, understanding the dynamics of 4OHT *in vivo* is vital. To estimate how long 4OHT remains active in the brain, I relied on findings from work done by Valny and colleagues, in which the concentration of 4OHT in the mouse brain was measured under various conditions (2016). The authors treated young adult C57BL/6J mice with two i.p. injections of 100mg/kg 4OHT, spaced one day apart, just as in the TTT experiments presented here. They found that the concentration of 4OHT in the brain peaks eight hours after injection, and drops to ineffective levels by the third day post-injection. In the context of TTT experiments, this means that the transition between Timeframe 1 and Timeframe 2 is approximately four days long, spanning from the peak of 4OHT concentration in the brain on the first day, to when it drops below active concentration three days after the second 4OHT injection. We cannot be certain whether a neuron initially infected with rabies virus during the three days of 4OHT degradation will express tdTomato or not, which influences how we can interpret the populations of Timeframe 1 and 2 neurons. To account for the clearance time of 4OHT, one should align the plasticity-inducing paradigm such that the hypothesized peak of formation of new connections in the starter cell region takes place approximately three days after the second 4OHT injection, as described for the TTT-MD experiments below.

4.1.3.6. Does 4OHT influence OD plasticity?

In the TTT-MD experiments, the onset of MD follows just one day after the second and final 4OHT injection. Based on previous work, we expect 4OHT to be below active concentration in the brain by the third day after injection (Valny et al., 2016), which means that 4OHT is still active in the brain for the first three days of monocular deprivation. While there have been no reports of 4OHT interacting directly with plasticity mechanisms, I nevertheless confirmed that 4OHT did not alter OD plasticity. To do so, I performed a control experiment where mice were treated as in TTT-MD experiments, but were not injected with 4OHT. I compared the ODI shift between the two groups, and found no qualitative differences in either the magnitude of the ODI shift or in the relative contributions of closed-eye suppression and open-eye strengthening (Supp. Fig. 1). Given the small sample size of this experiment, statistical tests were not performed. Note that the sample size for this control experiment was much smaller than for the TTT-MD experiment, and that adult OD plasticity shows relatively high variability across individuals (Sato and Stryker, 2008). Further investigation would therefore be necessary to concretely determine whether 4OHT treatment interacts in a more subtle way with the changes in the brain induced by MD.

4.1.3.7. What are the negative effects of 4OHT?

Treatment with tamoxifen and its metabolites, like 4OHT, has been observed to have negative effects on the health and survival of mice, especially with treatment that is more prolonged than that used in the TTT experiments described here (Halpage et al., 2024; Huh et al., 2012; Rossi et al., 2023). In designing the TTT experiments, we referred to previous work in other labs to try to minimize these negative effects. For example, we use 4OHT instead of tamoxifen because a substantially lower concentration is needed to achieve a given efficacy (Valny et al., 2016). I also ensured that as much EtOH as possible had evaporated from the solution during preparation of 4OHT for injection.

The interaction of 4OHT and medetomidine has very recently been shown to cause high mortality in male mice (Rashbrook et al., 2023). In the TTT-MD experiments, which took place prior to the publication from Rashbrook and colleagues, mice in the MD group were anesthetized with a mixture that included medetomidine (see section 2.3.3) just one day after 4OHT treatment (Fig.3.10A). Indeed, in line with Rashbrook and colleagues, male mice in the TTT-MD experiments that were in the MD group, unexpectedly at the time, showed high rates of mortality following eye suture surgery. I therefore included only female mice in the MD group, once this problem in males became clear.

Given the possibility that 4OHT treatment and FMM anesthesia are not compatible, it makes sense to consider a different method of anesthetizing mice in future experiments. Additionally, it may be possible to lower the dose of 4OHT for future TTT experiments. In the verification experiment I performed to establish the false positive rate, I treated mice with one of four 4OHT injection schemes and found no significant difference in the percentage of neurons that failed to express tdTomato (Fig. 3.6). One could consider repeating this experiment with a larger sample size, and 4OHT injection schemes with total dosages below 100mg/kg, to estimate a false positive rate for a lower dose of 4OHT. The goal would be to identify the minimum dose that does not significantly reduce the fraction of rabies virus-infected neurons that undergo recombination.

We developed TTT as a generalized methodological approach, to be able to study plasticity in a wide range of paradigms. Many (even most) of these potential applications of TTT do not require a surgery to induce plasticity after the tdTomato snapshot. As such, this particular challenge of 4OHT treatment immediately preceding anesthesia and surgery is unlikely to be present in most other potential applications of TTT.

There are several advantages of using inducible Cre recombinase and 4OHT, which should be taken into consideration. The main benefit I find in using inducible Cre is that this treatment is not a surgical intervention. The i.p. injections of 4OHT appeared to carry a relatively low burden for the mice in the absence of anesthesia, as assessed by observing mouse behavior in the hours following injection, and by noting that there was no notable weight loss in the days following injection. In addition to benefits for mouse welfare, the absence of a surgical intervention at the transition between Timeframe 1 and Timeframe 2 is also beneficial from the experimenter's perspective, as mice can more rapidly transition into a learning paradigm this way. To conclude, the drawbacks of 4OHT

application can be mitigated (i.e., by considering a lower dose and a different protocol for anesthesia) without loss of the several advantages of the method.

4.2. Investigating Ocular Dominance Plasticity using TTT

While it is generally accepted that OD plasticity in mice is not limited to an early critical period (Gordon and Stryker, 1996), the effects of MD in adult mice show high variability across individuals (Sato and Stryker, 2008), across environmental conditions (Balog et al., 2019; Greifzu et al., 2016; Kalogeraki et al., 2014), and across strains of mice (Heimel et al., 2008). Therefore, in order to contextualize the results of the TTT experiments, it was important to confirm that an OD shift did in fact take place in the mice that had undergone MD. I used IOS imaging to measure the amplitudes of responses to contralateral and ipsilateral stimulation in three baseline imaging sessions, and one readout session immediately after MD, for each mouse. The ODI decreased significantly during MD. While juvenile OD plasticity is generally driven by a strong decrease in deprived-eye responsiveness (Frenkel and Bear, 2004), and adult OD plasticity by an increase in open-eye responsiveness (Sawtell et al., 2003), the OD shift in my experiments appeared to be driven by changes in responsiveness to both eyes. Previous work has demonstrated that environmental enrichment can preserve juvenile-like OD plasticity, such that MD induces deprived-eye depression of responses (Greifzu et al., 2016; Kalogeraki et al., 2017). As these mice were housed with enrichment such as a running wheel in their cages, it was not entirely unexpected that the ODI shift observed here was mediated in part by deprived-eye depression.

4.2.1. Overall anatomical results of TTT are largely consistent with previous work on V1 connectivity

In the TTT-MD experiments, I labeled inputs to the binocular region of primary visual cortex (bV1) using rabies virus tracing. The analysis pipeline used for registration of these labeled neurons to brain regions of the Allen Brain Atlas revealed more than 400 specific brain regions containing rabies virus-traced cells. Before interpreting the effects of MD and the results of two-timeframe rabies virus tracing, I evaluated whether the basic patterns of connectivity revealed by monosynaptic rabies virus tracing are consistent with the literature on brain-wide input to visual cortex.

Overall, my data align closely with previous studies on brain-wide inputs to mouse visual cortex (Falkner et al., 2016; Oh et al., 2014). I drew more direct comparisons to results from a more recent publication, which analyzed inputs to visual cortex using rabies virus tracing (Yao et al., 2023). In this work, the authors compare the rabies virus-traced inputs projecting to various populations of spatially and genetically defined starter cells, in V1 and various HVAs. The helper virus in the TTT-MD experiments was targeted to excitatory neurons. I therefore specifically compared the results of experiments tracing from excitatory neurons reported by Yao et al. to the results presented in this thesis.

The regions identified as providing substantial input to V1 in the TTT-MD experiments align with the regions identified by Yao et al. (2023). Namely, in our work and theirs, V1

ipsilateral to the injection contains the highest fraction of input neurons, regardless of if starter cells are also in V1 or rather in HVAs. Their work also found all but one of the other broader brain regions identified in my analysis as providing input to excitatory neurons in visual cortex (Table 2; Yao et al., 2023). The inferior colliculus (IC) was only identified in four out of 26 TTT-MD mice as containing rabies virus-infected neurons (median = 3 neurons, maximum = 6 neurons). As the IC borders the SC, it is likely that a small error in registration explains this finding, rather than a discrepancy between my results and those of Yao et. al (2023).

Importantly, both Yao et al. and our results show a small amount of labeling in the superior colliculus (SC), which has previously not been reported to project monosynaptically to V1. Yao et al. report a potential monosynaptic connection between SC and the postrhinal higher visual area (POR), with very sparse SC labeling observed in 10% of the approximately 300 mice in their study. The same was true in cases where starter cells were excitatory neurons and located in V1 (Yao et al., 2023). Conclusive evidence of a monosynaptic projection from SC to V1 is absent from the literature, with the exception of their results, which rely on rabies virus tracing. Further experiments would be needed to explain why rabies virus appears to identify SC as an input region to V1, while conventional tracing methods do not seem to reveal this projection.

Comparing the distribution of rabies virus traced neurons to previous work has highlighted one of the disadvantages of the relatively long experimental timeline of TTT – rabies virus may sparsely spread to brain regions that may not be monosynaptically connected to starter cells. Despite this downside, I have identified only one brain region (SC) that is consistently labeled in spite of having very little evidence for monosynaptic connectivity with V1. Yao and colleagues identified input to V1 from SC, even though the duration of rabies virus tracing is much shorter than in the TTT-MD experiments (2023). It could therefore be possible that the long tracing duration does not explain my observation, and that there is an extremely sparse monosynaptic connection that has previously been missed. We do not intend for TTT to be implemented as a tool to identify unknown patterns of structural connectivity, though. Rather, the aim of TTT is to identify changes in connectivity among brain regions that are known to connect to the starter cell region, but may have an unclear or uncertain role in a given plasticity paradigm. Overall, the locations of inputs to starter cells in V1 and their relative distribution is similar to what has been observed by the most recent and thorough study of rabies virus tracing to visual cortex (Yao et al., 2023).

4.2.2. Region-specific effects of MD found in TTT

One of the central aims of this thesis was to use MD as a paradigm to benchmark the ability of TTT to identify changes in circuitry known to participate in plasticity. OD plasticity in binocular visual cortex is associated with increased spine turnover and a net addition of new, lasting spines (Hofer et al., 2009), and so we expected to see a higher percentage of eGFP-only neurons in brain regions that likely project to these new, stable spines. Previous speculation regarding these new persistent spines was that they

represented an increase in input from the open eye, which, in adult mice, evokes stronger responses following MD (Sawtell et al., 2003). The representation of the open eye could be strengthened via new inputs to bV1 through several pathways, which are discussed in turn below.

4.2.2.1. Dorsal lateral geniculate nucleus

The first candidate region that we expected to show an effect of MD is the dLGN. The indication that MD affects the input from dLGN to cortex goes back to early work in OD plasticity in young monkeys, in which eye preference in cortex is organized into repeating bands called "ocular dominance (OD) columns." Hubel and Wiesel traced from the retina and used autoradiography of cortex to show that MD caused a marked reduction in the size of the columns representing the closed eye, even though the repeat distance remained similar, suggesting some combination of retraction of closed-eye inputs and/or expansion of open-eye inputs from dLGN (Hubel et al., 1977). Results from similar critical period experiments in both cats and mice showed retraction or shrinkage of dLGN axonal arbors representing the deprived eye, and expansion of open-eye axonal arbors after long periods of MD (Antonini et al., 1999; Antonini and Stryker, 1996). More recently, a role for thalamocortical input in adult mouse OD plasticity has also been shown. The shift in relative response strength towards the open, ipsilateral eye in bV1 relies heavily on synaptic inhibition from the dLGN (Qin et al., 2023). Taken together, we hypothesized that the fraction of eGFP-only neurons in the dLGN would also be higher in the adult mice that experienced MD as compared to controls. Indeed, this was the case (Fig. 3.11B).

An as-of-yet untested hypothesis regarding the plasticity of the projection from dLGN to V1 is that the strength of the effect of MD may vary within the dLGN. The dLGN is functionally divided. The core region preferentially responds to the contralateral eye but also contains neurons which receive ipsilateral eye input, while the remainder of the structure responds only to the contralateral eye (Kerschensteiner and Guido, 2017). Previous work has shown that MD leads to a strengthening of open-eye responses (Sawtell et al., 2003), and our study indicates that, following MD, the dLGN projects more strongly to bV1. It is possible that the Timeframe 2 neurons in the dLGN of MD mice reflect open-eye input, which should originate from the dLGN ipsilateral core. A more detailed spatial analysis could reveal if, indeed, the fraction of Timeframe 2 neurons is specifically higher in this ipsilateral eye-preferring region of the dLGN (see section 1.2.1.1). Ongoing analysis will address this hypothesis.

4.2.2.2. Intracortical connectivity

We also hypothesized that local connectivity within the visual cortex would be providing input to the newly-formed spines and would therefore show an effect of MD in the TTT experiments. In young cats, the effect of MD can be observed in upper cortical layers as early as 24 hours after onset of MD. The effect is in both the shift in responses of neurons in L2/3 (Trachtenberg et al., 2000) and in plasticity of connections between OD "zones," such that OD columns serving the same eye were more strongly interconnected than those serving opposite eyes following MD (Trachtenberg and Stryker, 2001). Additionally,

local inhibitory inputs have been shown to play a crucial role in critical period plasticity (Harauzov et al., 2010).

We did not observe an overall effect in V1 or in HVAs contralateral to the deprived eye (Fig. 3.11B, 3.12A), but, as with dLGN, we have not yet tested the hypothesis that the fraction of Timeframe 2 neurons may vary along retinotopic gradients in the cortex. In other words, the effect of MD in V1 and HVAs may be masked by pooling the data for the whole region instead of analyzing the spatial distribution of Timeframe 2 neurons. Mice do not have ocular dominance "columns" as canonically described in primates and cats, but there is recent evidence that neurons in mouse bV1 nevertheless cluster by eye preference (Goltstein et al., 2023). We would predict that the fraction of eGFP-only neurons in bV1 would vary as eye preference varies, which would suggest an increase in connectivity between neurons preferring the same eye.

4.2.2.3. Callosal projections from non-injected visual cortex

The visual cortices of each hemisphere are strongly interconnected via the corpus callosum. In adult rats, which normally do not show OD plasticity during MD, silencing the callosal inputs to the visual cortex contralateral to the closed eye caused a slight increase in the contralateral bias of neuronal responses (Restani et al., 2009). While I did not observe an effect of MD in the callosally-projecting V1, there was a significant effect in the HVAs in that hemisphere. Note, however, that the results presented here are drawn from a data set with potentially inaccurate registration to the Allen Atlas (see footnote 1, section 3.3.5). Given that V1 and most HVAs share borders, and that the density of labeling made it challenging to accurately identify these borders, I refrain from further interpretation of the absence of an effect in the callosally-projecting V1 ($p=0.065$, t-test) and the presence of this effect in HVAs.

As TTT is a newly developed approach for investigating brain-wide plasticity, it is not possible to draw meaning from these findings without context. In the TTT-MD experiment, this context is provided by previous work in adult OD plasticity. This means that the key take-away from this outcome is *not* that OD plasticity is primarily mediated by a change in the strength of projections from the dLGN and the opposite HVAs to the starter cells. The key take-away is that the readout of TTT is generally consistent with our hypotheses regarding where we expected to see higher percentages of eGFP-only cells, and is consistent with previous literature identifying a role for the dLGN projection and projections from various visual cortical regions in OD plasticity. In short, this result is important for confirming the functionality of TTT, but should not be seen as a robust and novel finding regarding OD plasticity. Rather, the finding that dLGN and the HVAs in the non-injected hemisphere show an effect of MD may be used to guide future experiments that aim to parse out the roles of these regions in OD plasticity.

4.2.3. Number of traced neurons may be higher in control mice

In the TTT experiments, I observed that the total number of rabies virus-traced neurons is higher in control mice than in MD mice (Fig. 3.10C). Though the difference was not statistically significant, it nevertheless warranted consideration. The finding holds true for

both the number of Timeframe 1 inputs, and the number of Timeframe 2 inputs. MD mice and control mice are cohoused, and treated the same throughout the experiment, with the exception of one additional surgical intervention (the eye suture), three injections of carprofen for analgesia, and the period of monocular deprivation. Control mice undergo anesthesia for anesthetized imaging lasting approximately one hour at the same point in the experimental timeline as the eye suture for MD mice, which excludes anesthesia alone as an explanation for the discrepancy. We developed three possible explanations for why monocular deprivation could lead to reduced rabies virus tracing. How each of these three explanations could result in a difference in the number of Timeframe 1 inputs is schematized in Figure 4.1.

The first explanation stems from how mice were divided into MD and control conditions (Fig. 4.1B). Rather than random assignment, I took note of each mouse's weight and of any signs of social hierarchy that were present in each cage. For example, some mice did not sleep in the hut in the cage, but instead slept alone. I very loosely interpreted this as evidence of social exclusion, and generally would not choose this mouse to be in the MD group, because social hierarchy is known to influence OD plasticity, particularly in male mice (Balog et al., 2019). Some mice lost more weight following initial surgeries than others, or were lighter by several grams than their cagemates. I also generally excluded these from the MD group. The eye suture surgery immediately follows 4OHT treatment (se Fig. 3.10A), making that period of the experiment very strenuous for the mouse. For this reason, heavier mice were chosen for the MD group. It is possible that these differences were systematic enough to influence the mean number of labeled cells for each group.

The second possibility is that Timeframe 1 is, as we expect, equivalent across groups, but that sensory deprivation and altered neuronal firing in MD mice renders Timeframe 1 neurons more vulnerable to rabies virus-related cell death (Fig. 4.1C). There is no indication in the literature that this might be the case, though.

The third explanation has two prongs, both of which must be true in order for this explanation to hold: It could be the case that 4OHT is not metabolized as quickly as we expect based on literature (Guenthner et al., 2013; Valny et al., 2016). At the same time, it could be possible that MD actually suppresses transsynaptic spread of the rabies virus, particularly during the first few days of eye closure, due to a drop in neuronal activity observed at the onset of MD (Hengen et al., 2013). This combination would mean that neurons infected for several days after 4OHT injection would still express both tdTomato and eGFP, and that there would be substantially more neurons infected during the initial days following 4OHT treatment in control mice as compared to MD mice (Fig. 4.1D).

We carefully considered whether this finding of increased labeling in both timeframes has any explanation that is more plausible than random chance. Given that the difference in number of traced neurons per micrometer of tissue imaged does not differ significantly between groups, we concluded that the most likely explanation is random chance and we therefore decided against further investigation of the issue for now. The three

explanations described above could serve as a guide for such investigation, should the issue present more strongly in future TTT experiments.

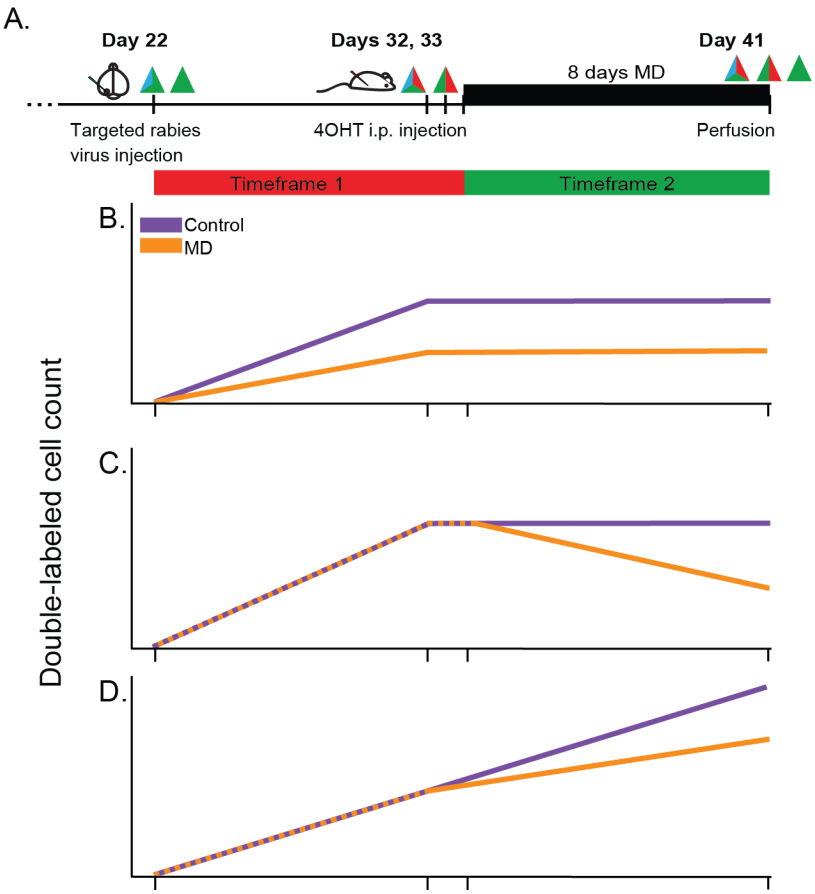

Figure 4.1. | Possible explanations for difference in number of Timeframe 1 neurons between groups. A: Shortened timeline of experiment described in Figure 3.10. **B:** Theoretical ramp-up of double-labeled neurons. Control mice and MD mice show unintentional systematic differences before the snapshot; more Timeframe 1 tracing occurs in controls. **C**: Timeframe 1 tracing is comparable across groups, but rabies virus-infected neurons die during MD. **D:** 4OHT is not cleared quickly, causing Timeframe 2 inputs to also be labeled with tdTomato, *and* MD suppresses transsynaptic tracing.

4.2.4. Which plasticity mechanisms are reflected by TTT?

So far, I have presented three key findings of the TTT-MD experiments. First, the components of TTT interact *in vitro* and *in vivo* the way they do in theory, with regard to the snapshot of Timeframe 1 inputs. Second, the overall anatomical results from the TTT experiment are consistent with results from other visual cortex connectivity studies. And third, the percentage of eGFP-only neurons (the key measure provided by TTT) differs significantly between the control group and the MD group. This difference was observed at the whole-brain level, as well as for specific regions like both ipsilateral and contralateral V1, and dLGN. In short, TTT was compatible with the study of OD plasticity; MD appears to have selectively increased the relative number of rabies virus-labeled cells in Timeframe 2.

There are a few possible ways to interpret the relationship between OD plasticity and the observation of a higher fraction of eGFP-only neurons observed in some brain regions. This observation could be linked to altered synaptic connectivity induced by MD; indeed, this is perhaps the most intuitive explanation for the effect we see. But in addition to an increase in lasting synapses, there are two other mechanisms that may explain the link between OD plasticity and increased rabies virus tracing: plasticity of existing synapses, and altered neuronal firing rates. Below, I discuss the plausibility of each of these three possible contributors.

One of the known effects of adult MD is a lasting increase in spine density on L5 neurons in bV1 (Hofer et al., 2009). These new, stable spines are indicative of an increase in connectivity, although the presynaptic partners have not been identified. The fraction of Timeframe 2 neurons in mice that experienced MD is, in all likelihood, partially composed of exactly those OD plasticity-related presynaptic partners. The increase in spine density induced by MD likely leads to a corresponding increase in rabies virus tracing in two ways: for presynaptic partners that were already connected prior to MD, but not infected by rabies virus until Timeframe 2, an increase in the number of spines connecting the two neurons also increases the likelihood of tracing. And for neurons that are newly incorporated into the circuit as a result of OD plasticity, rabies virus tracing simply could not have occurred during Timeframe 1. Though we cannot distinguish between neurons that were previously connected and may have increased the number of synaptic connections, and neurons that are novel presynaptic partners, both of these reflect the increase in connectivity induced by MD and are reflected by the increased relative number of rabies virus-traced neurons.

The second effect of adult MD that might result in increased rabies virus tracing is plasticity of synaptic strength, such as in the form of NMDA receptor-dependent long term potentiation (LTP) of thalamocortical synapses (Sawtell et al., 2003), or scaling of L2/3 synapses, which has been linked to EDP in the visual system but not directly to MD (Goel and Lee, 2007). It could be possible that a synapse forming a strong, functionally relevant connection has a higher probability of allowing transsynaptic spread of the rabies virus. Indeed, a study by Lavi et al. (2023) presents some evidence for preferential rabies virus tracing at strongly active connections. The authors biased starter cells to encode an experience and subsequently use the immediate early gene, c-fos, a well-established proxy for neuronal activity (Herrera and Robertson, 1996), to identify the full experience-encoding network. The authors interpret their finding that rabies virus tracing was preferentially observed in c-fos expressing cells as evidence that rabies virus transsynaptically spreads readily to neurons that are encoding the experience throughout the brain (Lavi et al., 2023).

Previously, I discussed evidence from the literature suggesting that rabies virus tracing is influenced more by structural connectivity than it is by functional connectivity (section 4.1.2.4). The studies described do not consider conditions where functional connectivity between two neurons or brain regions changes, though (Beier et al., 2017; Lerner et al.,

2015). Rather, one study reports on the *absence* of change in functional connectivity (Beier et al., 2017). The other study lacks a comparison of rabies virus tracing between animals undergoing a plasticity paradigm and a control group (Lerner et al., 2015). Although Lerner and colleagues showed a discrepancy between the strength of functional input and the relative amount of rabies virus tracing, this finding does not exclude the possibility that an increase in the functional connectivity of one region may also increase the likelihood of rabies virus infection. Whether there is a relationship between functional connectivity increases, and increased rabies virus tracing, is still uncertain. I therefore do not exclude the possibility that LTP, or other forms of increases in synapse strength, play a role in the observed increased fraction of Timeframe 2 neurons, particularly within the dLGN.

Beyond the changes in synaptic connectivity described above, there is another mechanism that may contribute to the likelihood of transsynaptic spread of rabies virus: neuronal activity and mode of firing (e.g., bursting or tonic firing patterns). It is important to consider the possibility that rabies virus tracing might be more influenced by increased neuronal firing, rather than by an increase in connectivity driven by new, stable spines and synaptic scaling. The correlation of firing is known to change in the context of juvenile OD plasticity, where initially the unstructured input from the closed eye to the dLGN leads to LTD, due to reduced correlation of firing from neurons that previously fired synchronously; following this initial change, responses are strengthened overall, likely via either homeostatic plasticity or LTP (Bienenstock et al., 1982; Blais et al., 1999; Mioche and Singer, 1989). In my TTT-MD experiments, adult OD plasticity is the focus, but it is probable that some of the same mechanisms apply as in juvenile plasticity. Although changes in firing rate may be correlated with changes in synaptic strength, it is also probable that firing rate in itself contributes to the likelihood of transsynaptic spread to a given neuron (Beier et al., 2017). The firing mode and rate changes associated with MD likely have an influence on the fraction of eGFP-only cells.

Each of these three mechanisms can link OD plasticity to an increase in rabies virus tracing, and each can therefore plausibly contribute to the effect seen in the TTT experiments. The mechanism that is best supported by previous findings is that the increase in new, stable spines enables increased rabies virus tracing to newly-connected neurons, while also increasing the likelihood of transsynaptic spread to neurons that increase their number of synaptic contacts. But plasticity of synapse strength and plasticity of firing rates likely also contribute to Timeframe 2 labeling in mice during MD. One of the main strengths of TTT is that it can identify changes in connectivity that arise from various synaptic plasticity mechanisms.

To concretely determine whether TTT specifically identifies brain regions that change their functional or structural connectivity with bV1 during OD plasticity, further experimentation would be needed. For instance, one could use an *ex vivo* strategy to measure the synaptic strength of inputs to bV1 that originate in various brain regions (see section 4.3.2). Alternatively, one could artificially increase or decrease neuronal activity

using optogenetic actuators and stimulation. Further experiments that incorporate measures of functional connectivity and neuronal activity between specific regions would help to clarify the relationship between functional strength of a connection, and the changes identified by TTT.

4.2.5. Shift magnitude after MD does not correlate with TTT's measurement of structural plasticity

In the TTT-MD experiments, I observed no significant correlation between the shift in ODI measured in bV1 and the percentage of eGFP-only inputs in either the whole brain or in specific regions affected by monocular deprivation (MD) (Supp. Fig. 4). It is possible that the functional plasticity seen in bV1 is not solely a result of the putative structural changes captured by TTT. But the lack of a correlation could also be due to a high level of noise, or other factors that we did not account for, which may significantly influence the readout of TTT.

The lack of correlation between structural and functional OD plasticity could be attributable to which plasticity mechanisms are and are not identified by TTT. The magnitude of the ODI shift in adult mice is at least in part determined by LTP at pre-existing synapses (Sawtell et al., 2003). Additionally, more stable spines on neurons do not necessarily translate to changes in the functional responses of those neurons. This discrepancy suggests that the presence of new spines or the stability of existing ones does not directly determine the functional plasticity measured by shifts in ODI.

There are several possible explanations for why functional plasticity does not correlate with structural plasticity as measured by TTT and spine turnover. For instance, the presynaptic partners of newly-formed or stable spines may not predominantly represent inputs from the open, unaffected eye. As a result, the changes in synaptic connections may not directly contribute to the functional shift in ODI. Another explanation is that homeostatic mechanisms may be at play, so that neurons that previously were driven primarily by the closed eye maintain overall input levels, though this is less likely in the adult animals used in my experiments (Mrsic-Flogel et al., 2007). In response to MD, a neuron might generally "seek out" new inputs, including through local connectivity, which would not necessarily cause a functional shift in ODI. The general take away is that functional plasticity (ODI shift) and structural plasticity (as measured by rabies virus labeling) may both result from MD, but they may operate through independent mechanisms. For example, while ODI shifts reflect changes in visual processing due to altered input, rabies virus tracing may label synapses that have become newly active due to MD, but these synapses may not be directly responsible for the ODI shift.

To further explore the relationship between structural and functional plasticity, one approach could involve using a rabies virus carrying the gene for a brighter fluorophore that ramps up more quickly. Faster expression of the fluorophore would allow experiments to be terminated after only 4-5 days of MD, a period that aligns with the ramp-up of spine turnover during MD (Hofer et al., 2009). By comparing TTT measurements during this early period to the spine turnover time course, we could

determine if structural changes occur on a similar timeline, even if they precede functional ODI shifts. Early MD tracing might reveal effects that align more closely with the time course of structural changes.

The disconnect between functional and structural plasticity does not invalidate the findings of TTT experiments, though. While functional changes like ODI shifts are a hallmark of plasticity in bV1, they may not reflect the underlying structural changes captured by TTT. Future experiments focused on earlier stages of MD, using tools that provide more temporally precise readouts, could help clarify the relationship between structural and functional plasticity.

4.3. Future directions

4.3.1. Suggested improvements of TTT

TTT, while promising as a methodological approach, requires several improvements upon how I implemented it here during development of the approach. I have previously described possible improvements to helper construct expression (section 4.1.1.4). While detectability of eGFP carried by the rabies virus did not pose a substantial challenge in the TTT-MD experiments, there is still room for improvement. Rabies virus-driven expression of eGFP is slow in comparison to ramp-up of tdTomato expression. Slower expression means that neurons infected with rabies virus towards the end of Timeframe 2 may not become visible, because there is not enough time for eGFP to express before the mouse is perfused. To increase visibility of late Timeframe 2 neurons, we have very recently designed a rabies virus that carries inducible Cre recombinase and a novel fluorophore, tdStayGold (Hirano et al., 2022), instead of eGFP. tdStayGold is substantially brighter than eGFP. Replacing eGFP with tdStayGold will likely decrease the ramp-up time needed for visibility of a rabies virus-infected neuron, and improve detection of Timeframe 2 neurons.

The procedure for imaging whole brains after perfusion can also be optimized. In the TTT-MD experiments described here, brains were cleared with X-Clarity™, sliced into thick 1mm sections, and then imaged with confocal microscopes. Originally, I planned to image cleared whole brains using a light sheet microscope. However, not all necessary filter sets were available for the light sheet microscope. The interim solution I used, confocal microscopy of thick slices, was not an ideal method for imaging, but was required at the time.

Serial two-photon tomography (STPT) is an imaging technique that improves upon the imaging process used here in several ways (Ragan et al., 2012). First, the brain does not need to be cleared, which means the tissue does not swell. Second, the brain is not sliced prior to imaging, but is rather sliced progressively during imaging. This allows for easier and more accurate registration of the images to a brain atlas because it results in continuous 3D volumetric images. And third, the imaging itself is faster than confocal imaging of cleared slices. One mouse brain can be imaged in approximately one day using STPT. With the confocal imaging pipeline I used, one brain required approximately 160

hours of confocal imaging. The acquisition for one slice lasted approximately 16 hours, and there were approximately ten slices per brain. We have recently performed a pilot experiment using STPT to image one mouse brain to confirm that eGFP and tdTomato can be easily distinguished, and that registration to an atlas is fast and accurate (data not shown). The result of this pilot confirmed that STPT is an ideal way to image whole brains after TTT experiments.

4.3.2. Improving the interpretability of TTT experiments

In addition to improvements for the TTT method itself, there are several experiments that could be done to lend more understanding to what, exactly, TTT is measuring. In other words, does a higher percentage of eGFP-only neurons reflect a lasting strengthened structural connection? An increased firing rate? Or some combination thereof?

The most important, incomplete piece of the puzzle is the exact nature of the relationship between rabies virus tracing, neuronal activity, and neuronal connectivity. To better understand the extent to which transsynaptic spread of rabies virus depends on these two factors, electrophysiological measurements of connectivity and activity should be made. Here, I describe a potential experiment investigating whether, in the TTT-MD paradigm, the projection from the contralateral visual cortex via the corpus callosum is stronger in MD mice than in controls, as my data potentially indicate (Figure 3.12A). The experiment would implement the principles of channelrhodopsin-2 (ChR2)-assisted circuit mapping (CRACM; Petreanu et al., 2007). First, I would inject an optogenetic actuator such as ChR2 unilaterally in V1, such that it expresses in somata in the injection region, but also in axon terminals in the opposite hemisphere's visual cortex. I would then suture the eye ipsilateral to the ChR2 injection. After eight days of MD, I would prepare acute slices from the hemisphere of the brain contralateral to the sutured eye. By holding each slice in ACSF containing TTX, all activity except for that induced by stimulation of the ChR2-expressing axons should be silenced. Patch clamp recordings of neurons in V1 during optogenetic stimulation of the opposite V1's afferents would give an indication of the strength of the projection. Comparing the strength of the projection in slices from mice who underwent MD, to that in control mice, would indicate whether MD actually increases the functional connectivity between these two regions, and whether functional connectivity may correlate with TTT outputs.

Similar experiments could be performed for various brain regions that show an effect, or the absence of an effect, in TTT experiments. The relationship between electrophysiological connection strength, and percentage of eGFP-only cells in a given region, would be a strong indicator of how to interpret the results of TTT experiments.

4.3.3. TTT in other paradigms

In this thesis, I have shown that TTT implemented in conjunction with monocular deprivation produces results consistent with what is known about OD plasticity. But more importantly, I have provided evidence that TTT is reliable enough to be implemented in conjunction with other paradigms, too. There are some limitations, imposed by timescales of various forms of learning, to what paradigms TTT can reasonably be applied

to. For TTT to provide useful information about brain regions contributing to plasticity, the majority of the learning or plasticity-inducing paradigm should take place during Timeframe 2. In the current setup of TTT, Timeframe 2 lasts only 8 days. Paradigms that are likely to be compatible with TTT include associative learning, such as conditioned taste aversion and contextual and cued fear conditioning, which are often learned with relatively little training on a time scale of just one day (Fanselow, 2010; Fanselow and Poulos, 2005; Foa et al., 1992; Garcia et al., 1955). Additionally, brain-wide contributions to rapid formation of addiction could be investigated using TTT (for a review of animal models of addiction, see Spanagel, 2017). Specific types of motor learning would also lend themselves for this purpose. For example, learning to perform a seed-grasping task induces substantial spine turnover in mouse motor cortex (Xu et al., 2009), and we have just started a project using TTT to identify the presynaptic partners of newly-formed spines in this paradigm.

One of the main limiting factors, in terms of what kinds of research questions can be investigated using TTT, is the duration needed for the ramp-up of helper virus expression. The fact that two weeks is needed between helper virus and rabies virus injections, and that doing so can be technically challenging in very young mice, means that TTT in its current iteration can only be performed in adult mice. However, if one were to express a helper construct using single-cell electroporation, and inject the rabies virus in the same surgical intervention, TTT could theoretically be performed in young mice. SCE of the helper construct opens the door to using TTT to investigate factors that influence formation of connectivity during development, which would be a powerful approach to such questions.

4.4. Conclusions

The implementation of TTT to investigate how brain-wide connectivity changes during MD revealed that two key regions, the dLGN and the callosally-projecting HVAs, show an effect of MD on the percentage of eGFP-only inputs to bV1. As dLGN and visual cortex connectivity are known to be involved in OD plasticity, this key result led to two main conclusions. First, that TTT can identify brain regions that provide input to starter cells and are undergoing synaptic plasticity. And second, that the roles of the dLGN and callosally-projecting HVAs in OD plasticity have yet to be fully understood.

Overall, the work presented here lays the groundwork for implementation of TTT as a tool for studying synaptic plasticity. In determining the key properties of TTT, and implementing it in mice undergoing OD plasticity, I established a basic protocol for future TTT experiments. I also highlight ways to improve each component, such that TTT could become an effective, efficient approach for studying how plasticity affects connectivity in the whole brain.

References

007909 - Ai9 or Ai9(RCL-tdT) Strain Details. n.d. https://www.jax.org/strain/007909

Abraham WC, Jones OD, Glanzman DL. 2019. Is plasticity of synapses the mechanism of long-term memory storage? *npj Sci Learn* **4**:1–10. doi:10.1038/s41539-019-0048-y

Albieri G, Barnes SJ, de Celis Alonso B, Cheetham CEJ, Edwards CE, Lowe AS, Karunaratne H, Dear JP, Lee KC, Finnerty GT. 2015. Rapid bidirectional reorganization of cortical microcircuits. *Cereb Cortex* **25**:3025–3035. doi:10.1093/cercor/bhu098

Albisetti GW, Ghanem A, Foster E, Conzelmann K-K, Zeilhofer HU, Wildner H. 2017. Identification of two classes of somatosensory neurons that display resistance to retrograde infection by rabies virus. *J Neurosci* **37**:10358–10371. doi:10.1523/JNEUROSCI.1277-17.2017

Allen AE, Procyk CA, Howarth M, Walmsley L, Brown TM. 2016. Visual input to the mouse lateral posterior and posterior thalamic nuclei: photoreceptive origins and retinotopic order. *J Physiol* **594**:1911–1929. doi:10.1113/JP271707

Antonini A, Fagiolini M, Stryker MP. 1999. Anatomical correlates of functional plasticity in mouse visual cortex. *J Neurosci* **19**:4388–4406. doi:10.1523/JNEUROSCI.19-11-04388.1999

Antonini A, Stryker MP. 1996. Plasticity of geniculocortical afferents following brief or prolonged monocular occlusion in the cat. *J Comp Neurol* **369**:64–82. doi:10.1002/(SICI)1096-9861(19960520)369:1<64::AID-CNE5>3.0.CO;2-I

Attardo A, Fitzgerald JE, Schnitzer MJ. 2015. Impermanence of dendritic spines in live adult CA1 hippocampus. *Nature* **523**:592–596. doi:10.1038/nature14467

Babakhanova S, Jung EE, Namikawa K, Zhang H, Wang Y, Subach OM, Korzhenevskiy DA, Rakitina TV, Xiao X, Wang W, Shi J, Drobizhev M, Park D, Eisenhard L, Tang H, Köster RW, Subach FV, Boyden ES, Piatkevich KD. 2022. Rapid directed molecular evolution of fluorescent proteins in mammalian cells. *Protein Sci* **31**:728–751. doi:10.1002/pro.4261

Bailey CH, Kandel ER. 1993. Structural changes accompanying memory storage. *Annu Rev Physiol* **55**:397–426. doi:10.1146/annurev.ph.55.030193.002145

Bailey CH, Kandel ER, Harris KM. 2015. Structural components of synaptic plasticity and memory consolidation. *Cold Spring Harb Perspect Biol* **7**:a021758. doi:10.1101/cshperspect.a021758

Balog J, Hintz F, Isstas M, Teichert M, Winter C, Lehmann K. 2019. Social hierarchy regulates ocular dominance plasticity in adult male mice. *Brain Struct Funct* **224**:3183–3199. doi:10.1007/s00429-019-01959-w

Barnes SJ, Cheetham CE, Liu Y, Bennett SH, Albieri G, Jorstad AA, Knott GW, Finnerty GT. 2015. Delayed and temporally imprecise neurotransmission in reorganizing cortical microcircuits. *J Neurosci* **35**:9024–9037. doi:10.1523/JNEUROSCI.4583-14.2015

Bastos V, Pacheco V, Rodrigues ÉDL, Moraes CNS, Nóbile AL, Fonseca DLM, Souza KBS, do Vale FYN, Filgueiras IS, Schimke LF, Giil LM, Moll G, Cabral-Miranda G, Ochs HD, Vasconcelos PF da C, de Melo GD, Bourhy H, Casseb LMN, Cabral-Marques O. 2023. Neuroimmunology of rabies: New insights into an ancient disease. *J Med Virol* **95**:e29042. doi:10.1002/jmv.29042

Bauer A, Nolden T, Nemitz S, Perlson E, Finke S. 2015. A dynein light chain 1 binding motif in rabies virus polymerase L protein plays a role in microtubule reorganization and viral primary transcription. *J Virol* **89**:9591–9600. doi:10.1128/JVI.01298-15

Bauer A, Nolden T, Schröter J, Römer-Oberdörfer A, Gluska S, Perlson E, Finke S. 2014. Anterograde glycoprotein-dependent transport of newly generated rabies virus in dorsal root ganglion neurons. *J Virol* **88**:14172–14183. doi:10.1128/JVI.02254-14

Bauer J, Weiler S, Fernholz MHP, Laubender D, Scheuss V, Hübener M, Bonhoeffer T, Rose T. 2021. Limited functional convergence of eye-specific inputs in the retinogeniculate pathway of the mouse. *Neuron* **109**:2457-2468.e12. doi:10.1016/j.neuron.2021.05.036

Beier KT, Kim CK, Hoerbelt P, Hung LW, Heifets BD, DeLoach KE, Mosca TJ, Neuner S, Deisseroth K, Luo L, Malenka RC. 2017. Rabies screen reveals GPe control of cocaine-triggered plasticity. *Nature* **549**:345–350. doi:10.1038/nature23888

Bhatt DH, Zhang S, Gan W-B. 2009. Dendritic Spine Dynamics. *Annu Rev Physiol* **71**:261–282. doi:10.1146/annurev.physiol.010908.163140

Bienenstock EL, Cooper LN, Munro PW. 1982. Theory for the development of neuron selectivity: orientation specificity and binocular interaction in visual cortex. *J Neurosci* **2**:32–48. doi:10.1523/JNEUROSCI.02-01-00032.1982

Blais BS, Shouval HZ, Cooper LN. 1999. The role of presynaptic activity in monocular deprivation: comparison of homosynaptic and heterosynaptic mechanisms. *Proc Natl Acad Sci USA* **96**:1083–1087. doi:10.1073/pnas.96.3.1083

Bliss TVP, Lømo T. 1973. Long-lasting potentiation of synaptic transmission in the dentate area of the anaesthetized rabbit following stimulation of the perforant path. *J Physiol* **232**:331–356. doi:10.1113/jphysiol.1973.sp010273

Bonhoeffer T, Grinvald A. 1991. Iso-orientation domains in cat visual cortex are arranged in pinwheel-like patterns. *Nature* **353**:429–431. doi:10.1038/353429a0

Bonhoeffer T, Hübener M. 2016. Intrinsic optical imaging of functional map development in mammalian visual cortex. *Cold Spring Harb Protoc* **2016**. doi:10.1101/pdb.top089383

Bonhoeffer T, Kim DS, Malonek D, Shoham D, Grinvald A. 1995. Optical imaging of the layout of functional domains in area 17 and across the area 17/18 border in cat visual cortex. *Eur J Neurosci* **7**:1973–1988. doi:10.1111/j.1460-9568.1995.tb00720.x

Bonin V, Histed MH, Yurgenson S, Reid RC. 2011. Local diversity and fine-scale organization of receptive fields in mouse visual cortex. *J Neurosci* **31**:18506–18521. doi:10.1523/JNEUROSCI.2974-11.2011

Bracci L, Antoni G, Cusi MG, Lozzi L, Niccolai N, Petreni S, Rustici M, Santucci A, Soldani P, Valensin PE. 1988. Antipeptide monoclonal antibodies inhibit the binding of rabies virus glycoprotein and alpha-bungarotoxin to the nicotinic acetylcholine receptor. *Mol Immunol* **25**:881–888. doi:10.1016/0161-5890(88)90125-3

Briggs F. 2020. Role of feedback connections in central visual processing. *Annu Rev Vis Sci* **6**:313–334. doi:10.1146/annurev-vision-121219-081716

Callaway EM, Luo L. 2015. Monosynaptic circuit tracing with glycoprotein-deleted rabies viruses. *J Neurosci* **35**:8979–8985. doi:10.1523/JNEUROSCI.0409-15.2015

Carl Zeiss Microscopy GmbH. 2023. arivis Cloud. https://www.arivis.cloud/home

Casanova E, Fehsenfeld S, Lemberger T, Shimshek DR, Sprengel R, Mantamadiotis T. 2002. ER-based double icre fusion protein allows partial recombination in forebrain. *Genesis* **34**:208–214. doi:10.1002/gene.10153

Chan KY, Jang MJ, Yoo BB, Greenbaum A, Ravi N, Wu W-L, Sánchez-Guardado L, Lois C, Mazmanian SK, Deverman BE, Gradinaru V. 2017. Engineered AAVs for efficient noninvasive gene delivery to the central and peripheral nervous systems. *Nat Neurosci* **20**:1172–1179. doi:10.1038/nn.4593

Chan YK, Wang SK, Chu CJ, Copland DA, Letizia AJ, Verdera HC, Chiang JJ, Sethi M, Wang MK, Neidermyer WJ, Chan Y, Lim ET, Graveline AR, Sanchez M, Boyd RF, Vihtelic TS, Inciong RGCO, Slain JM, Alphonse PJ, Xue Y, Robinson-McCarthy LR, Tam JM, Jabbar MH, Sahu B, Adeniran JF, Muhuri M, Tai PWL, Xie J, Krause TB, Vernet A, Pezone M, Xiao R, Liu T, Wang W, Kaplan HJ, Gao G, Dick AD, Mingozzi F, McCall MA, Cepko CL, Church GM. 2021. Engineering adeno-associated viral vectors to evade innate immune and inflammatory responses. *Sci Transl Med* **13**:eabd3438. doi:10.1126/scitranslmed.abd3438

Chatterjee S, Sullivan HA, MacLennan BJ, Xu R, Hou Y, Lavin TK, Lea NE, Michalski JE, Babcock KR, Dietrich S, Matthews GA, Beyeler A, Calhoon GG, Glober G, Whitesell JD, Yao S, Cetin A, Harris JA, Zeng H, Tye KM, Reid RC, Wickersham IR. 2018. Nontoxic, double-deletion-mutant rabies viral vectors for retrograde targeting of projection neurons. *Nat Neurosci* **21**:638–646. doi:10.1038/s41593-018-0091-7

Chklovskii DB, Mel BW, Svoboda K. 2004. Cortical rewiring and information storage. *Nature* **431**:782–788. doi:10.1038/nature03012

Ciabatti E, González-Rueda A, de Malmazet D, Lee H, Morgese F, Tripodi M. 2023. Genomic stability of self-inactivating rabies. *eLife* **12**:e83459. doi:10.7554/eLife.83459

Ciabatti E, González-Rueda A, Mariotti L, Morgese F, Tripodi M. 2017. Life-long genetic and functional access to neural circuits using self-inactivating rabies virus. *Cell* **170**:382-392.e14. doi:10.1016/j.cell.2017.06.014

Coleman JE, Law K, Bear MF. 2009. Anatomical origins of ocular dominance in mouse primary visual cortex. *J Neurosci* **161**:561–571. doi:10.1016/j.neuroscience.2009.03.045

Craddock R, Vasalauskaite A, Ranson A, Sengpiel F. 2023. Experience dependent plasticity of higher visual cortical areas in the mouse. *Cereb Cortex* **33**:9303–9312. doi:10.1093/cercor/bhad203

Cremer H, Lange R, Christoph A, Plomann M, Vopper G, Roes J, Brown R, Baldwin S, Kraemer P, Scheff S. 1994. Inactivation of the N-CAM gene in mice results in size reduction of the olfactory bulb and deficits in spatial learning. *Nature* **367**:455–459. doi:10.1038/367455a0

DeNardo LA, Berns DS, DeLoach K, Luo L. 2015. Connectivity of mouse somatosensory and prefrontal cortex examined with trans-synaptic tracing. *Nat Neurosci* **18**:1687–1697. doi:10.1038/nn.4131

Douglas RJ, Martin KA. 1991. A functional microcircuit for cat visual cortex. *J Physiol* **440**:735–769.

Douglas RJ, Martin KAC, Whitteridge D. 1989. A canonical microcircuit for neocortex. *Neural Comput* **1**:480–488. doi:10.1162/neco.1989.1.4.480

Drager UC. 1978. Observations on monocular deprivation in mice. *J Neurophysiol* **41**:28–42. doi:10.1152/jn.1978.41.1.28

Dräger UC. 1975. Receptive fields of single cells and topography in mouse visual cortex. *J Comp Neurol* **160**:269–289. doi:10.1002/cne.901600302

Dräger UC, Olsen JF. 1980. Origins of crossed and uncrossed retinal projections in pigmented and albino mice. *J Comp Neurol* **191**:383–412. doi:10.1002/cne.901910306

Dudek SM, Bear MF. 1992. Homosynaptic long-term depression in area CA1 of hippocampus and effects of N-methyl-D-aspartate receptor blockade. *Proc Natl Acad Sci USA* **89**:4363–4367. doi:10.1073/pnas.89.10.4363

Ellis EM, Gauvain G, Sivyer B, Murphy GJ. 2016. Shared and distinct retinal input to the mouse superior colliculus and dorsal lateral geniculate nucleus. *J Neurophysiol* **116**:602–610. doi:10.1152/jn.00227.2016

Espinosa JS, Stryker MP. 2012. Development and plasticity of the primary visual cortex. *Neuron* **75**:230–249. doi:10.1016/j.neuron.2012.06.009

Faber M, Pulmanausahakul R, Hodawadekar SS, Spitsin S, McGettigan JP, Schnell MJ, Dietzschold B. 2002. Overexpression of the rabies virus glycoprotein results in enhancement of apoptosis and antiviral immune response. *J Virol* **76**:3374. doi:10.1128/JVI.76.7.3374-3381.2002

Faget L, Osakada F, Duan J, Ressler R, Johnson AB, Proudfoot JA, Yoo JH, Callaway EM, Hnasko TS. 2016. Afferent inputs to neurotransmitter-defined cell types in the ventral tegmental area. *Cell Reports* **15**:2796–2808. doi:10.1016/j.celrep.2016.05.057

Fagiolini M, Pizzorusso T, Berardi N, Domenici L, Maffei L. 1994. Functional postnatal development of the rat primary visual cortex and the role of visual experience: Dark rearing and monocular deprivation. *Vis Res* **34**:709–720. doi:10.1016/0042-6989(94)90210-0

Falkner S, Grade S, Dimou L, Conzelmann K-K, Bonhoeffer T, Götz M, Hübener M. 2016. Transplanted embryonic neurons integrate into adult neocortical circuits. *Nature* **539**:248–253. doi:10.1038/nature20113

Fanselow MS. 2010. From contextual fear to a dynamic view of memory systems. *Trends Cog Sci* **14**:7–15. doi:10.1016/j.tics.2009.10.008

Fanselow MS, Poulos AM. 2005. The neuroscience of mammalian associative learning. *Annu Rev Psych* **56**:207–234. doi:10.1146/annurev.psych.56.091103.070213

Fauth M, Wörgötter F, Tetzlaff C. 2015. The formation of multi-synaptic connections by the interaction of synaptic and structural plasticity and their functional consequences. *PLoS Comput Biol* **11**:e1004031. doi:10.1371/journal.pcbi.1004031

Federspiel MJ, Bates P, Young JA, Varmus HE, Hughes SH. 1994. A system for tissue-specific gene targeting: transgenic mice susceptible to subgroup A avian leukosis virus-based retroviral vectors. *Proc Natl Acad Sci USA* **91**:11241–11245. doi:10.1073/pnas.91.23.11241

Foa EB, Zinbarg R, Rothbaum BO. 1992. Uncontrollability and unpredictability in post-traumatic stress disorder: an animal model. *Psychol Bull* **112**:218–238. doi:10.1037/0033-2909.112.2.218

Frenkel MY, Bear MF. 2004. How monocular deprivation shifts ocular dominance in visual cortex of young mice. *Neuron* **44**:917–923. doi:10.1016/j.neuron.2004.12.003

Garcia J, Kimeldorf DJ, Koelling RA. 1955. Conditioned aversion to saccharin resulting from exposure to gamma radiation. *Science* **122**:157–158.

Ginger M, Haberl M, Conzelmann K-K, Schwarz MK, Frick A. 2013. Revealing the secrets of neuronal circuits with recombinant rabies virus technology. *Front Neural Circuits* **7**:2. doi:10.3389/fncir.2013.00002

Goel A, Lee H-K. 2007. Persistence of experience-induced homeostatic synaptic plasticity through adulthood in superficial layers of mouse visual cortex. *J Neurosci* **27**:6692. doi:10.1523/JNEUROSCI.5038-06.2007

Goltstein PM, Laubender D, Bonhoeffer T, Hübener M. 2023. Ocular dominance columns in mouse visual cortex. *bioRxiv.* doi:10.1101/2023.07.22.550034

Goltstein PM, Reinert S, Bonhoeffer T, Hübener M. 2021. Mouse visual cortex areas represent perceptual and semantic features of learned visual categories. *Nat Neurosci* **24**:1441–1451. doi:10.1038/s41593-021-00914-5

Gordon JA, Stryker MP. 1996. Experience-dependent plasticity of binocular responses in the primary visual cortex of the mouse. *J Neurosci* **16**:3274–3286. doi:10.1523/JNEUROSCI.16-10-03274.1996

Graf W, Gerrits N, Yatim-Dhiba N, Ugolini G. 2002. Mapping the oculomotor system: The power of transneuronal labelling with rabies virus. *Eur J Neurosci* **15**:1557–1562. doi:10.1046/j.1460-9568.2002.01994.x

Greenough WT, Bailey CH. 1988. The anatomy of a memory: convergence of results across a diversity of tests. *Trends Neurosci* **11**:142–147. doi:10.1016/0166-2236(88)90139-7

Greifzu F, Kalogeraki E, Löwel S. 2016. Environmental enrichment preserved lifelong ocular dominance plasticity, but did not improve visual abilities. *Neurobiol Aging* **41**:130–137. doi:10.1016/j.neurobiolaging.2016.02.014

Grinvald A, Lieke E, Frostig RD, Gilbert CD, Wiesel TN. 1986. Functional architecture of cortex revealed by optical imaging of intrinsic signals. *Nature* **324**:361–364. doi:10.1038/324361a0

Groeneboom NE, Yates SC, Puchades MA, Bjaalie JG. 2020. Nutil: A pre- and post-processing toolbox for histological rodent brain section images. *Front Neuroinform* **14**:37. doi:10.3389/fninf.2020.00037

Guenthner CJ, Miyamichi K, Yang HH, Heller HC, Luo L. 2013. Permanent genetic access to transiently active neurons via TRAP: targeted recombination in active populations. *Neuron* **78**:773–784. doi:10.1016/j.neuron.2013.03.025

Guire ES, Lickey ME, Gordon B. 1999. Critical period for the monocular deprivation effect in rats: assessment with sweep visually evoked potentials. *J Neurophysiol* **81**:121–128. doi:10.1152/jn.1999.81.1.121

Guo Y, Duan M, Wang X, Gao J, Guan Z, Zhang M. 2019. Early events in rabies virus infection—Attachment, entry, and intracellular trafficking. *Virus Research* **263**:217–225. doi:10.1016/j.virusres.2019.02.006

Haas K, Sin WC, Javaherian A, Li Z, Cline HT. 2001. Single-cell electroporation for gene transfer in vivo. *Neuron* **29**:583–591. doi:10.1016/s0896-6273(01)00235-5

Halpage J, DaSilva Pantoja P, Mancarella S. 2024. Prolonged tamoxifen-enriched diet is associated with cardiomyopathy and nutritional frailty in mice. *Exp Phys* **109**:513–523. doi:10.1113/EP091668

Han R-W, Zhang Z-Y, Jiao C, Hu Z-Y, Pan B-X. 2024. Synergism between two BLA-to-BNST pathways for appropriate expression of anxiety-like behaviors in male mice. *Nat Commun* **15**:3455. doi:10.1038/s41467-024-47966-2

Harauzov A, Spolidoro M, DiCristo G, De Pasquale R, Cancedda L, Pizzorusso T, Viegi A, Berardi N, Maffei L. 2010. Reducing intracortical inhibition in the adult visual cortex promotes ocular dominance plasticity. *J Neurosci* **30**:361–371. doi:10.1523/JNEUROSCI.2233-09.2010

Hebb, D.O. 1949. The Organization of Behavior. New York: Wiley.

Heesy CP. 2004. On the relationship between orbit orientation and binocular visual field overlap in mammals. *Anat Rec A Discov Mol Cell Evol Biol.* **281**:1104–1110. doi:10.1002/ar.a.20116

Heimel JA, Hermans JM, Sommeijer J-P, Consortium N-BMP, Levelt CN. 2008. Genetic control of experience-dependent plasticity in the visual cortex. *Genes Brain Behav* **7**:915–923. doi:10.1111/j.1601-183X.2008.00431.x

Hemachudha T, Wacharapluesadee S, Mitrabhakdi E, Wilde H, Morimoto K, Lewis AR. 2005. Pathophysiology of human paralytic rabies. *J Neurovirol* **11**:93–100. doi:10.1080/13550280590900409

Hengen KB, Lambo ME, Van Hooser SD, Katz DB, Turrigiano GG. 2013. Firing rate homeostasis in visual cortex of freely behaving rodents. *Neuron* **80**:335–342. doi:10.1016/j.neuron.2013.08.038

Herrera DG, Robertson HA. 1996. Activation of c-fos in the brain. *Prog Neurobiol* **50**:83–107. doi:10.1016/s0301-0082(96)00021-4

Heynen AJ, Yoon B-J, Liu C-H, Chung HJ, Huganir RL, Bear MF. 2003. Molecular mechanism for loss of visual cortical responsiveness following brief monocular deprivation. *Nat Neurosci* **6**:854–862. doi:10.1038/nn1100

Hirano M, Ando R, Shimozono S, Sugiyama M, Takeda N, Kurokawa H, Deguchi R, Endo K, Haga K, Takai-Todaka R, Inaura S, Matsumura Y, Hama H, Okada Y, Fujiwara T, Morimoto T, Katayama K, Miyawaki A. 2022. A highly photostable and bright green fluorescent protein. *Nat Biotechnol* **40**:1132–1142. doi:10.1038/s41587-022-01278-2

Hofer SB, Mrsic-Flogel TD, Bonhoeffer T, Hübener M. 2009. Experience leaves a lasting structural trace in cortical circuits. *Nature* **457**:313–317. doi:10.1038/nature07487

Hofer SB, Mrsic-Flogel TD, Bonhoeffer T, Hübener M. 2006. Prior experience enhances plasticity in adult visual cortex. *Nat Neurosci* **9**:127–132. doi:10.1038/nn1610

Holtmaat A, Svoboda K. 2009. Experience-dependent structural synaptic plasticity in the mammalian brain. *Nat Rev Neurosci* **10**:647–658. doi:10.1038/nrn2699

Huang KW, Sabatini BL. 2020. Single-cell analysis of neuroinflammatory responses following intracranial injection of G-deleted rabies viruses. *Front Cell Neurosci* **14**:65. doi:10.3389/fncel.2020.00065

Hubel DH, Wiesel TN. 1968. Receptive fields and functional architecture of monkey striate cortex. *J Physiol* **195**:215–243. doi:10.1113/jphysiol.1968.sp008455

Hubel DH, Wiesel TN. 1962. Receptive fields, binocular interaction and functional architecture in the cat's visual cortex. *J Physiol* **160**:106-154.2. doi:10.1113/jphysiol.1962.sp006837

Hubel DH, Wiesel TN, LeVay S. 1977. Plasticity of ocular dominance columns in monkey striate cortex. *Philos Trans R Soc Lond B Biol Sci* **278**:377–409. doi:10.1098/rstb.1977.0050

Hübener M, Bonhoeffer T. 2014. Neuronal plasticity: Beyond the critical period. *Cell* **159**:727-737. doi:10.1016/j.cell.2014.10.035

Hübener M, Bonhoeffer T. 2010. Searching for engrams. *Neuron* **67**:363–371. doi:10.1016/j.neuron.2010.06.033

Huh WJ, Khurana SS, Geahlen JH, Kohli K, Waller RA, Mills JC. 2012. Tamoxifen induces rapid, reversible atrophy and metaplasia in mouse stomach. *Gastroenterology* **142**:21-24.e7. doi:10.1053/j.gastro.2011.09.050

Hulett HR, Bonner WA, Barrett J, Herzenberg LA. 1969. Cell sorting: automated separation of mammalian cells as a function of intracellular fluorescence. *Science* **166**:747–749. doi:10.1126/science.166.3906.747

Indra AK, Warot X, Brocard J, Bornert JM, Xiao JH, Chambon P, Metzger D. 1999. Temporally-controlled site-specific mutagenesis in the basal layer of the epidermis: comparison of the recombinase activity of the tamoxifen-inducible Cre-ER(T) and Cre-ER(T2) recombinases. *Nucleic Acids Res* **27**:4324–4327. doi:10.1093/nar/27.22.4324

Jaepel J, Hübener M, Bonhoeffer T, Rose T. 2017. Lateral geniculate neurons projecting to primary visual cortex show ocular dominance plasticity in adult mice. *Nat Neurosci* **20**:1708–1714. doi:10.1038/s41593-017-0021-0

Jahn HM, Kasakow CV, Helfer A, Michely J, Verkhratsky A, Maurer HH, Scheller A, Kirchhoff F. 2018. Refined protocols of tamoxifen injection for inducible DNA recombination in mouse astroglia. *Sci Rep* **8**:5913. doi:10.1038/s41598-018-24085-9

James W. 1890. The Principles of Psychology. Henry Holt and Comp.

Jin L, Matsuyama M, Sullivan HA, Zhu M, Lavin TK, Hou Y, Lea NE, Pruner MT, Dam Ferdínez ML, Wickersham IR. 2023a. “Self-inactivating” rabies viruses are susceptible to loss of their intended attenuating modification. *Proc Natl Acad Sci USA* **120**:e2023481120. doi:10.1073/pnas.2023481120

Jin L, Sullivan HA, Zhu M, Lavin TK, Matsuyama M, Fu X, Lea NE, Xu R, Hou Y, Rutigliani L, Pruner M, Babcock KR, Ip JPK, Hu M, Daigle TL, Zeng H, Sur M, Feng G, Wickersham IR. 2024. Long-term labeling and imaging of synaptically connected neuronal networks in vivo using double-deletion-mutant rabies viruses. *Nat Neurosci* 1–11. doi:10.1038/s41593-023-01545-8

Jin L, Sullivan HA, Zhu M, Lea NE, Lavin TK, Fu X, Matsuyama M, Hou Y, Feng G, Wickersham IR. 2023b. Single-deletion-mutant, third-generation rabies viral vectors allow nontoxic retrograde targeting of projection neurons with greatly increased efficiency. *Cell Rep Methods* **3**:100644 doi:10.1101/2022.02.23.481706

Jones EG. 1994. Santiago Ramón y Cajal and the Croonian Lecture, March 1894. *Trends Neurosci* **17**:190–192. doi:10.1016/0166-2236(94)90100-7

Jung CKE, Herms J. 2014. Structural dynamics of dendritic spines are influenced by an environmental enrichment: an in vivo imaging study. *Cereb Cortex* **24**:377–384. doi:10.1093/cercor/bhs317

Kaas JH, Krubitzer LA, Chino YM, Langston AL, Polley EH, Blair N. 1990. Reorganization of retinotopic cortical maps in adult mammals after lesions of the retina. *Science* **248**:229–231. doi:10.1126/science.2326637

Kalogeraki E, Greifzu F, Haack F, Löwel S. 2014. Voluntary physical exercise promotes ocular dominance plasticity in adult mouse primary visual cortex. *J Neurosci* **34**:15476–15481. doi:10.1523/JNEUROSCI.2678-14.2014

Kalogeraki E, Pielecka-Fortuna J, Löwel S. 2017. Environmental enrichment accelerates ocular dominance plasticity in mouse visual cortex whereas transfer to standard

cages resulted in a rapid loss of increased plasticity. *PLoS One* **12**:e0186999. doi:10.1371/journal.pone.0186999

Kaplan MS, Hinds JW. 1977. Neurogenesis in the adult rat: electron microscopic analysis of light radioautographs. *Science* **197**:1092–1094. doi:10.1126/science.887941

Kasper EM, Larkman AU, Lübke J, Blakemore C. 1994. Pyramidal neurons in layer 5 of the rat visual cortex. I. Correlation among cell morphology, intrinsic electrophysiological properties, and axon targets. *J Comp Neurol* **339**:459–474. doi:10.1002/cne.903390402

Keck T, Mrsic-Flogel TD, Vaz Afonso M, Eysel UT, Bonhoeffer T, Hübener M. 2008. Massive restructuring of neuronal circuits during functional reorganization of adult visual cortex. *Nat Neurosci* **11**:1162–1167. doi:10.1038/nn.2181

Keller AJ, Roth MM, Scanziani M. 2020. Feedback generates a second receptive field in neurons of the visual cortex. *Nature* **582**:545–549. doi:10.1038/s41586-020-2319-4

Kerschensteiner D, Guido W. 2017. Organization of the dorsal lateral geniculate nucleus in the mouse. *Vis Neurosci* **34**:E008. doi: 10.1017/S0952523817000062.

Khibnik LA, Tritsch NX, Sabatini BL. 2014. A direct projection from mouse primary visual cortex to dorsomedial striatum. *PLoS One* **9**:e104501. doi:10.1371/journal.pone.0104501

Kiermayer C, Conrad M, Schneider M, Schmidt J, Brielmeier M. 2007. Optimization of spatiotemporal gene inactivation in mouse heart by oral application of tamoxifen citrate. *Genesis* **45**:11–16. doi:10.1002/dvg.20244

Kim JJ, Fanselow MS. 1992. Modality-specific retrograde amnesia of fear. *Science* **256**:675–677. doi:10.1126/science.1585183

Kim KH, Singha S, Jun YW, Reo YJ, Kim HR, Ryu HG, Bhunia S, Ahn KH. 2019. Far-red/near-infrared emitting, two-photon absorbing, and bio-stable amino-Si-pyronin dyes. *Chem Sci* **10**:9028–9037. doi:10.1039/c9sc02287b

Kim S, Larrous F, Varet H, Legendre R, Feige L, Dumas G, Matsas R, Kouroupi G, Grailhe R, Bourhy H. 2021. Early transcriptional changes in rabies virus-infected neurons and their impact on neuronal functions. *Front Microbiol* **12**:730892. doi:10.3389/fmicb.2021.730892

Klingen Y, Conzelmann K-K, Finke S. 2008. Double-labeled rabies virus: live tracking of enveloped virus transport. *J Virol* **82**:237–245. doi:10.1128/JVI.01342-07

Knott GW, Holtmaat A, Wilbrecht L, Welker E, Svoboda K. 2006. Spine growth precedes synapse formation in the adult neocortex in vivo. *Nat Neurosci* **9**:1117–1124. doi:10.1038/nn1747

Kreile AK, Bonhoeffer T, Hübener M. 2011. Altered visual experience induces instructive changes of orientation preference in mouse visual cortex. *J Neurosci* **31**:13911–13920. doi:10.1523/JNEUROSCI.2143-11.2011

Lafon M. 2005. Rabies virus receptors. *J Neurovirol* **11**:82–87. doi:10.1080/13550280590900427

Lavi A, Sehgal M, de Sousa AF, Ter-Mkrtchyan D, Sisan F, Luchetti A, Okabe A, Bear C, Silva AJ. 2023. Local memory allocation recruits memory ensembles across brain regions. *Neuron* **111**:470-480.e5. doi:10.1016/j.neuron.2022.11.018

Lavin TK, Jin L, Lea NE, Wickersham IR. 2020. Monosynaptic tracing success depends critically on helper virus concentrations. *Front Synaptic Neurosci* **12**:6. doi:10.3389/fnsyn.2020.00006

Lerner TN, Shilyansky C, Davidson TJ, Evans KE, Beier KT, Zalocusky KA, Crow AK, Malenka RC, Luo L, Tomer R, Deisseroth K. 2015. Intact-brain analyses reveal distinct information carried by SNc dopamine subcircuits. *Cell* **162**:635–647. doi:10.1016/j.cell.2015.07.014

Leuner B, Falduto J, Shors TJ. 2003. Associative memory formation increases the observation of dendritic spines in the hippocampus. *J Neurosci* **23**:659–665. doi:10.1523/JNEUROSCI.23-02-00659.2003

LeVay S, Hubel DH, Wiesel TN. 1975. The pattern of ocular dominance columns in macaque visual cortex revealed by a reduced silver stain. *J Comp Neurol* **159**:559–575. doi:10.1002/cne.901590408

Li A, Cornelius SP, Liu Y-Y, Wang L, Barabási A-L. 2017. The fundamental advantages of temporal networks. *Science* **358**:1042–1046. doi:10.1126/science.aai7488

Li S, Chen L, Peng X, Wang C, Qin B, Tan D, Han C, Yang H, Ren X, Liu F, Xu C, Zhou X. 2018. Overview of the reporter genes and reporter mouse models. *Animal Model Exp Med* **1**:29–35. doi:10.1002/ame2.12008

Lickey ME, Pham TA, Gordon B. 2004. Swept contrast visual evoked potentials and their plasticity following monocular deprivation in mice. *Vis Res* **44**:3381–3387. doi:10.1016/j.visres.2004.09.018

Liu J, Li W, Yu D, Jin R, Hou H, Ling X, Kiflu AB, Wei X, Yang X, Li X, He Y, Luo TR. 2023. Transcriptomic analysis of mRNA expression profiles in the microglia of mouse brains infected with rabies viruses of varying virulence. *Viruses* **15**:1223. doi:10.3390/v15061223

Liu K, Kim J, Kim DW, Zhang YS, Bao H, Denaxa M, Lim S-A, Kim E, Liu C, Wickersham IR, Pachnis V, Hattar S, Song J, Brown SP, Blackshaw S. 2017. Lhx6-positive GABA-releasing neurons of the zona incerta promote sleep. *Nature* **548**:582–587. doi:10.1038/nature23663

Liu Q, Wu Y, Wang H, Jia F, Xu F. 2022. Viral tools for neural circuit tracing. *Neurosci Bull* **38**:1508–1518. doi:10.1007/s12264-022-00949-z

Liu Z, Chen O, Wall JBJ, Zheng M, Zhou Y, Wang L, Ruth Vaseghi H, Qian L, Liu J. 2017. Systematic comparison of 2A peptides for cloning multi-genes in a polycistronic vector. *Sci Rep* **7**:2193. doi:10.1038/s41598-017-02460-2

Lur G, Vinck MA, Tang L, Cardin JA, Higley MJ. 2016. Projection-specific visual feature encoding by layer 5 cortical subnetworks. *Cell Rep* **14**:2538–2545. doi:10.1016/j.celrep.2016.02.050

Ma S, Zuo Y. 2022. Synaptic modifications in learning and memory – a dendritic spine story. *Semin Cell Dev Biol* **125**:84–90. doi:10.1016/j.semcdb.2021.05.015

Madisen L, Zwingman TA, Sunkin SM, Oh SW, Zariwala HA, Gu H, Ng LL, Palmiter RD, Hawrylycz MJ, Jones AR, Lein ES, Zeng H. 2010. A robust and high-throughput Cre reporting and characterization system for the whole mouse brain. *Nat Neurosci* **13**:133–140. doi:10.1038/nn.2467

Manns JE, Hanks S, Brown JE, Double JA, Manns JE, Hanks S, Brown JE, Double JA. 1993. Methods for liquid chromatographic analysis of tamoxifen, tamoxifen metabolites and their geometric isomers in biological samples. *Anal Proc* **30**:161–163.

Markram H, Lübke J, Frotscher M, Roth A, Sakmann B. 1997. Physiology and anatomy of synaptic connections between thick tufted pyramidal neurones in the developing rat neocortex. *J Physiol* **500**:409–440. doi:10.1113/jphysiol.1997.sp022031

Marshel JH, Mori T, Nielsen KJ, Callaway EM. 2010. Targeting single neuronal networks for gene expression and cell labeling in vivo. *Neuron* **67**:562–574. doi:10.1016/j.neuron.2010.08.001

Mastop M, Bindels DS, Shaner NC, Postma M, Gadella TWJ, Goedhart J. 2017. Characterization of a spectrally diverse set of fluorescent proteins as FRET acceptors for mTurquoise2. *Sci Rep* **7**:11999. doi:10.1038/s41598-017-12212-x

Mataga N, Mizuguchi Y, Hensch TK. 2004. Experience-dependent pruning of dendritic spines in visual cortex by tissue plasminogen activator. *Neuron* **44**:1031–1041. doi:10.1016/j.neuron.2004.11.028

Maudsley H. 1876. The Physiology of Mind. London: Macmillan & Co.

Mebatsion T, Konig M, Conzelmann KK. 1996. Budding of rabies virus particles in the absence of the spike glycoprotein. *Cell* **84**:941–951. doi:10.1016/s0092-8674(00)81072-7

Merzenich MM, Nelson RJ, Stryker MP, Cynader MS, Schoppmann A, Zook JM. 1984. Somatosensory cortical map changes following digit amputation in adult monkeys. *J Comp Neurol* **224**:591–605. doi:10.1002/cne.902240408

Métin C, Godement P, Imbert M. 1988. The primary visual cortex in the mouse: Receptive field properties and functional organization. *Exp Brain Res* **69**:594–612. doi:10.1007/BF00247312

Mioche L, Singer W. 1989. Chronic recordings from single sites of kitten striate cortex during experience-dependent modifications of receptive-field properties. *J Neurophysiol* **62**:185–197. doi:10.1152/jn.1989.62.1.185

Morimoto K, Hooper DC, Spitsin S, Koprowski H, Dietzschold B. 1999. Pathogenicity of different rabies virus variants inversely correlates with apoptosis and rabies virus glycoprotein expression in infected primary neuron cultures. *J Virol* **73**:510–518. doi:10.1128/JVI.73.1.510-518.1999

Morimoto MM, Uchishiba E, Saleem AB. 2021. Organization of feedback projections to mouse primary visual cortex. *iScience* **24**:102450. doi:10.1016/j.isci.2021.102450

Mrsic-Flogel TD, Hofer SB, Ohki K, Reid RC, Bonhoeffer T, Hübener M. 2007. Homeostatic regulation of eye-specific responses in visual cortex during ocular dominance plasticity. *Neuron* **54**:961–972. doi:10.1016/j.neuron.2007.05.028

Nabavi S, Fox R, Proulx CD, Lin JY, Tsien RY, Malinow R. 2014. Engineering a memory with LTD and LTP. *Nature* **511**:348–352. doi:10.1038/nature13294

Nägerl UV, Köstinger G, Anderson JC, Martin KAC, Bonhoeffer T. 2007. Protracted synaptogenesis after activity-dependent spinogenesis in hippocampal neurons. *J Neurosci* **27**:8149–8156. doi:10.1523/JNEUROSCI.0511-07.2007

Niell CM. 2015. Cell types, circuits, and receptive fields in the mouse visual cortex. *Annu Rev Neurosci* **38**:413–431. doi:10.1146/annurev-neuro-071714-033807

Ogawa SK, Cohen JY, Hwang D, Uchida N, Watabe-Uchida M. 2014. Organization of monosynaptic inputs to the serotonin and dopamine neuromodulatory systems. *Cell Reports* **8**:1105–1118. doi:10.1016/j.celrep.2014.06.042

Oh SW, Harris JA, Ng L, Winslow B, Cain N, Mihalas S, Wang Q, Lau C, Kuan L, Henry AM, Mortrud MT, Ouellette B, Nguyen TN, Sorensen SA, Slaughterbeck CR, Wakeman W, Li Y, Feng D, Ho A, Nicholas E, Hirokawa KE, Bohn P, Joines KM, Peng H, Hawrylycz MJ, Phillips JW, Hohmann JG, Wohnoutka P, Gerfen CR, Koch C, Bernard A, Dang C, Jones AR, Zeng H. 2014. A mesoscale connectome of the mouse brain. *Nature* **508**:207–214. doi:10.1038/nature13186

Ohki K, Chung S, Ch'ng YH, Kara P, Reid RC. 2005. Functional imaging with cellular resolution reveals precise micro-architecture in visual cortex. *Nature* **433**:597–603. doi:10.1038/nature03274

Ohki K, Chung S, Kara P, Hübener M, Bonhoeffer T, Reid RC. 2006. Highly ordered arrangement of single neurons in orientation pinwheels. *Nature* **442**:925–928. doi:10.1038/nature05019

Olsen SR, Bortone D, Adesnik H, Scanziani M. 2012. Gain control by layer six in cortical circuits of vision. *Nature* **483**:47–52. doi:10.1038/nature10835

Opitz-Araya X, Barria A. 2011. Organotypic hippocampal slice cultures. *J Vis Exp* **48**:2462. doi:10.3791/2462

Osakada F, Mori T, Cetin AH, Marshel JH, Virgen B, Callaway EM. 2011. New rabies virus variants for monitoring and manipulating activity and gene expression in defined neural circuits. *Neuron* **71**:617–631. doi:10.1016/j.neuron.2011.07.005

Payne BR, Berman N, Murphy EH. 1981. Organization of direction preferences in cat visual cortex. *Brain Res* **211**:445–450. doi:10.1016/0006-8993(81)90971-9

Petreanu L, Huber D, Sobczyk A, Svoboda K. 2007. Channelrhodopsin-2–assisted circuit mapping of long-range callosal projections. *Nat Neurosci* **10**:663–668. doi:10.1038/nn1891

Pfeiffer T, Poll S, Bancelin S, Angibaud J, Inavalli VK, Keppler K, Mittag M, Fuhrmann M, Nägerl UV. 2018. Chronic 2P-STED imaging reveals high turnover of dendritic spines in the hippocampus in vivo. *eLife* **7**:e34700. doi:10.7554/eLife.34700

Piccinotti S, Kirchhausen T, Whelan SPJ. 2013. Uptake of rabies virus into epithelial cells by clathrin-mediated endocytosis depends upon actin. *J Virol* **87**. doi:10.1128/jvi.01648-13

Piccinotti S, Whelan SPJ. 2016. Rabies internalizes into primary peripheral neurons via clathrin coated pits and requires fusion at the cell body. *PLoS Pathog* **12**:e1005753. doi:10.1371/journal.ppat.1005753

Pielecka-Fortuna J, Kalogeraki E, Greifzu F, Löwel S. 2015. A small motor cortex lesion abolished ocular dominance plasticity in the adult mouse primary visual cortex and impaired experience-dependent visual improvements. *PLoS One* **10**:e0137961. doi:10.1371/journal.pone.0137961

Piscopo DM, El-Danaf RN, Huberman AD, Niell CM. 2013. Diverse visual features encoded in mouse lateral geniculate nucleus. *J Neurosci* **33**:4642–4656. doi:10.1523/JNEUROSCI.5187-12.2013

Poo M, Pignatelli M, Ryan TJ, Tonegawa S, Bonhoeffer T, Martin KC, Rudenko A, Tsai L-H, Tsien RW, Fishell G, Mullins C, Gonçalves JT, Shtrahman M, Johnston ST, Gage FH, Dan Y, Long J, Buzsáki G, Stevens C. 2016. What is memory? The present state of the engram. *BMC Biology* **14**:40. doi:10.1186/s12915-016-0261-6

Puchades MA, Csucs G, Ledergerber D, Leergaard TB, Bjaalie JG. 2019. Spatial registration of serial microscopic brain images to three-dimensional reference atlases with the QuickNII tool. *PLoS One* **14**:e0216796. doi:10.1371/journal.pone.0216796

Qin Y, Ahmadlou M, Suhai S, Neering P, de Kraker L, Heimel JA, Levelt CN. 2023. Thalamic regulation of ocular dominance plasticity in adult visual cortex. *eLife* **12**:RP88124. doi:10.7554/eLife.88124

Rabies. 2024. *World Health Organization*. https://www.who.int/news-room/fact-sheets/detail/rabies

Ragan T, Kadiri LR, Venkataraju KU, Bahlmann K, Sutin J, Taranda J, Arganda-Carreras I, Kim Y, Seung HS, Osten P. 2012. Serial two-photon tomography for automated ex vivo mouse brain imaging. *Nat Methods* **9**:255–258. doi:10.1038/nmeth.1854

Rancz EA, Franks KM, Schwarz MK, Pichler B, Schaefer AT, Margrie TW. 2011. Transfection via whole-cell recording *in vivo*: bridging single-cell physiology, genetics and connectomics. *Nat Neurosci* **14**:527–532. doi:10.1038/nn.2765

Ranson A, Cheetham CEJ, Fox K, Sengpiel F. 2012. Homeostatic plasticity mechanisms are required for juvenile, but not adult, ocular dominance plasticity. *Proc Natl Acad Sci USA* **109**:1311–1316. doi:10.1073/pnas.1112204109

Rashbrook VS, Denti L, Ruhrberg C. 2023. Tamoxifen exacerbates morbidity and mortality in male mice receiving medetomidine anaesthesia. *Anim Welf* **32**:e78. doi:10.1017/awf.2023.98

Rátkai A, Tárnok K, Aouad HE, Micska B, Schlett K, Szücs A. 2021. Homeostatic plasticity and burst activity are mediated by hyperpolarization-activated cation currents and T-type calcium channels in neuronal cultures. *Sci Rep* **11**:3236. doi:10.1038/s41598-021-82775-3

Reardon TR, Murray AJ, Turi GF, Wirblich C, Croce KR, Schnell MJ, Jessell TM, Losonczy A. 2016. Rabies virus CVS-N2cΔG strain enhances retrograde synaptic transfer and neuronal viability. *Neuron* **89**:711–724. doi:10.1016/j.neuron.2016.01.004

Reinert S, Hübener M, Bonhoeffer T, Goltstein PM. 2021. Mouse prefrontal cortex represents learned rules for categorization. *Nature* **593**:411–417. doi:10.1038/s41586-021-03452-z

Restani L, Cerri C, Pietrasanta M, Gianfranceschi L, Maffei L, Caleo M. 2009. Functional masking of deprived eye responses by callosal input during ocular dominance plasticity. *Neuron* **64**:707–718. doi:10.1016/j.neuron.2009.10.019

Robertson DW, Katzenellenbogen JA. 1982. Synthesis of the (E) and (Z) isomers of the antiestrogen tamoxifen and its metabolite, hydroxytamoxifen, in tritium-labeled form. *J Org Chem* **47**:2387–2393. doi:10.1021/jo00133a030

Rogers A, Beier KT. 2021. Can transsynaptic viral strategies be used to reveal functional aspects of neural circuitry? *J Neurosci Methods* **348**:109005. doi:10.1016/j.jneumeth.2020.109005

Rompani SB, Müllner FE, Wanner A, Zhang C, Roth CN, Yonehara K, Roska B. 2017. Different modes of visual integration in the lateral geniculate nucleus revealed by single-cell-initiated transsynaptic tracing. *Neuron* **93**:767-776.e6. doi:10.1016/j.neuron.2017.01.028

Rose T, Bonhoeffer T. 2018. Experience-dependent plasticity in the lateral geniculate nucleus. *Curr Opin Neurobiol* **53**:22–28. doi:10.1016/j.conb.2018.04.016

Rose T, Jaepel J, Hübener M, Bonhoeffer T. 2016. Cell-specific restoration of stimulus preference after monocular deprivation in the visual cortex. *Science* **352**:1319–1322. doi:10.1126/science.aad3358

Rosenberg M, Zhang T, Perona P, Meister M. 2021. Mice in a labyrinth show rapid learning, sudden insight, and efficient exploration. *eLife* **10**:e66175. doi:10.7554/eLife.66175

Rossi LF, Harris KD, Carandini M. 2019. Excitatory and inhibitory intracortical circuits for orientation and direction selectivity. *bioRxiv.* doi:10.1101/556795

Rossi M, Salomon A, Chaumontel N, Molet J, Bailly S, Tillet E, Bouvard C. 2023. Warning regarding hematological toxicity of tamoxifen activated CreERT2 in young Rosa26CreERT2 mice. *Sci Rep* **13**:5976. doi:10.1038/s41598-023-32633-1

Sato M, Stryker MP. 2008. Distinctive features of adult ocular dominance plasticity. *J Neurosci* **28**:10278–10286. doi:10.1523/JNEUROSCI.2451-08.2008

Sawtell NB, Frenkel MY, Philpot BD, Nakazawa K, Tonegawa S, Bear MF. 2003. NMDA receptor-dependent ocular dominance plasticity in adult visual cortex. *Neuron* **38**:977–985. doi:10.1016/s0896-6273(03)00323-4

Schalch T. 2017. Higher order chromatin structures are taking shape. *Z Med Phys* **27**:75–77. doi:10.1016/j.zemedi.2017.03.002

Schuett S, Bonhoeffer T, Hübener M. 2002. Mapping retinotopic structure in mouse visual cortex with optical imaging. *J Neurosci* **22**:6549–6559. doi:10.1523/JNEUROSCI.22-15-06549.2002

Schwenk F, Kuhn R, Angrand PO, Rajewsky K, Stewart AF. 1998. Temporally and spatially regulated somatic mutagenesis in mice. *Nucleic Acids Res* **26**:1427–1432.

Schwob JE, Youngentob SL, Ring G, Iwema CL, Mezza RC. 1999. Reinnervation of the rat olfactory bulb after methyl bromide-induced lesion: Timing and extent of reinnervation. *J Comp Neurol* **412**:439–457. doi:10.1002/(SICI)1096-9861(19990927)412:3<439::AID-CNE5>3.0.CO;2-H

Seidler B, Schmidt A, Mayr U, Nakhai H, Schmid RM, Schneider G, Saur D. 2008. A Cre-loxP-based mouse model for conditional somatic gene expression and knockdown in vivo by using avian retroviral vectors. *Proc Natl Acad Sci USA* **105**:10137–10142. doi:10.1073/pnas.0800487105

Shao Q, Chen L, Li Xiaowan, Li M, Cui H, Li Xiaoyue, Zhao X, Shi Y, Sun Q, Yan K, Wang G. 2024. A non-canonical visual cortical-entorhinal pathway contributes to spatial navigation. *Nat Commun* **15**:4122. doi:10.1038/s41467-024-48483-y

Siegle JH, Jia X, Durand S, Gale S, Bennett C, Graddis N, Heller G, Ramirez TK, Choi H, Luviano JA, Groblewski PA, Ahmed R, Arkhipov A, Bernard A, Billeh YN, Brown D, Buice MA, Cain N, Caldejon S, Casal L, Cho A, Chvilicek M, Cox TC, Dai K, Denman DJ, de Vries SEJ, Dietzman R, Esposito L, Farrell C, Feng D, Galbraith J, Garrett M, Gelfand EC, Hancock N, Harris JA, Howard R, Hu B, Hytnen R, Iyer R, Jessett E, Johnson K, Kato I, Kiggins J, Lambert S, Lecoq J, Ledochowitsch P, Lee JH, Leon A, Li Y, Liang E, Long F, Mace K, Melchior J, Millman D, Mollenkopf T, Nayan C, Ng L, Ngo K, Nguyen T, Nicovich PR, North K, Ocker GK, Ollerenshaw D, Oliver M, Pachitariu M, Perkins J, Reding M, Reid D, Robertson M, Ronellenfitch K, Seid S, Slaughterbeck C, Stoecklin M, Sullivan D, Sutton B, Swapp J, Thompson C, Turner K, Wakeman W, Whitesell JD, Williams D, Williford A, Young R, Zeng H, Naylor S, Phillips JW, Reid RC, Mihalas S, Olsen SR, Koch C. 2021. Survey of spiking in the mouse visual system reveals functional hierarchy. *Nature* **592**:86–92. doi:10.1038/s41586-020-03171-x

Soriano P. 1999. Generalized lacZ expression with the ROSA26 Cre reporter strain. *Nat Genet* **21**:70–71. doi:10.1038/5007

Spanagel R. 2017. Animal models of addiction. *Dialogues Clin Neurosci* **19**:247–258.

Stoppini L, Buchs PA, Muller D. 1991. A simple method for organotypic cultures of nervous tissue. *J Neurosci Methods* **37**:173-182. doi:10.1016/0165-0270(91)90128-m

Stoppini L, Parisi L, Oropesa C, Muller D. 1997. Sprouting and functional recovery in co-cultures between old and young hippocampal organotypic slices. *J Neurosci* 80:1127–1136. doi:10.1016/S0306-4522(97)00132-2

Sun Q, Li X, Ren M, Zhao M, Zhong Q, Ren Y, Luo P, Ni H, Zhang X, Zhang C, Yuan J, Li A, Luo M, Gong H, Luo Q. 2019. A whole-brain map of long-range inputs to GABAergic interneurons in the mouse medial prefrontal cortex. *Nat Neurosci* 22:1357–1370. doi:10.1038/s41593-019-0429-9

Svoboda K. 2019. Using rabies virus for tracing neural connections: caveats and limitations exposed by studies of barrel cortex circuits. *Occasional commentary on the science of neural circuits*. https://spikesphotons.wordpress.com/2019/05/13/using-rabies-virus-for-tracing-neural-connections-caveats-and-limitations-exposed-by-studies-of-barrel-cortex-circuits/

Sztainberg Y, Chen A. 2010. An environmental enrichment model for mice. *Nat Protoc* 5:1535–1539. doi:10.1038/nprot.2010.114

Tagawa Y, Kanold PO, Majdan M, Shatz CJ. 2005. Multiple periods of functional ocular dominance plasticity in mouse visual cortex. *Nat Neurosci* 8:380–388. doi:10.1038/nn1410

Tanaka S, Ribot J, Imamura K, Tani T. 2006. Orientation-restricted continuous visual exposure induces marked reorganization of orientation maps in early life. *Neuroimage* 30:462–477. doi:10.1016/j.neuroimage.2005.09.056

Tang Y, Rampin O, Giuliano F, Ugolini G. 1999. Spinal and brain circuits to motoneurons of the bulbospongiosus muscle: Retrograde transneuronal tracing with rabies virus. *J Comp Neurol* 414:167–192. doi:10.1002/(SICI)1096-9861(19991115)414:2<167::AID-CNE3>3.0.CO;2-P

Tootell RB, Silverman MS, De Valois RL. 1981. Spatial Frequency Columns in Primary Visual Cortex. *Science* 214:813–815. doi:10.1126/science.7292014

Tordo N, Kouknetzoff A. 1993. The rabies virus genome: an overview. *Onderstepoort J Vet Res* 60:263–269.

Tordo N, Poch O, Ermine A, Keith G, Rougeon F. 1988. Completion of the rabies virus genome sequence determination: Highly conserved domains among the L (polymerase) proteins of unsegmented negative-strand RNA viruses. *J Virol* 165:565–576. doi:10.1016/0042-6822(88)90600-9

Trachtenberg JT, Chen BE, Knott GW, Feng G, Sanes JR, Welker E, Svoboda K. 2002. Long-term in vivo imaging of experience-dependent synaptic plasticity in adult cortex. *Nature* 420:788–794. doi:10.1038/nature01273

Trachtenberg JT, Stryker MP. 2001. Rapid anatomical plasticity of horizontal connections in the developing visual cortex. *J Neurosci* 21:3476–3482. doi:10.1523/JNEUROSCI.21-10-03476.2001

Trachtenberg JT, Trepel C, Stryker MP. 2000. Rapid extragranular plasticity in the absence of thalamocortical plasticity in the developing primary visual cortex. *Science* 287:2029–2032. doi:10.1126/science.287.5460.2029

Tritsch NX, Sabatini BL. 2012. Dopaminergic modulation of synaptic transmission in cortex and striatum. *Neuron* 76:33–50. doi:10.1016/j.neuron.2012.09.023

Troyer TW, Krukowski AE, Priebe NJ, Miller KD. 1998. Contrast-invariant orientation tuning in cat visual cortex: thalamocortical input tuning and correlation-based

intracortical connectivity. *J Neurosci* **18**:5908–5927. doi:10.1523/JNEUROSCI.18-15-05908.1998

Tuffereau C, Schmidt K, Langevin C, Lafay F, Dechant G, Koltzenburg M. 2007. The rabies virus glycoprotein receptor p75NTR is not essential for rabies virus infection. *J Virol* **81**:13622–13630. doi:10.1128/JVI.02368-06

Uesaka N, Hirai S, Maruyama T, Ruthazer ES, Yamamoto N. 2005. Activity dependence of cortical axon branch formation: a morphological and electrophysiological study using organotypic slice cultures. *J Neurosci* **25**:1–9. doi:10.1523/JNEUROSCI.3855-04.2005

Ugolini G. 2011. Rabies virus as a transneuronal tracer of neuronal connections. *Adv Virus Res* **79**:165-202. doi:10.1016/B978-0-12-387040-7.00010-X

Ugolini G. 2010. Advances in viral transneuronal tracing. *J Neurosci Methods* **194**:2–20. doi:10.1016/j.jneumeth.2009.12.001

Ugolini G. 1995. Specificity of rabies virus as a transneuronal tracer of motor networks: Transfer from hypoglossal motoneurons to connected second-order and higher order central nervous system cell groups. *J Comp Neurol* **356**:457–480. doi:10.1002/cne.903560312

Valny M, Honsa P, Kirdajova D, Kamenik Z, Anderova M. 2016. Tamoxifen in the mouse brain: Implications for fate-mapping studies using the tamoxifen-inducible cre-loxP system. *Front Cell Neurosci* **10**: 243. doi:10.3389/fncel.2016.00243

van Versendaal D, Rajendran R, Saiepour MH, Klooster J, Smit-Rigter L, Sommeijer J-P, De Zeeuw CI, Hofer SB, Heimel JA, Levelt CN. 2012. Elimination of inhibitory synapses is a major component of adult ocular dominance plasticity. *Neuron* **74**:374–383. doi:10.1016/j.neuron.2012.03.015

Vangeneugden J, van Beest EH, Cohen MX, Lorteije JAM, Mukherjee S, Kirchberger L, Montijn JS, Thamizharasu P, Camillo D, Levelt CN, Roelfsema PR, Self MW, Heimel JA. 2019. Activity in lateral visual areas contributes to surround suppression in awake mouse V1. *Curr Biol* **29**:4268-4275.e7. doi:10.1016/j.cub.2019.10.037

Vooijs M, Jonkers J, Berns A. 2001. A highly efficient ligand-regulated Cre recombinase mouse line shows that LoxP recombination is position dependent. *EMBO reports* **2**:292–297. doi:10.1093/embo-reports/kve064

Wall NR, De La Parra M, Callaway EM, Kreitzer AC. 2013. Differential innervation of direct- and indirect-pathway striatal projection neurons. *Neuron* **79**:347–360. doi:10.1016/j.neuron.2013.05.014

Wang H, Dey O, Lagos WN, Behnam N, Callaway EM, Stafford BK. 2024. Parallel pathways carrying direction-and orientation-selective retinal signals to layer 4 of the mouse visual cortex. *Cell Reports* **43**:113830. doi:10.1016/j.celrep.2024.113830

Wang J, Wang Z, Liu R, Shuai L, Wang Xinxin, Luo J, Wang C, Chen W, Wang Xijun, Ge J, He X, Wen Z, Bu Z. 2018. Metabotropic glutamate receptor subtype 2 is a cellular receptor for rabies virus. *PLoS Pathog* **14**:e1007189. doi:10.1371/journal.ppat.1007189

Wang Q, Burkhalter A. 2007. Area map of mouse visual cortex. *J Comp Neurol* **502**:339–357. doi:10.1002/cne.21286

Wang Q, Ding S-L, Li Y, Royall J, Feng D, Lesnar P, Graddis N, Naeemi M, Facer B, Ho A, Dolbeare T, Blanchard B, Dee N, Wakeman W, Hirokawa KE, Szafer A, Sunkin SM, Oh SW, Bernard A, Phillips JW, Hawrylycz M, Koch C, Zeng H, Harris JA, Ng L. 2020.

The Allen Mouse Brain Common Coordinate Framework: a 3D reference atlas. *Cell* 181:936-953.e20. doi:10.1016/j.cell.2020.04.007

Watabe-Uchida M, Zhu L, Ogawa SK, Vamanrao A, Uchida N. 2012. Whole-brain mapping of direct inputs to midbrain dopamine neurons. *Neuron* 74:858–873. doi:10.1016/j.neuron.2012.03.017

Weliky M, Bosking WH, Fitzpatrick D. 1996. A systematic map of direction preference in primary visual cortex. *Nature* 379:725–728. doi:10.1038/379725a0

Wertz A, Trenholm S, Yonehara K, Hillier D, Raics Z, Leinweber M, Szalay G, Ghanem A, Keller G, Rózsa B, Conzelmann K-K, Roska B. 2015. Single-cell–initiated monosynaptic tracing reveals layer-specific cortical network modules. *Science* 349:70–74. doi:10.1126/science.aab1687

Whitfield J, Littlewood T, Soucek L. 2015. Tamoxifen administration to mice. *Cold Spring Harb Protoc* 2015:269. doi:10.1101/pdb.prot077966

Whitlock JR, Heynen AJ, Shuler MG, Bear MF. 2006. Learning induces long-term potentiation in the hippocampus. *Science* 313:1093–1097. doi:10.1126/science.1128134

Wickersham Ian R, Finke S, Conzelmann K-K, Callaway EM. 2007a. Retrograde neuronal tracing with a deletion-mutant rabies virus. *Nat Methods* 4:47–49. doi:10.1038/NMETH999

Wickersham Ian R., Lyon DC, Barnard RJO, Mori T, Finke S, Conzelmann K-K, Young JAT, Callaway EM. 2007b. Monosynaptic restriction of transsynaptic tracing from single, genetically targeted neurons. *Neuron* 53:639–647. doi:10.1016/j.neuron.2007.01.033

Wiesel TN, Hubel DH. 1963. Single-cell responses in striate cortex of kittens deprived of vision in one eye. *J Neurophysiol* 26:1003-17. doi:10.1152/jn.1963.26.6.1003

Wiesel TN, Hubel DH, Lam DMK. 1974. Autoradiographic demonstration of ocular-dominance columns in the monkey striate cortex by means of transneuronal transport. *Brain Res* 79:273–279. doi:10.1016/0006-8993(74)90416-8

Wilkemeyer MF, Angelides KJ. 1996. Addition of tetrodotoxin alters the morphology of thalamocortical axons in organotypic cocultures. *J Neurosci Res* 43:707–718. doi:10.1002/(SICI)1097-4547(19960315)43:6<707::AID-JNR7>3.0.CO;2-I

Xu T, Yu X, Perlik AJ, Tobin WF, Zweig JA, Tennant K, Jones T, Zuo Y. 2009. Rapid formation and selective stabilization of synapses for enduring motor memories. *Nature* 462:915–919. doi:10.1038/nature08389

Yamada A, Uesaka N, Hayano Y, Tabata T, Kano M, Yamamoto N. 2010. Role of pre- and postsynaptic activity in thalamocortical axon branching. *Proc Natl Acad Sci USA* 107:7562–7567. doi:10.1073/pnas.0900613107

Yang G, Pan F, Gan W-B. 2009. Stably maintained dendritic spines are associated with lifelong memories. *Nature* 462:920–924. doi:10.1038/nature08577

Yao S, Wang Q, Hirokawa KE, Ouellette B, Ahmed R, Bomben J, Brouner K, Casal L, Caldejon S, Cho A, Dotson NI, Daigle TL, Egdorf T, Enstrom R, Gary A, Gelfand E, Gorham M, Griffin F, Gu H, Hancock N, Howard R, Kuan L, Lambert S, Lee EK, Luviano J, Mace K, Maxwell M, Mortrud MT, Naeemi M, Nayan C, Ngo N-K, Nguyen T, North K, Ransford S, Ruiz A, Seid S, Swapp J, Taormina MJ, Wakeman W, Zhou T, Nicovich PR, Williford A, Potekhina L, McGraw M, Ng L, Groblewski PA, Tasic B, Mihalas S, Harris JA, Cetin A, Zeng H. 2023. A whole-brain monosynaptic

input connectome to neuron classes in mouse visual cortex. *Nat Neurosci* **26**:350–364. doi:10.1038/s41593-022-01219-x

Yates SC, Groeneboom NE, Coello C, Lichtenthaler SF, Kuhn P-H, Demuth H-U, Hartlage-Rübsamen M, Roßner S, Leergaard T, Kreshuk A, Puchades MA, Bjaalie JG. 2019. QUINT: Workflow for quantification and spatial analysis of features in histological images from rodent brain. *Front Neuroinform* **13**:75. doi:10.3389/fninf.2019.00075

Ye Q, Gast G, Su X, Saito T, Saido TC, Holmes TC, Xu X. 2022. Hippocampal neural circuit connectivity alterations in an Alzheimer's disease mouse model revealed by monosynaptic rabies virus tracing. *Neurobiol Dis* **172**:105820. doi:10.1016/j.nbd.2022.105820

Zhou Y, Lai B, Gan W-B. 2017. Monocular deprivation induces dendritic spine elimination in the developing mouse visual cortex. *Sci Rep* **7**:4977. doi:10.1038/s41598-017-05337-6

Zhou Y, Lai CSW, Bai Y, Li W, Zhao R, Yang G, Frank MG, Gan W-B. 2020. REM sleep promotes experience-dependent dendritic spine elimination in the mouse cortex. *Nat Commun* **11**:4819. doi:10.1038/s41467-020-18592-5

Zuo Y, Lin A, Chang P, Gan W-B. 2005. Development of long-term dendritic spine stability in diverse regions of cerebral cortex. *Neuron* **46**:181–189. doi:10.1016/j.neuron.2005.04.001

Supplementary Figures

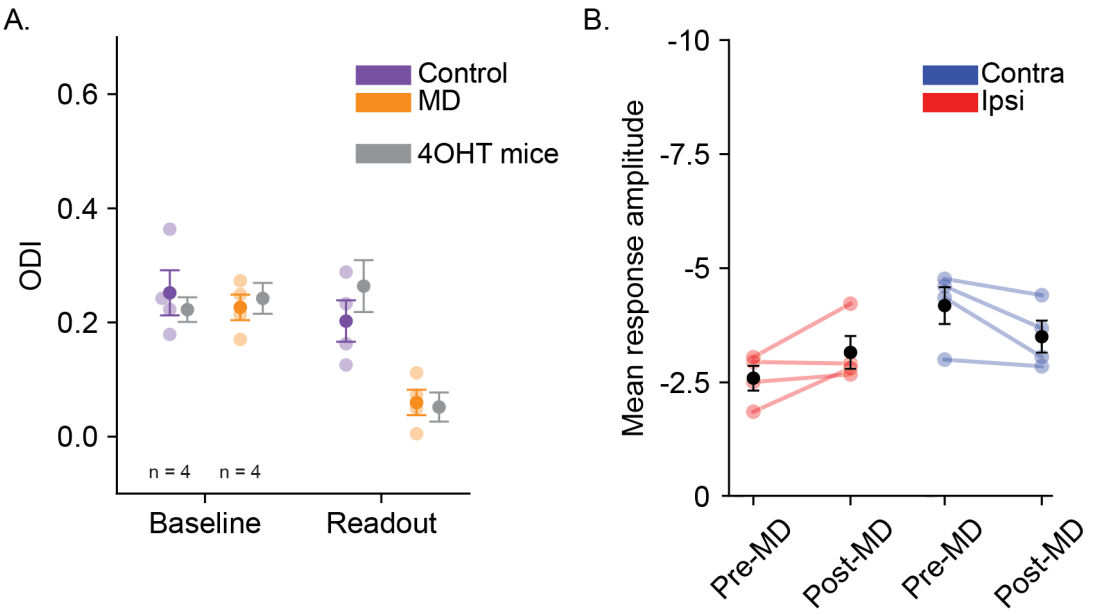

Supplementary Figure 1. | 4OHT does not influence OD plasticity. A: Ocular dominance indices for eight mice (four control, four MD) who were not treated with 4OHT. Baseline values are averaged over three imaging sessions. Gray bars indicate mean ± SEM reported in Fig. 3.8C for TTT mice, for comparison. **B:** Response amplitudes after stimulation of the unaffected, ipsilateral (red) or deprived, contralateral (blue) eye, for mice in the no-4OHT MD group, pre-eye suture (average over three baseline sessions) and post-eye suture. Lines connect points corresponding to the same mouse.

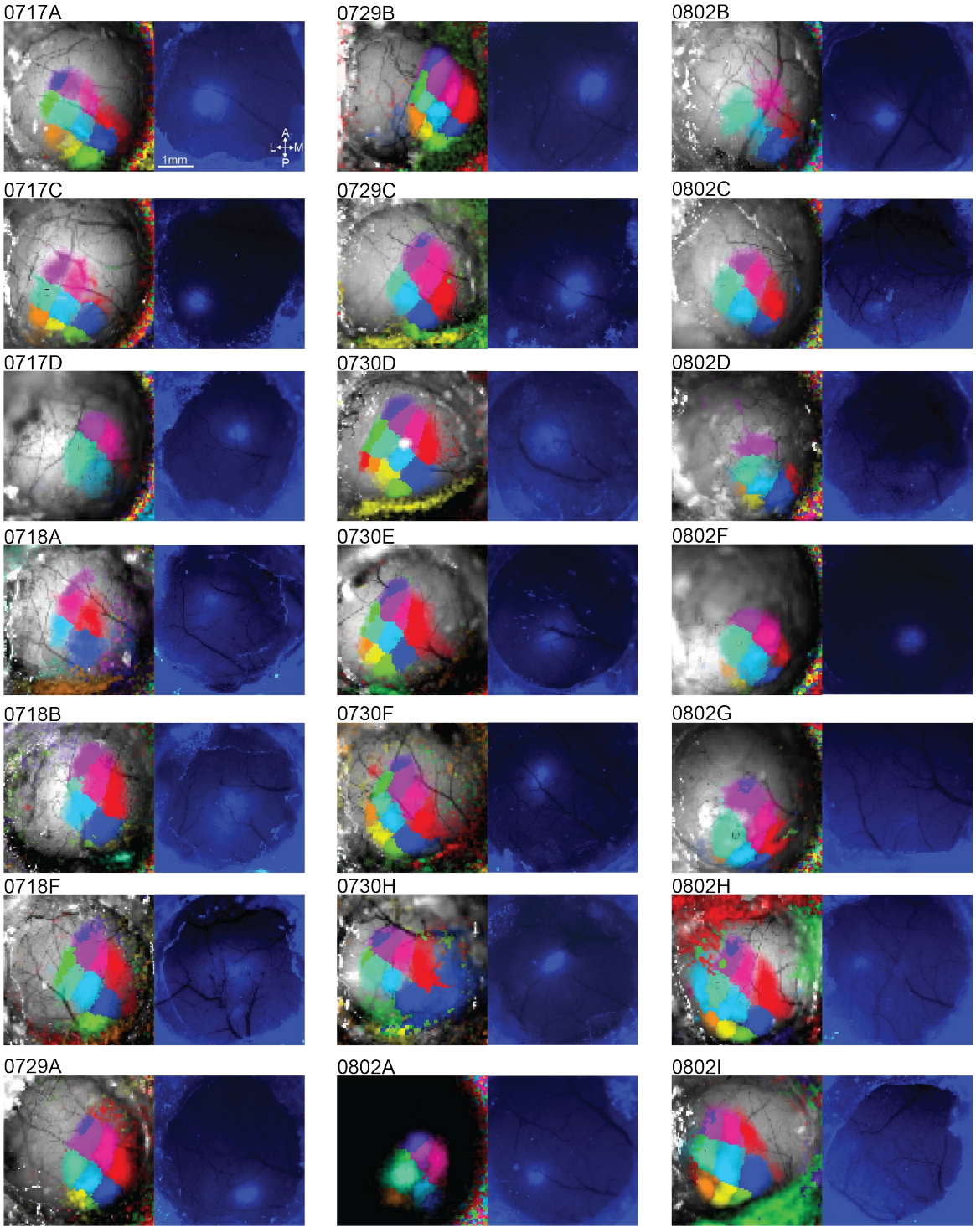
0717A
1mm
A
L
M
P
0729B
0802B
0717C
0729C
0802C
0717D
0730D
0802D
0718A
0730E
0802F
0718B
0730F
0802G
0718F
0730H
0802H
0729A
0802A
0802I

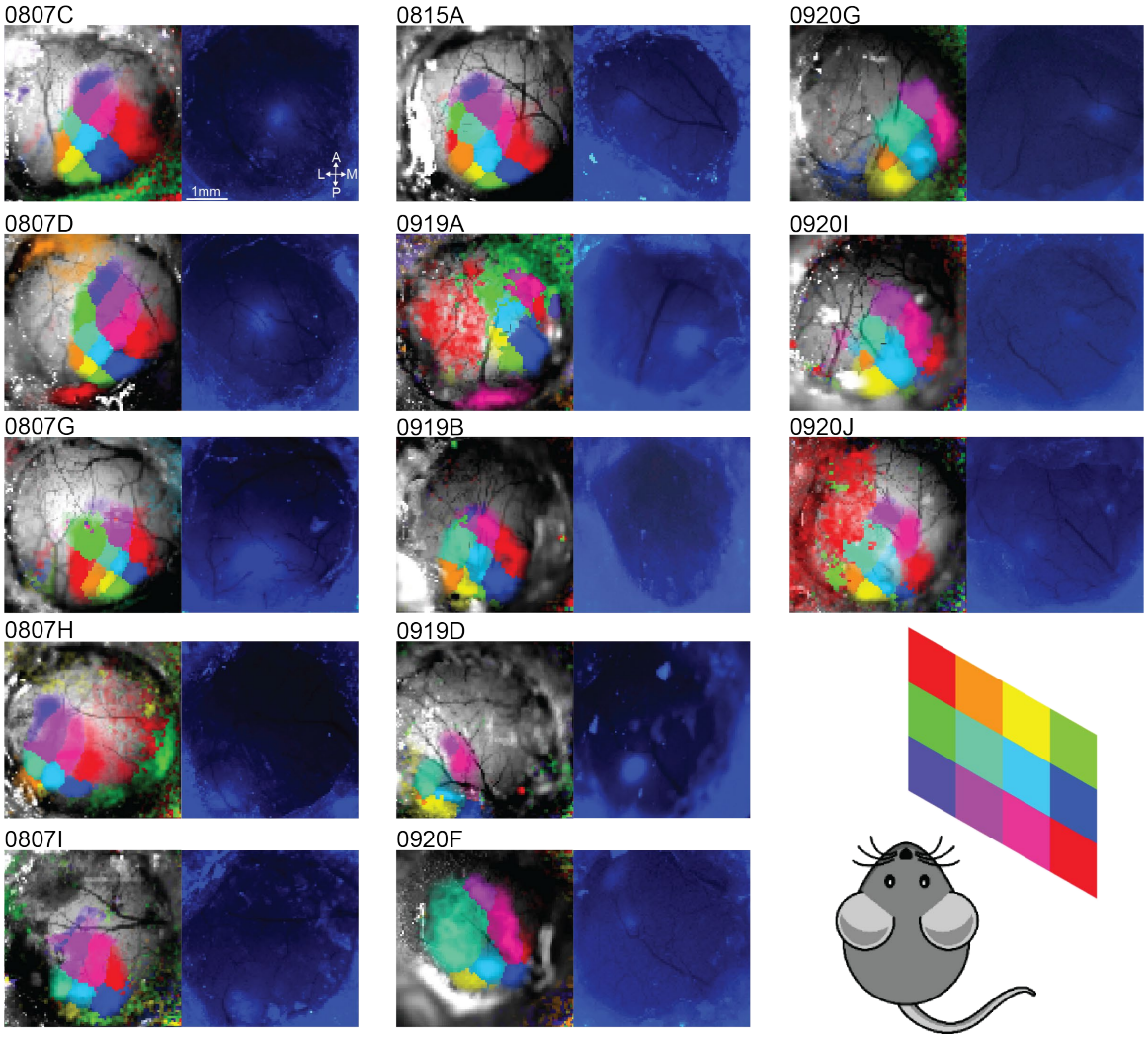

Supplementary Figure 2. | Comparison of retinotopy and expression of helper virus mTurquoise2 in TTT mice. For each mouse: *Left* Brightfield image through the cranial window, overlaid with color coded (see schematic at bottom right) retinotopic map. *Right*: Epifluorescence image through cranial window after two to three weeks of helper virus expression. A, L, M, P: Anterior, lateral, medial, posterior.

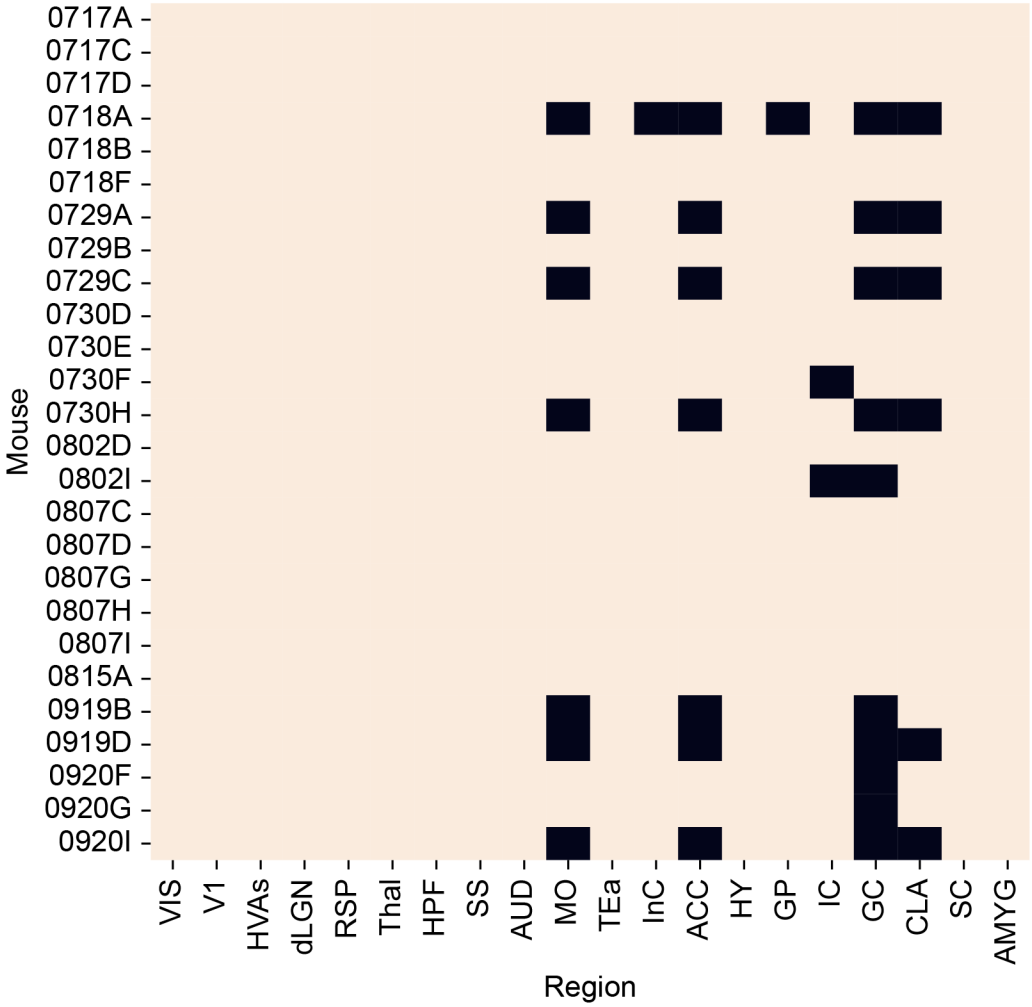

Supplementary Figure 3. | Regions imaged in each mouse. Regions are not all mutually exclusive. Black squares indicate regions not imaged in a given mouse. VIS, visual cortex. V1, primary visual cortex. HVAs, higher visual areas. dLGN, dorsal lateral geniculate nucleus. RSP, retrosplenial cortex. Thal, thalamus. HPF, hippocampal formation. SS, somatosensory cortex. AUD, auditory cortex. MO, motor cortex. TEa, temporal association areas. InC, insular cortex. ACC, anterior cingulate cortex. HY, hypothalamus. GP, globus palidus. IC, inferior colliculus. GC, gustatory cortex. CLA, claustrum. SC, superior colliculus. AMYG, amygdala.

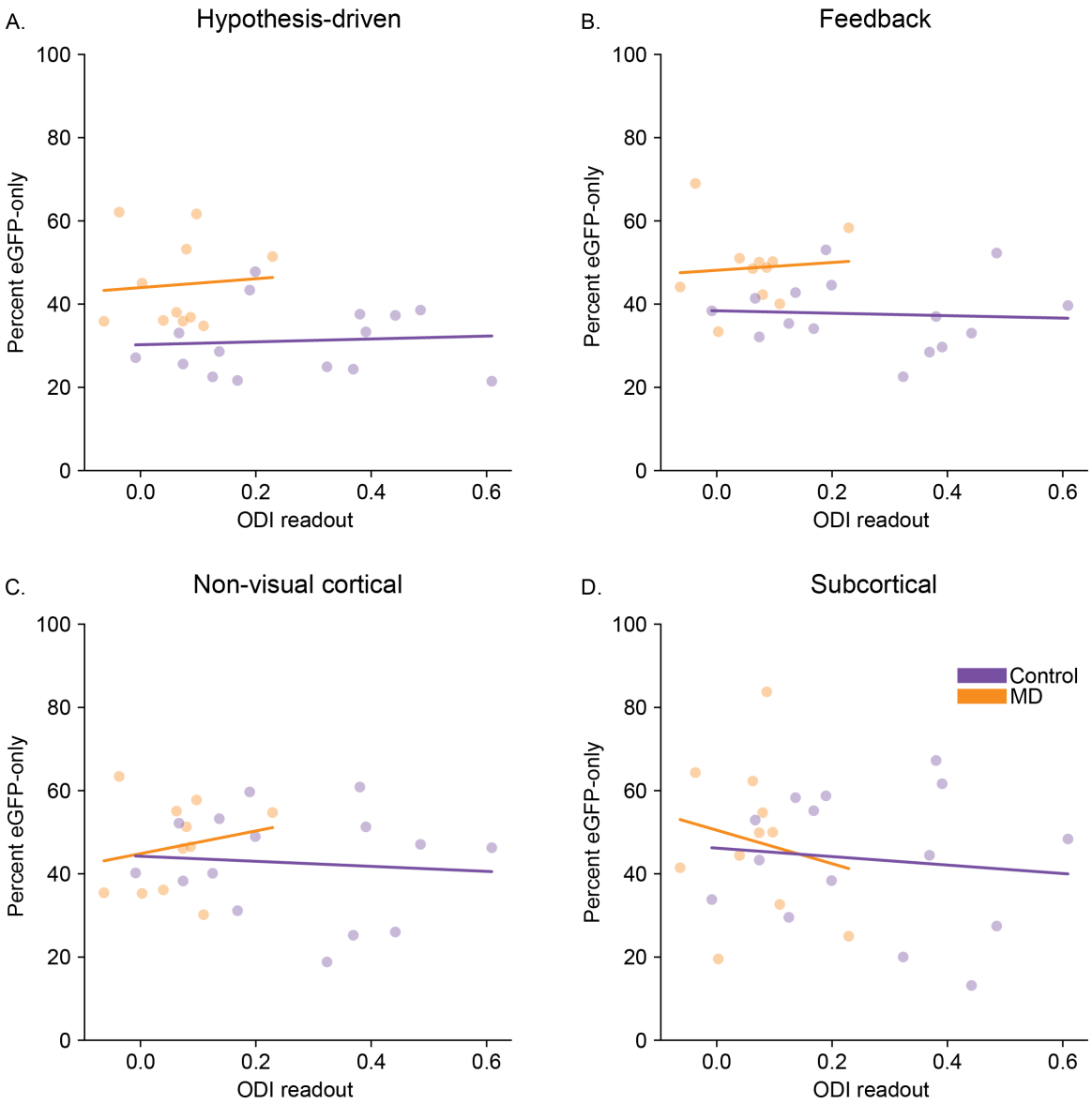

Supplementary Figure 4. | Relationship between ODI readout and the output of TTT. A: V1 (inj), V1 (non-inj), and dLGN do not show a relationship between ODI shift and percentage of eGFP-only cells. **B:** As in A, for HVAs, LP, and RSP. **C:** As in A, for seven non-visual cortical regions. **D:** As in A, for five subcortical regions.

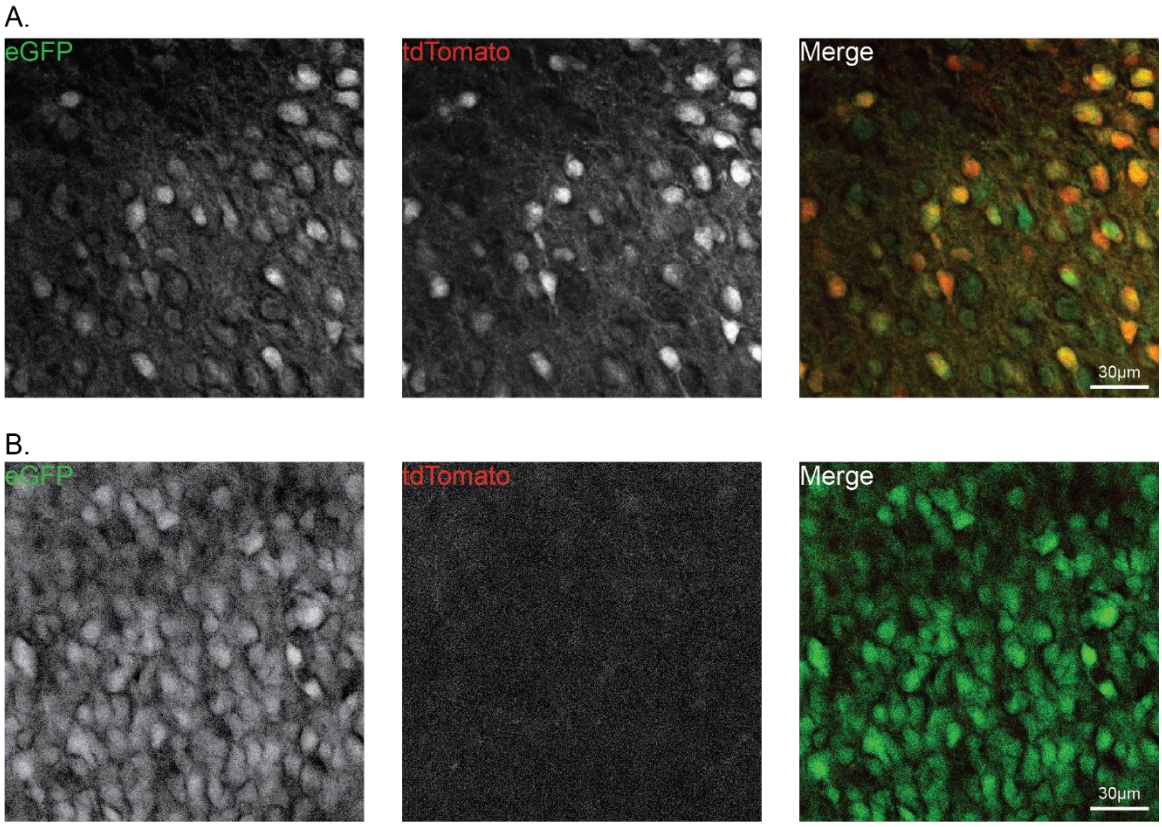

Supplementary Figure 5. | TTT components tested in organotypic cultures. A: Confocal image of organotypic culture from the experiment described in Figure 3.1 A-D. *Left:* eGFP expression associated with injection of helper virus (not shown) and rabies virus. *Center:* tdTomato expression associated with 4OHT bath application. *Right:* merged image. **B:** Confocal image of organotypic culture from the experiment described in Figure 3.1 E. *Left:* eGFP expression associated with injection of helper virus (not shown) and rabies virus. *Center:* tdTomato expression is absent, as 4OHT was not applied in this control experiment. *Right:* merged image.

List of Figures

List of Tables

List of Abbreviations

4OHT	4-hydroxytamoxifen
AAV	Adeno-associated virus
AL	Anterolateral higher visual area
AM	Anteromedial higher visual area
AMYG	Amygdala
ANCOVA	Analysis of covariance
ANOVA	Analysis of variance
AUD	Auditory cortex
bV1	Primary visual cortex, binocular region
ChR2	Channelrhodopsin-2
CLA	claustrum
CNN	Convolutional neural network
CRACM	Channelrhodopsin-2-assisted circuit mapping
CVS	Challenge virus standard
DAPI	4',6-diamidino-2-phenylindole
dLGN	Dorsal lateral geniculate nucleus of the thalamus
DLS	dorsolateral striatum
EDP	Experience-dependent plasticity
eGFP	enhanced green fluorescent protein
EnvA	Envelope A
ETC	Electrophoretic tissue clearing
FlpO	Mouse codon-optimized flippase
FMM	Fentanyl, midazolam, medetomidin
FRT	Flippase recombination target
GaAsP	Gallium Arsenide Phosphide
GC	Gustatory cortex
GECI	Genetically encoded calcium indicator
GP	Globus pallidus external segment
HPF	Hippocampal formation
HVA	Higher visual area
HY	Hypothalamus
i.p.	Intraperitoneal
IC	Inferior colliculus
InC	Insular cortex
IOS	Intrinsic optical signal
L1	Layer 1
L2/3	Layer 2/3
L4	Layer 4
L5	Layer 5

L6	Layer 6
LD	Lateral dorsal nucleus of the thalamus
LED	Light-emitting diode
LM	Lateromedial higher visual area
LP	Lateral posterior nucleus of the thalamus
LTD	Long-term depression
LTP	Long-term potentiation
MD	Monocular deprivation
mGluR2	Metabotropic glutamate receptor 2
MO	Motor cortex
mPFC	Medial prefrontal cortex
nAChR	Nicotinic acetylcholine receptor
NCAM	Neural cell adhesion molecule
OD	Ocular dominance
ODI	Ocular dominance index
p75NTR	Low-affinity nerve growth factor receptor
pAAV	Plasmid adeno-associated virus
PM	Posteromedial higher visual area
POR	Postrhinal higher visual area
RGC	Retinal ganglion cell
RL	Rostrolateral higher visual area
RPM	Rotations per minute
RSP	Retrosplenial cortex
s.c.	Subcutaneous
SAD	Street Alabama Dufferin
SEM	Standard error of the mean
SC	Superior colliculus
SCE	Single-cell electroporation
sCMOS	Scientific complementary metal-oxide-semiconductor
SNc	Substantia nigra pars compacta
SS	Somatosensory cortex
SSR	Site-specific recombinase
TEa	Temporal associataion areas
Thal	Thalamus
TTT	Two-timeframe tracing
TTX	Tetrodotoxin
TVA	Tumor virus A
V1	Primary visual cortex
VTA	Ventral tegmental area

Acknowledgements

I once read some excellent advice about working in science and academia — “Everyone here is smart. Distinguish yourself by being kind.” By this logic, I’ve been lucky enough to work with the most distinguished scientists around. And Pieter, you’re at the top of this list. Thank you for trusting me with the “rabies project” way before I trusted me with this project. Thank you for exemplifying what it is to be a good scientist and mentor. Thanks for knowing exactly when to let me figure it out on my own, and when to step in and save the day. You have a knack for putting things and mistakes into perspective, in such a way that has turned the most challenging parts of the past few years into really rewarding growing experiences. I’m so thankful to have you as a supervisor and a friend.

Mark, I’m so grateful for your support of both my PhD and of the rabies project. Your insight, scientific input, and attention to detail are inspiring, and have made every poster, abstract, and now this thesis immeasurably better. From planning experiments, to looking at the initial preliminary results, your optimism and excitement about the project has been so motivating.

Tobias, thank you so much for accepting me into your lab, seeing the potential in the rabies project, and for financial support. Thank you for trusting me to make decisions that shaped this project, and for providing invaluable scientific input and guidance.

The work presented here was made possible, and made so much easier than it could have been, by invaluable technical support from Volker, Claudia, Dominik, Frank, Max, and Miri. Thank you all for your assistance with mice, cultures, histology, setups, and all of the work that makes the lab function.

I am grateful to the team at the Graduate School of Systemic Neurosciences for the support over the past six years, including financial support during an incredibly rewarding and challenging “Fast-Track” preparatory year. Thank you for bringing together such clever young scientists and for providing opportunities for us all to learn from each other

To my students who I had the privilege to supervise, Anna, Connor, and Laura - thank you for joining the rabies project for a time! I’m grateful for your scientific contributions to the in vitro experiments and the data processing pipeline that helped shape this project.

To my past and present officemates, Matt, Martin, Volker, and Adrianna - I love our little Krabbelgruppe. Thank you for letting me interrupt your work eight times every hour, thanks for sharing tea and snacks and advice. Thanks for letting me jump rope in the office.

To all of the BonBros - You’ve created an environment where people can’t help but to grow towards the very best version of themselves, both professionally and personally, and that’s amazing and rare. I’m so grateful to be a part of it. Thank you for the always-entertaining lunch conversations, relaxing coffee chats, super intricate Happy Hours, cycling and other “shport” adventures, and of course for the scientific support and input.

To my GSN pals, it's your friendship and endless support that make Munich feel like home. I'm so thankful that we got to grow together for these past few years, and I hope you know I'll be rooting for you always.

To Maxie — I cannot overstate how vital your unwavering support for the rabies project and for me has been. Thank you for saving the analysis pipeline and for all of the work you've done to advance the data through it. Thanks for always being there, with ice cream and a reel and a fresh perspective on our experiments and analyses. I'm so glad you decided that TTT is worth pursuing in your PhD; you are exactly what the lab needed. I'm stoked to see what kind of whimsical and brilliant things you'll come up with in the next years.

To my family, especially Mom, Dad, John, and Jacqueline - it's not easy to learn how to love someone from really far away, and I'm so thankful that it feels like we're quite good at it by now. Thank you for supporting me, in great big giant ways and in subtle, quiet ways, too. I'll love you forever (I'll like you for always).